6. FLOW VISUALISATION OF THE VORTEX WAKE

As established in the previous chapter, the cylinder Reynolds number and the yaw angle are the two major parameters influencing vortex shedding from yawed cylinders. In the flow over a yawed cylinder the incident flow has velocity components along and normal to the axis of the cylinder; these lead to corresponding components of the vorticity vector in the cylinder wake. The total vorticity vector, and therefore the axes of the shed vortices, as will be seen later, are inclined to the cylinder axis (as discussed by Ramberg 1983) - at an angle referred to as the vortex-shedding angle.

The aim of the flow visualisation presented in this chapter is to examine the dependence of the vortex-shedding angle on the geometric yaw angle and the cylinder Reynolds number. The effect of the axial velocity component on the vortex-shedding frequency measurements, presented in chapter five, is examined with reference to the associated vortex-shedding angles.

6.1 Visualisation of the Vortex Wake in Air

The flow was visualised by smoke streaks generated by a fine electrically-heated oil-coated wire, and recorded by video camera. Images of the vortex structure in the cylinder wake were obtained from single video frames.

Typical images obtained by this technique (some of which were also given by Bull and Dekkers (1992a, Appendix 2) and Dekkers and Bull (1992, Appendix 6) are shown in Figure [6.1] for large yaw angles. The oil smoke follows the streamlines of the flow, and becomes concentrated in the vortex cores, allowing the vortex axes to be identified.

The limitations of this technique are set by the short duration of the smoke streaks, the uncertainty in the time lag between turning on the electric current and the smoke appearing, and the small amount of light reflected by the tenuous streaks of smoke. The poor reflectivity of the smoke requires very bright light to achieve a visible image. The uncertainties in the timing of the smoke due to variations in the thickness of the oil coating and the prior temperature of the resistance wire make flash photography impracticable, necessitating the use of continuous lighting at lower power.

The rapid consumption of the thin oil layer and consequent short duration of the smoke streaks result in only a few video frames of conventional video footage (25 frames per second) when the smoke is uniformly present in sufficient density to produce a useful image. The use of a high speed video camera(<1000 frames per

second) did little to solve these problems as the camera performance was severely limited by the available light, and images of a quality comparable to those obtained by a conventional video camera were obtained only at similar framing rates.

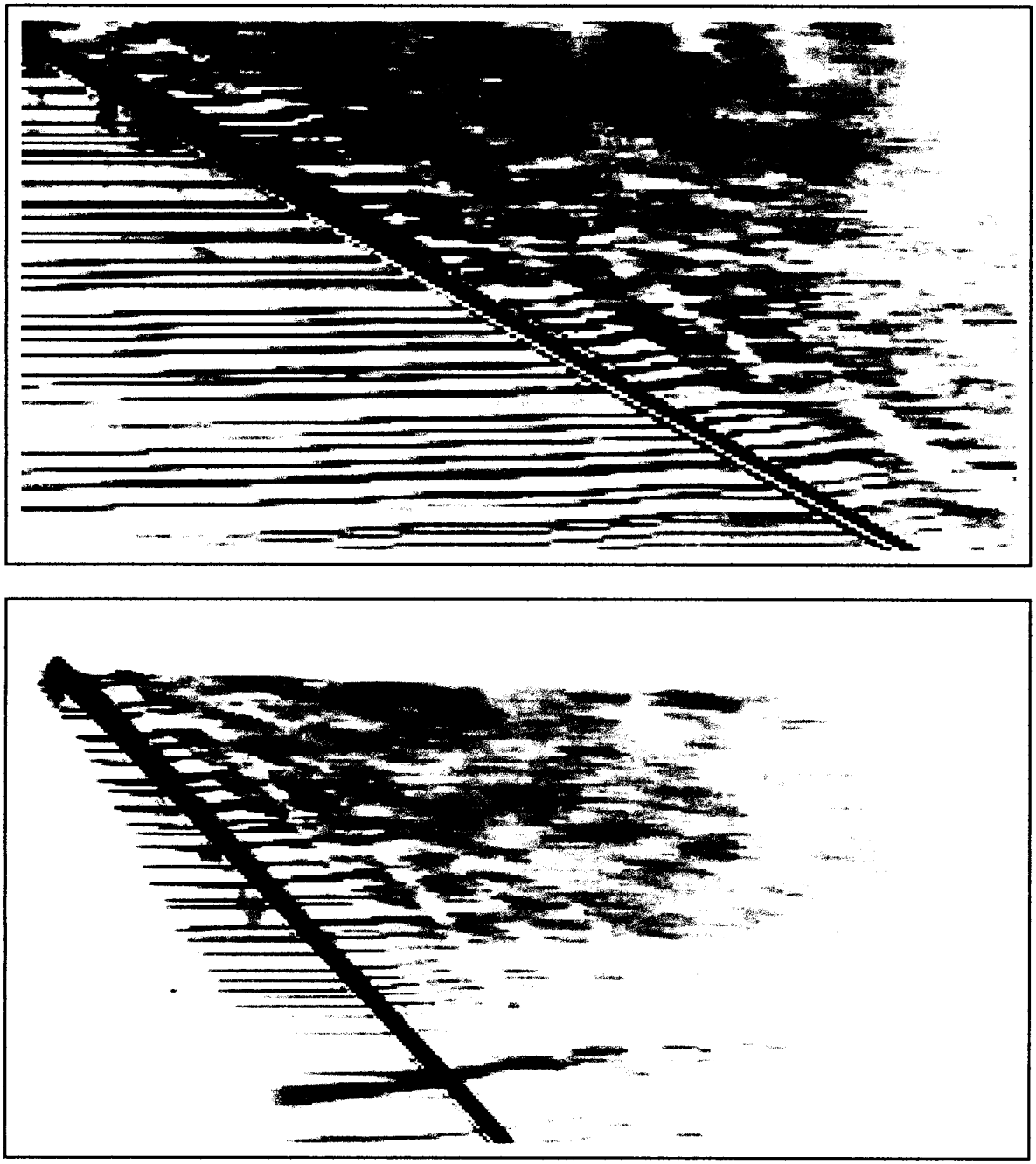

Figure 6.1 Flow visualisation of vortex lines using oil smoke in air.

Re_a = 260 (Re_d= 520), yaw angle β = 30°(upper), 45°(lower), flow direction ⇒.

As the cylinder yaw angle is decreased, the area of wake containing coherent vortices decreases. In the limiting case of axial flow, the area reduces to the boundary layer thickness on either side of the cylinder, approximately 20% of the area (and of the reflected light) of the normal flow case. This factor is particularly important in the present investigations of small yaw angles.

The combination of low camera shutter speeds and the high air-flow velocities required for the desired Reynolds numbers also degrades the final images: blurring of the smoke traces results from the movement during each exposure. The clarity of the images shown in Figure [6.1] was only achieved by the use of a relatively large cylinder diameter (d = 6 mm) to obtain the required Reynolds number at the minimum wind-tunnel flow speed. Increasing the cylinder diameter at smaller yaw angles is not practicable as the desired values of x/a for slender cylinders in near-axial flow would require a much longer wind-tunnel test section than that available.

For these reasons flow visualisation in water, with hydrogen bubbles, was selected as a better method of acquiring flow-visualisation images.

6.2 Visualisation of the Vortex Wake in Water

The advantages of conducting flow visualisation experiments in water rather than in air are largely a consequence of the kinematic viscosity of water being approximately fifteen times smaller. The same Reynolds numbers for the same cylinder diameter may then be obtained at a much lower free stream velocity and blurring of the images avoided.

The higher density and specific heat of water also decrease the temperature rise resulting from the high lighting power required. In addition the hydrogen bubbles used to render the flow patterns visible reflect more light than the much smaller smoke particles. The ease of achieving the correct conditions for a successful image is also greatly enhanced by the use of hydrogen bubbles in water as they may be generated continuously while lighting and camera settings are adjusted.

A laminar-flow recirculating water tunnel, shown in Figure [3.12], was designed and constructed following preliminary experiments using a water flume in the Civil Engineering department. These early experiments indicated the importance of a smooth laminar flow to the success of visualisation techniques in producing satisfactory images, and also served to develop suitable techniques and procedures for the generation and photography of the hydrogen bubbles.

A typical image of the "vortex street" obtained by hydrogen bubble flow visualisation is shown in Figure [6.2]. This image also confirms that the measured

periodic velocity fluctuations in the cylinder wake, presented in chapter five, result from regular vortex shedding alternately from opposite sides of the yawed cylinder.

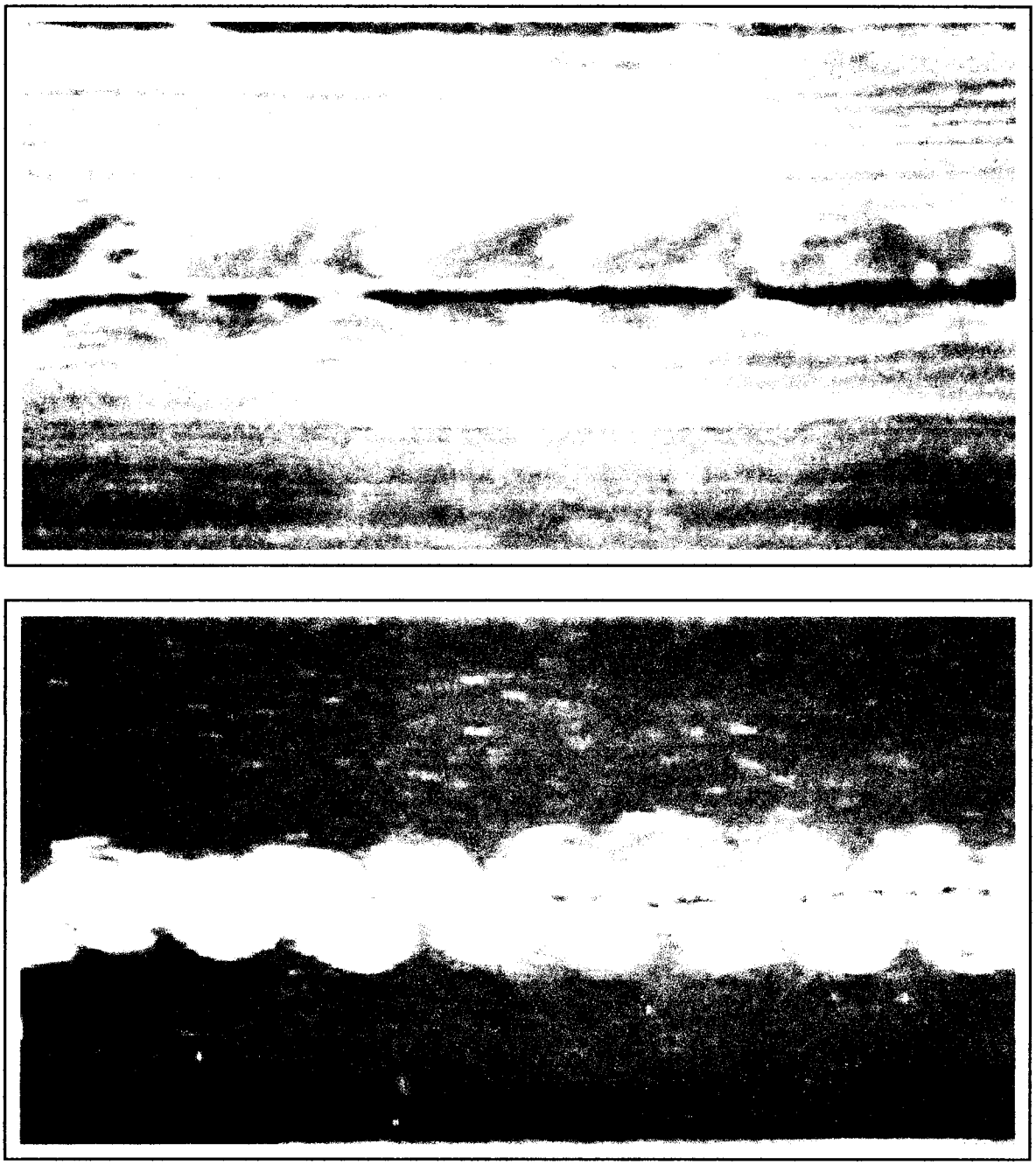

Figure 6.2 Flow visualisation of the "vortex street" using hydrogen bubbles in water.

Re_a = 200 (Re_d = 400), yaw angle β = 20°(upper), 30°(lower), flow direction ⇒.

6.3 Inclination of the Vortex Lines

As each vortex forms, the hydrogen bubbles, generated in the plane of cylinder yaw, become concentrated in the vortex core making the axes of a series of vortices visible. A series of images in this form has been presented previously by Bull and Dekkers (1992a, Appendix 2) and is extended here in Figure [6.3] for a series of yaw angles at constant Reynolds number $Re_a = 150$ ($Re_d = 300$).

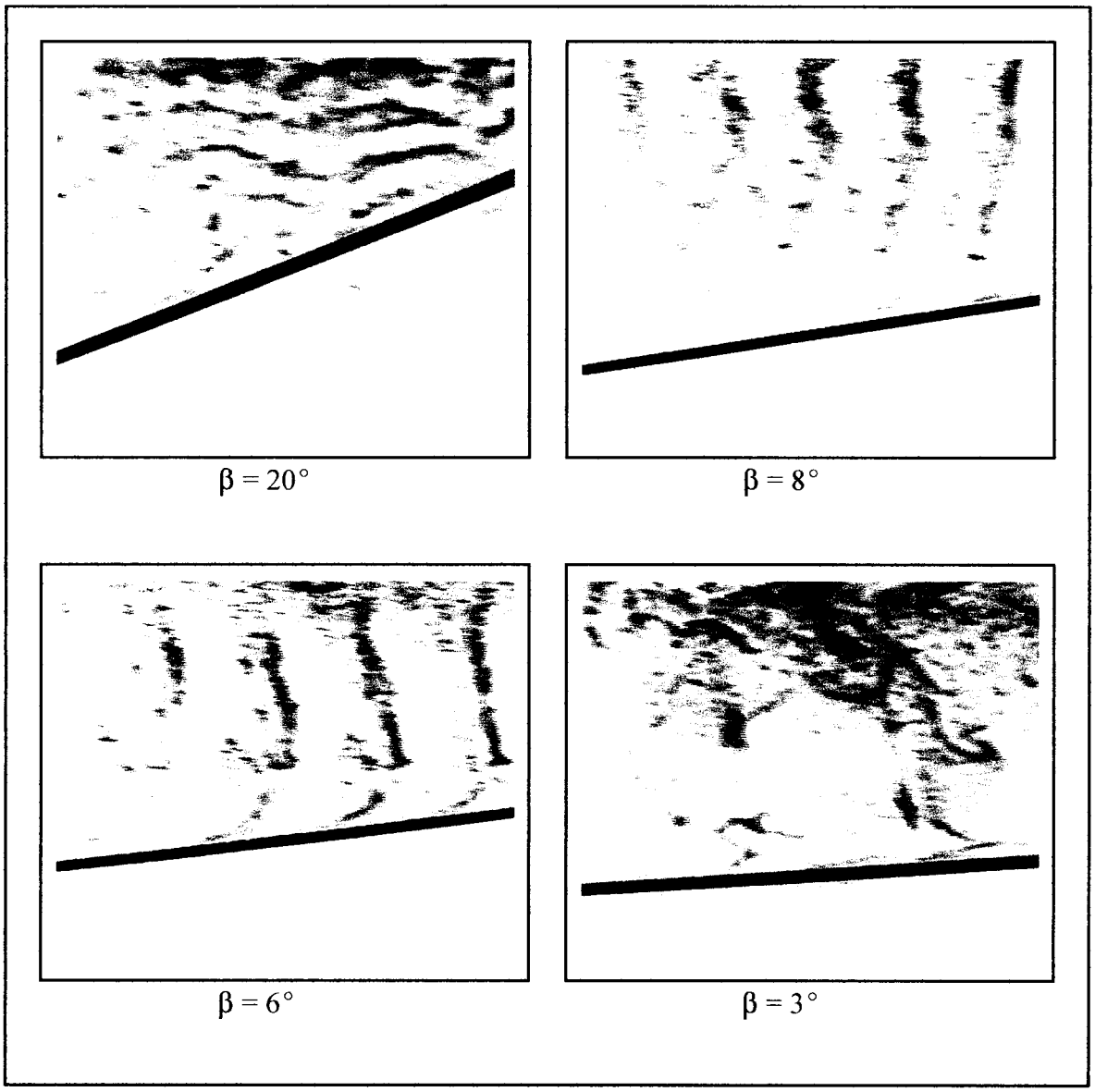

Figure 6.3 Flow visualisation of vortex lines using hydrogen bubbles in water. Various yaw angles at constant Reynolds number $Re_a = 150$ ($Re_d = 300$), flow direction ⇐.

The patterns of vortex lines were recorded on video tape for yaw angles over the range $2° < \beta < 30°$, and Reynolds numbers over the range $150 < Re_a < 300$ ($300 < Re_d < 600$). Images are shown in Figure [6.4] for different Reynolds numbers at constant yaw angle $\beta = 5°$. These digital images have been produced from single video frames to examine the effects of the experimental apparatus on the vortex shedding processes and to allow the vortex shedding angles to be measured.

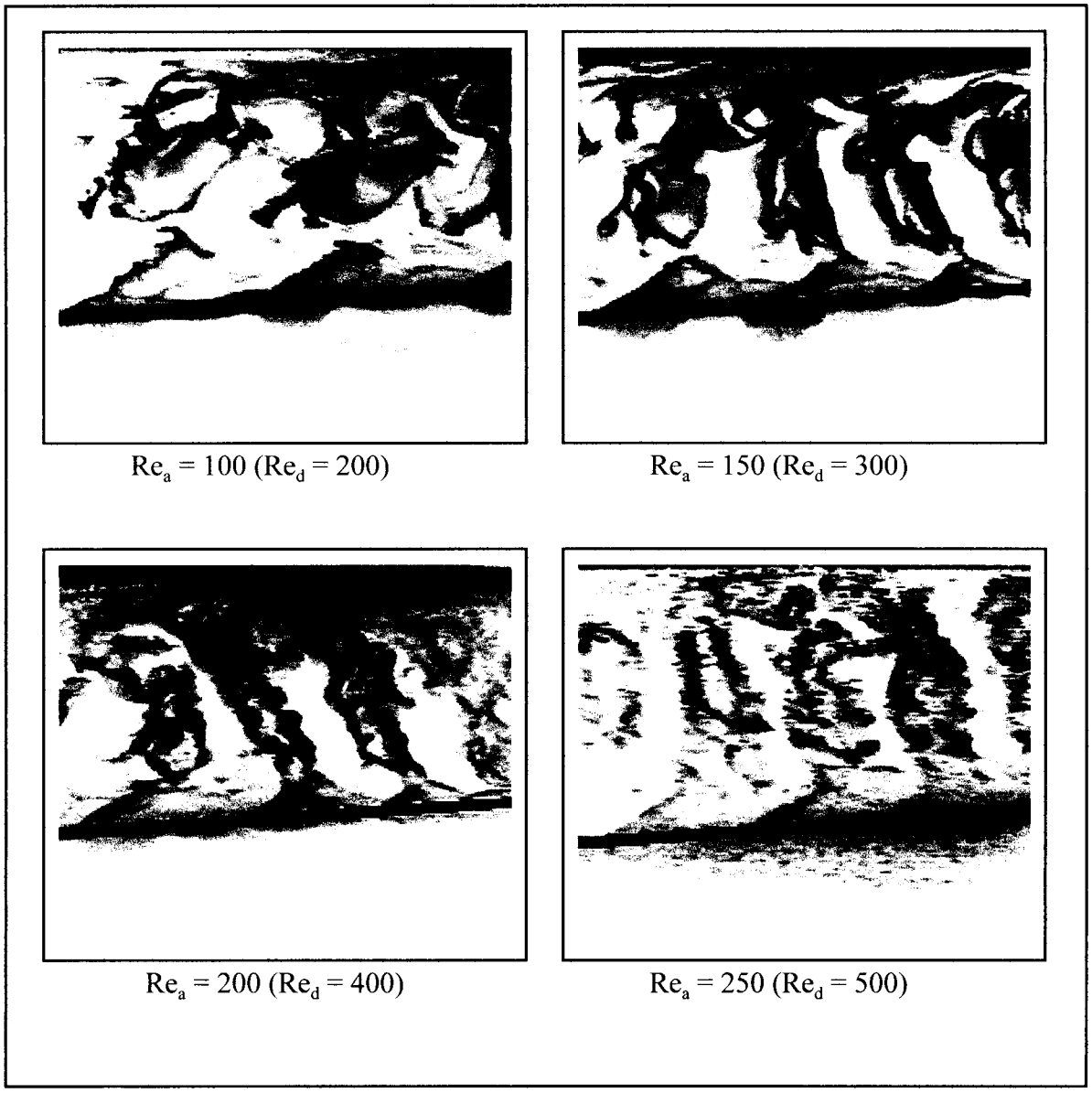

Figure 6.4 Visualisation of vortex lines using hydrogen bubbles in water.

Various Reynolds numbers at constant yaw angle $\beta = 5°$, flow direction $\Leftarrow$.

To satisfy the aim of interpreting the flow visualisation images in terms of a single vortex-shedding angle requires some understanding of the complexity of the three dimensional flow structure of the wake, and of the effects on the flow of the experimental arrangement. Factors to be considered are:

the effects of the cylinder end conditions,

the effects of the water-tunnel boundary conditions on the flow,

the effects of the presence of the hydrogen-bubble wire on the vortex wake,

the effects of the finite width of the lighting plane.

The use of extremely long cylinders is expected to minimise the effects of the particular cylinder end conditions used, as the ends are hundreds of cylinder-diameters away from the measuring positions. On the other hand, the flow boundaries are much closer to the area of investigation. As each vortex is shed from the cylinder and moves downstream, the vortex lines must extend outwards to the boundary of the fluid, or intersect and merge with other vortex lines which themselves extend to the flow boundary.

In the experimental arrangement used here, vortex lines are formed on the upper side of the cylinder, and extend outwards from the cylinder to terminate at the free surface of the water flow. As originally reported by Bull and Dekkers (1992b, Appendix 3) and Dekkers and Bull (1992, Appendix 6), at large angles of yaw ($\beta > 20°$) the visible vortex line appears as a straight line inclined to the cylinder axis by a small angle $\alpha°$; however, at smaller yaw angles ($\beta < 8°$), the vortex lines appear to curve and change in inclination to the cylinder axis as they extend outwards from the cylinder. It is proposed here that this curvature is simply a result of the increase in the

mean velocity of the wake with distance downstream of the cylinder, as the wake flow is re-accelerated by the surrounding free-stream flow.

The termination of vortex lines at the free surface of the water flow may also affect the inclination of a vortex at the outer extremity of the flow. Both of these mechanisms will tend to change the vortex orientation after the initial formation.

The wire used as a cathode to generate hydrogen bubbles has a diameter of 100μm. At the maximum flow velocity the wire Reynolds number is less than 33, which is lower than the minimum Reynolds number for vortex shedding from a cylinder normal to the flow.

Although the bubble wire will not have a vortex wake, its presence may still disturb the formation of the cylinder vortices. The vertical position of the abrupt change in vortex-line orientation shown in Figure [6.3] for a yaw angle of 8° corresponds to the position of the intersection point of the hydrogen bubble wire and the test cylinder further upstream (see Figure [6.5]). As in the experimental effects discussed previously, the vortex orientation beneath this disturbance appears to be that of the undisturbed vortex oriented at its initial formation angle.

The final experimental effect is that of the finite width of the lighting plane. Although the hydrogen bubbles are initially formed in a very thin vertical plane, they are spread outwards normal to the plane of yaw as they are entrained into the vortex wake. As the "sheet" of light illuminating the plane of yaw has a thickness of several millimetres, but is thinner than the width of the wake, the resulting image is of a thin

slice of the wake, with bubbles in front of and behind the plane of yaw appearing in the image in addition to the desired particles within the yaw plane. This three-dimensional structure superimposed on the two-dimensional image blurs the finer detail of the wake, but does not obscure the principal structure of the orientation of the vortex cores.

Each flow visualisation image has to be interpreted in the light of these considerations of the experimental effects. The initial vortex-shedding angle is measured as shown in Figure [6.5] from each video frame, and an average angle over ten measurements determined for each Reynolds-number / yaw-angle combination. The variation of the average vortex-shedding angle α with cylinder yaw angle β is shown in

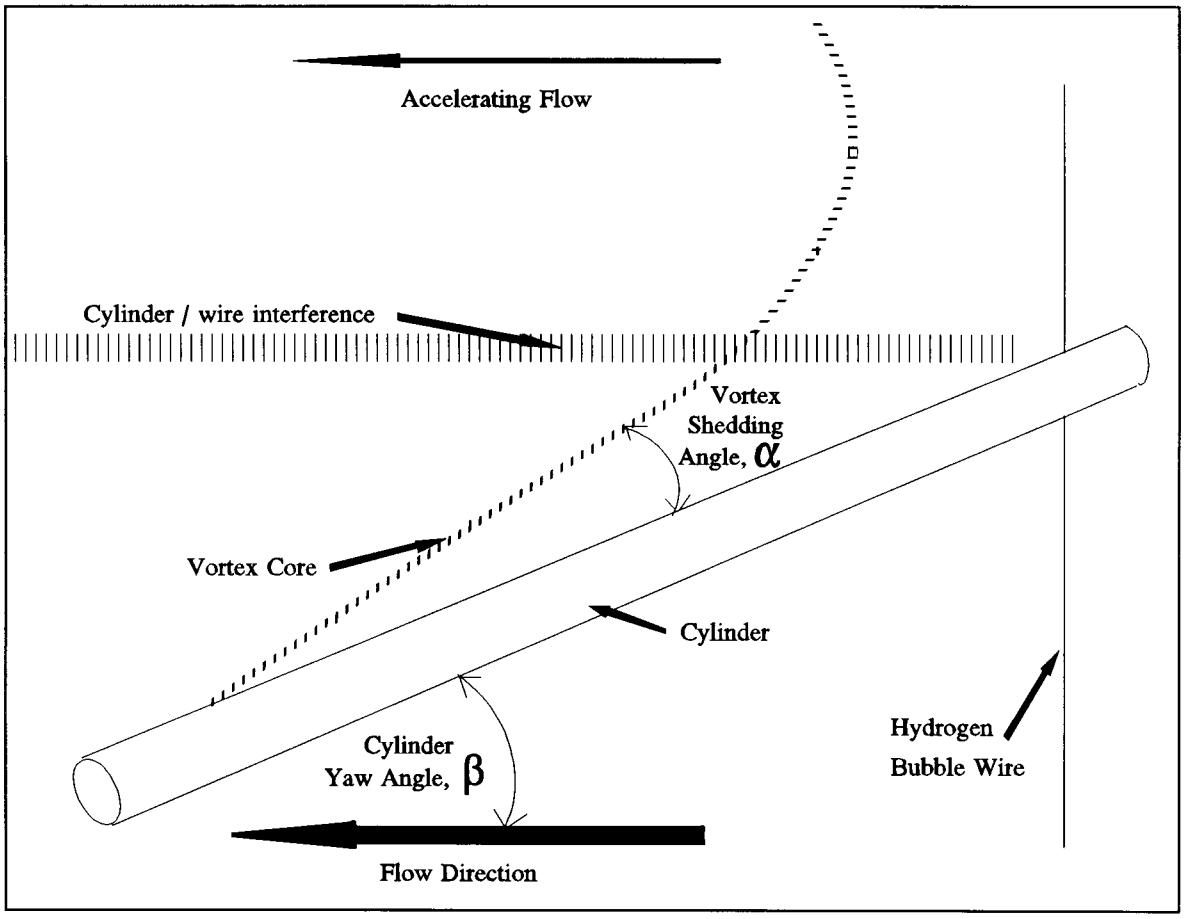

Figure 6.5 The vortex shedding angle α determined as the initial angle of formation of the vortex line relative to the cylinder axis.

Figure [6.6] for various Reynolds numbers Re_a. As expected, the angle α increases as the yaw angle decreases, corresponding to an increase in axial vorticity with increasing axial velocity component as the yaw angle is decreased. These results confirm the theoretical predictions of Ramberg (1983) for the orientation of the vortex axes in the absence of cylinder end effects and other experimental effects on the flow.

The variation of the vortex-shedding angle with Reynolds number for a constant cylinder yaw angle of $\beta = 5°$ is shown in Figure [6.7]. The essentially constant value of α suggests that the shedding angle is relatively insensitive to the Reynolds number, and thus is predominantly a function of the cylinder yaw angle only.

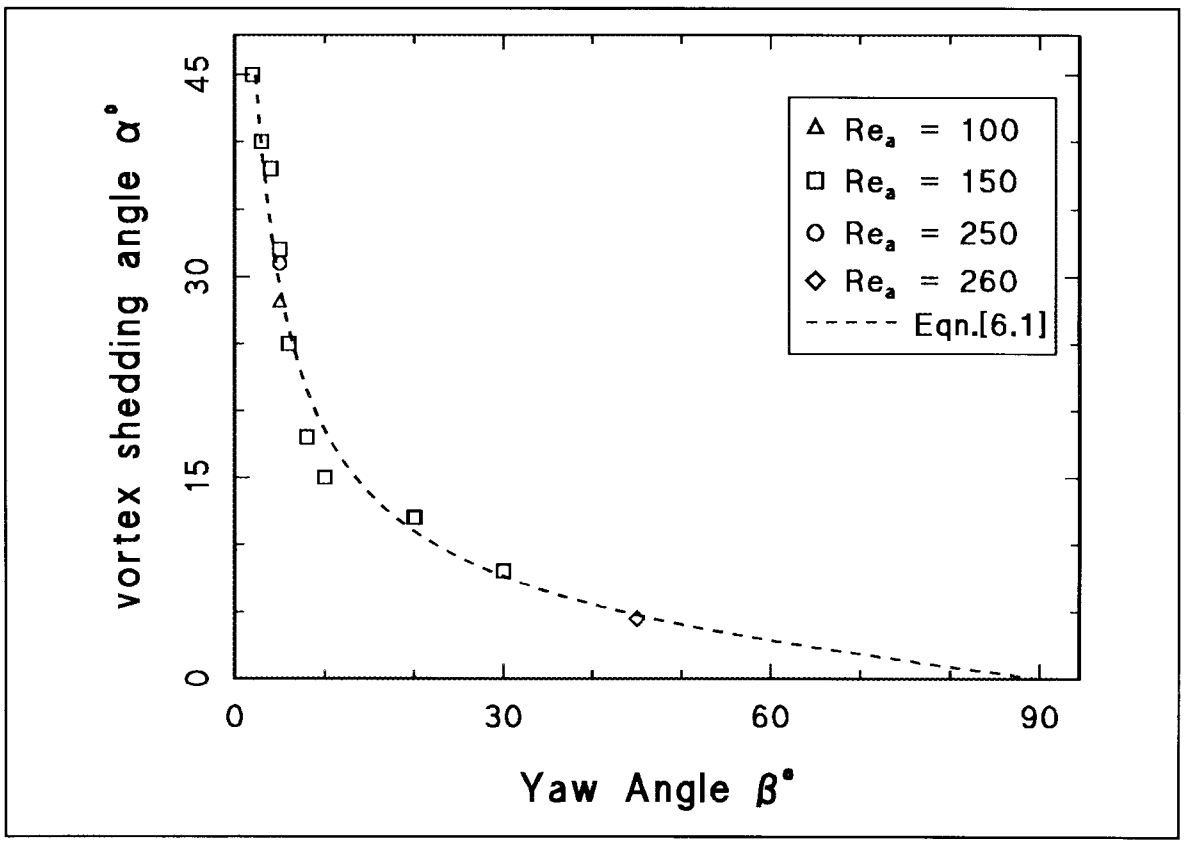

Figure 6.6 Variation of vortex orientation α relative to the cylinder axis with cylinder yaw angle β, for various Reynolds numbers Re_a.

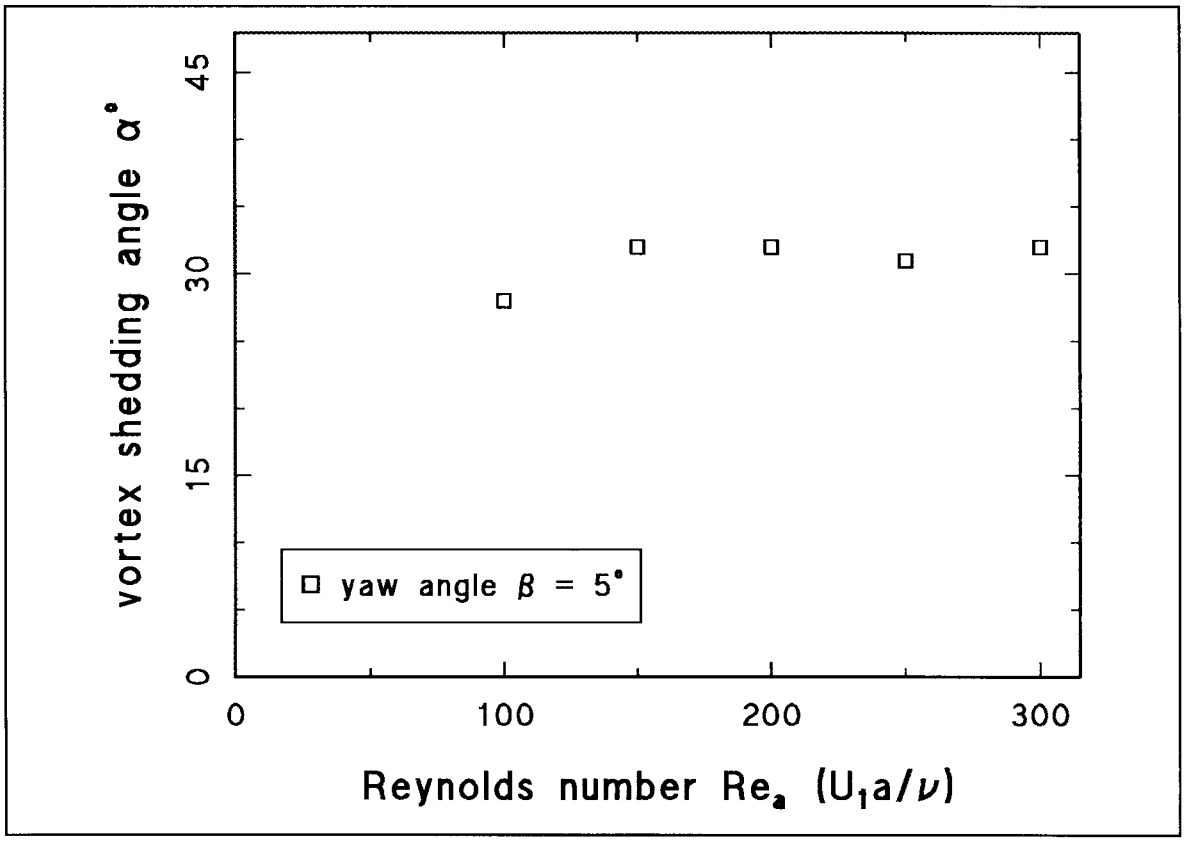

Figure 6.7 Variation of vortex orientation α relative to the cylinder axis with Reynolds number for yaw angle $\beta = 5°$.

The relation between vortex angle and yaw angle can be represented quite well by the empical formula

$$\cos\alpha = \frac{170 \sin^{4/3}\beta}{1 + 169 \sin^{4/3}\beta} , \qquad [6.1]$$

which satisfies the conditions $\alpha = 0$ at $\beta = \pi/2$ (parallel vortex-shedding for cylinders normal to the free stream) and $\alpha = \pi/2$ at $\beta = 0$. This relation is shown in Figure [6.6].

These flow visualisation results may now be considered in conjunction with the results of the vortex-shedding frequency measurements to establish the effects of the axial velocity component on the vortex-shedding frequency, and to examine the contributions of the velocity and associated vorticity components to the structure of the vortex wake.

6.4 The Effect of the Axial Velocity Component

In this section the vortex-shedding properties of yawed cylinders are examined against the datum case of cylinders normal to the flow. Consequently the results are presented in terms of Reynolds number Re_d, the conventional Reynolds number for normal cylinder flow, rather than in terms of Re_a. In the absence of any effect of the axial velocity component, the effects of cylinder yaw angle would be simple: vortex shedding would be expected to occur with vortex axes parallel to the cylinder axis, and at a frequency corresponding to shedding from a cylinder normal to a flow with a free stream velocity of $U_1 \sin\beta$ equal to the component of velocity normal to the axis of the yawed cylinder. This is the "independence principle".

The effect of the axial velocity component thus becomes apparent in two ways: firstly in any inclination of the vortex axes to the cylinder axis, and secondly in any deviation of the vortex shedding frequency from that calculated using the independence principle. The extent of the deviation from the independence principle for the first case is given directly by the vortex-shedding-angle data shown in Figure [6.6].

In order to examine the second form of deviation of the vortex-shedding behaviour from the parallel shedding which would be associated with the validity of the independence principle, it is necessary to compare the measured vortex-shedding frequencies with those predicted by the independence principle. The latter can be calculated by Roshko's (1954) empirical linear relationships (for $\beta = 90°$) for the frequency parameter F as a function of the Reynolds number Re_d (Equations [2.1] and

[2.2]) using the normal Reynolds number, $Re_n = Re_d \sin \beta$ to replace Re_d. According to the independence principle, equations [2.1] and [2.2] for cylinders normal to the flow become

$$50 < Re_n < 150 \qquad F_n = 0.212\ Re_n - 4.5 \qquad [6.2]$$

$$300 < Re_n < 2000 \qquad F_n = 0.212\ Re_n - 2.7 \qquad [6.3]$$

for cylinders yawed to the flow.

The measured and predicted frequencies are compared over a range of yaw angles and Reynolds numbers, as the ratio F/F_n, in Figure [6.8], where Re_n is within the limits of the Equations [6.2] and [6.3].

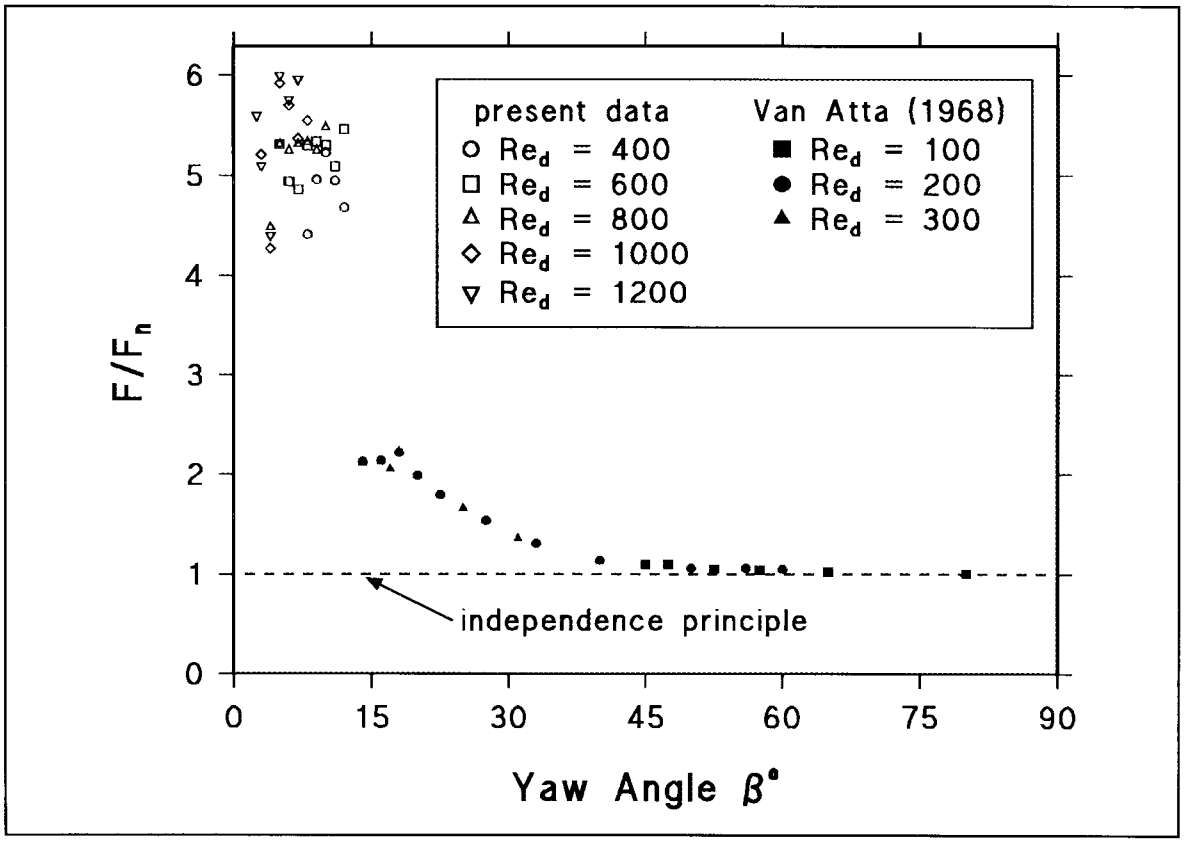

Figure 6.8 The ratio F/F_n for a range of yaw angle β, at different Re_d ($= 2Re_a$).

The results of Van Atta (1968) indicate that, for all large yaw angles, typically $> 45°$, F/F_n is close to unity and converges to this value as the yaw angle approaches 90°. However, both Van Atta's data and the present data diverge from the independence-principle predictions when the yaw angle is reduced below 45°, and dramatically so at very small β approaching axial flow.

As the results for the vortex-shedding angle, shown in Figure [6.6], and the vortex-shedding frequency, shown in Figure [6.8], both indicate a significant divergence of the vortex-shedding mechanism from dependence on only the normal velocity component, an alternative description of the vortex mechanisms is required. To formulate such a description the component of the free stream velocity which most directly affects the frequency and orientation of the vortices has to be identified. At large yaw angles ($\beta > 45°$) the relevant velocity component is that normal to both the cylinder axis and the vortex axis. It is suggested that the more appropriate characteristic velocity component, for both large and small yaw angles is that normal to the vortex axes. An alternative description will now be derived on this basis.

Thus, rather than dividing the free stream velocity U_1 into components normal to and parallel to the cylinder axis, as in the independence principle, which predicts parallel vortex shedding with a frequency determined by the normal component, U_1 is resolved into two orthogonal components normal to and parallel to the resulting vortex axes. The component normal to the vortex axes is considered to be the sole determinant of the vortex-shedding frequency; this will be termed the effective velocity component U^*. The component parallel to the vortex axes is considered to have no effect on the vortex-shedding frequency, and will be termed the ineffective velocity component U_{inef}.

The definitions of these velocity components, and the associated angles are shown in Figure [6.9]; the effective velocity component U^* is

$$U^* = U_1 \sin(\alpha + \beta). \qquad [6.4]$$

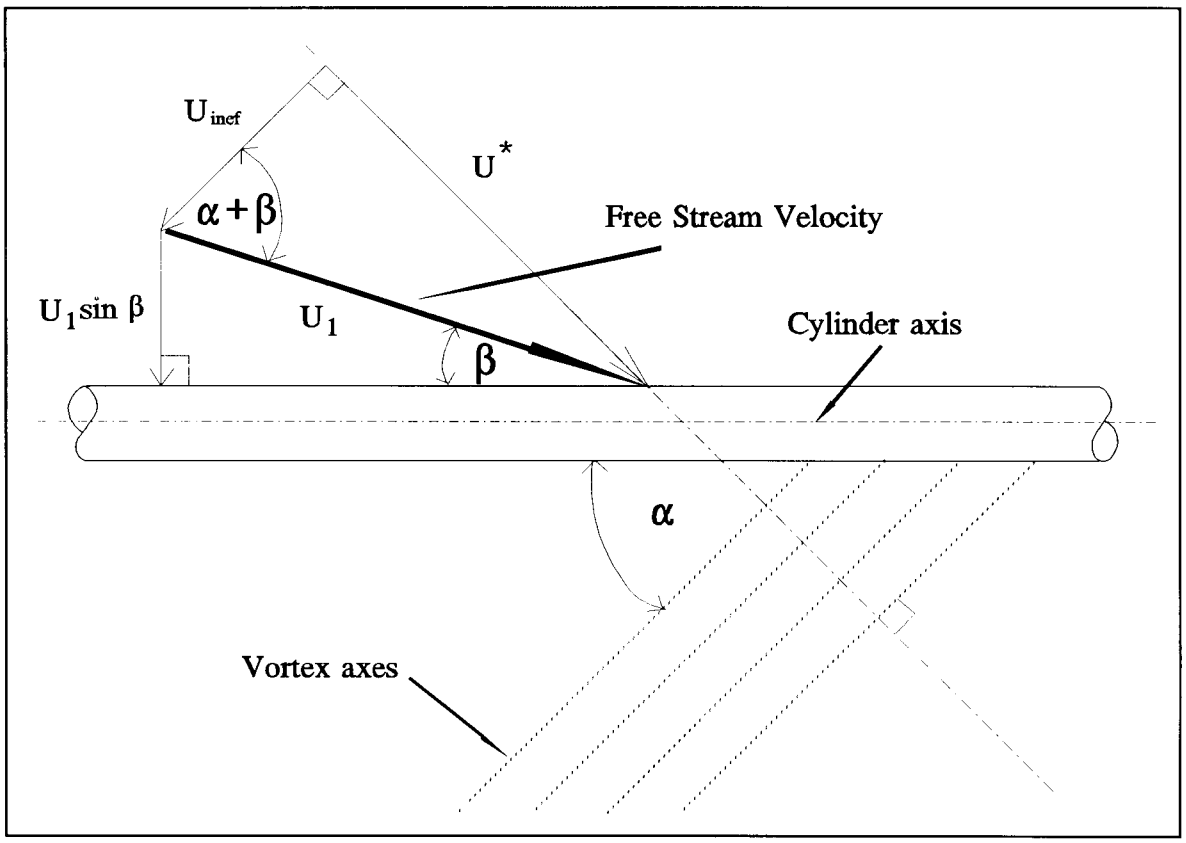

Figure 6.9 Definition of the effective velocity component U^* and the ineffective velocity component U_{inef}, in terms of the cylinder yaw angle β and the vortex shedding angle α.

The orientation, and thus the magnitude, of the effective velocity U^* is determined by the angle $(\alpha+\beta)$, which is obtained from the vortex-shedding-angle data of Figures [6.6] and [6.7]. As the vortex-shedding angle α is largely independent of Reynolds number (Figure [6.7]), $(\alpha+\beta)$ will be considered to be a function of cylinder yaw angle only. The empirical function equation [6.1], fitted to the data of Figure

[6.6], can be used to express $(\alpha+\beta)$ as a function of β, as shown in Figure [6.10]. As noted in section 6.3, the resulting function, as required, approaches unity as the yaw angle approaches 90°, thus representing vortex shedding parallel to the axis of a cylinder normal to the flow. This empirical function may now be used to determine the orientation of both the vortex axes and the effective velocity component U^*, and in conjunction with the free-stream velocity and the cylinder yaw angle, the magnitude of U^*.

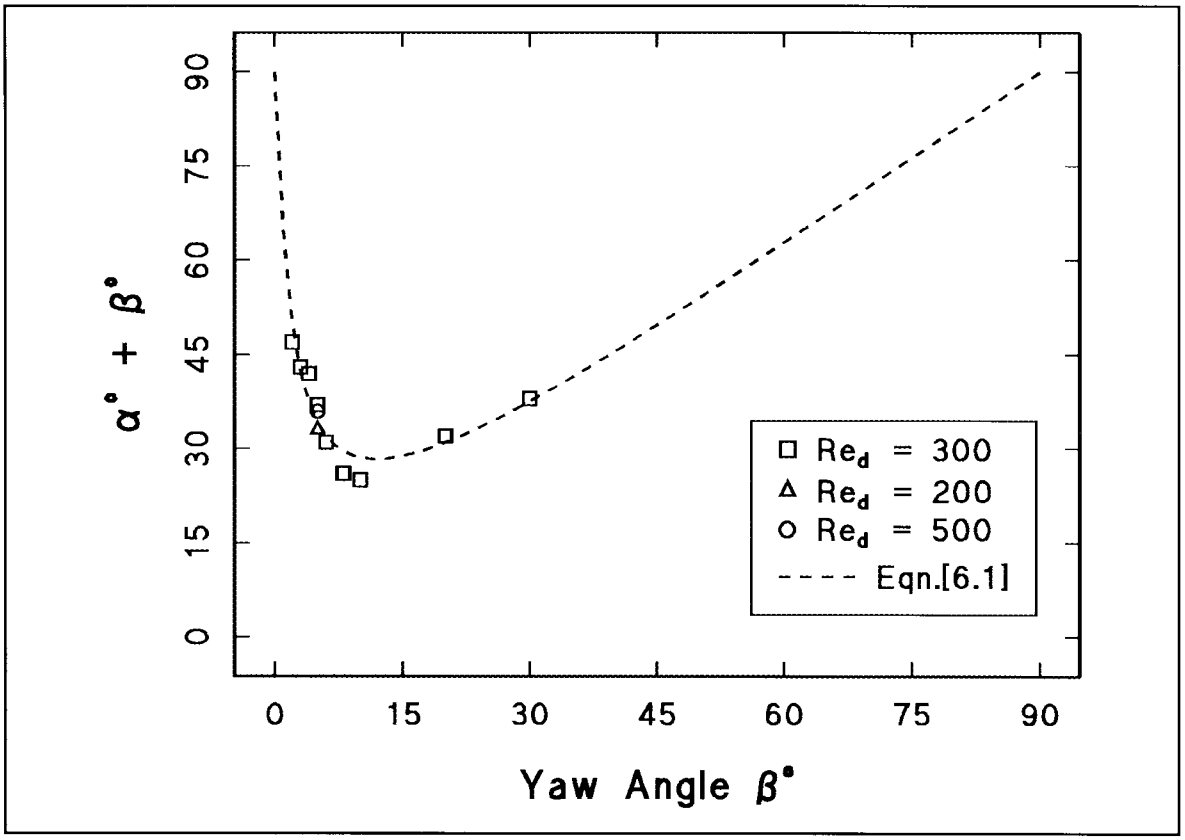

Figure 6.10 Angle of inclination of vortex axis to free-stream direction, $(\alpha+\beta)$, as a function of yaw angle.

The effective velocity falls between the free stream velocity and the normal velocity component, as U^* must be less than U_1, and for positive shedding angles must be greater than the normal velocity component $U_1\sin\beta$. Values of $(\alpha+\beta)$ derived from

Equation [6.1] are also concistent with the conclusion, based on the measured vortex-shedding frequencies shown in Figure [6.8], that the axial velocity contribution to the vortex shedding process is negligible for yaw angles greater than about 45°.

Introduction of a velocity component U^* characteristic of the vortex-shedding process, and an effective characteristic cylinder diameter d^*, allows the standard empirical relationships between frequency parameter and Reynolds number for cylinders normal to the flow, as determined by Roshko (1954), to be extended to cylinders in near-axial flow. The fundamental assumption required here is that there exists a universal relationship between a generalised frequency parameter $F^* = fd^{*2}/\nu$ and a generalised Reynolds number $Re_d^* = U^*d^*/\nu$. Hence, for cylinders yawed to the flow, Equations [2.1] and [2.2] applicable to cylinders normal to the flow now become

$$50 < Re_d^* < 150 \qquad F^* = 0.212\ Re_d^* - 4.5 \qquad [6.4]$$

$$300 < Re_d^* < 2000 \qquad F^* = 0.212\ Re_d^* - 2.7 \qquad [6.5]$$

These relations are of the form

$$F\left(\frac{d^*}{d}\right)^2 = B_R Re_d \left(\frac{d^*}{d}\right) \sin(\alpha+\beta) - C_R$$

$$= X\left(\frac{d^*}{d}\right) - C_R$$

where $X = B_R Re_d \sin(\alpha+\beta)$ and B_R (= 0.212) and C_R (= 4.5 or 2.7) are the Roshko constants. Thus, with $(\alpha+\beta)$ established as a function of β, d^*/d can be determined from the frequency parameter F measured at any given yaw angle and Reynolds number as

$$\frac{d^*}{d} = \frac{X + \sqrt{(X^2 - 4FC_R)}}{2F} \qquad [6.6]$$

Values of d^*/d derived in this way are shown as a function of Re_d in Figure [6.11] (upper) for ($0.5° \leq \beta \leq 5°$) and Figure [6.11] (lower) for ($6° \leq \beta \leq 12°$). The dependence of d^*/d on Reynolds number Re_d and cylinder yaw angle β (in degrees), as shown in the figures, can be quite well represented empirically as

$$\frac{d^*}{d} = A + Be^{-kR}, \qquad [6.7]$$

where $R = (Re_d/1000)$ and A, B and k are yaw-angle-dependent parameters given by

$$A = [1 + 0.08(90-\beta)/\beta - \{(90-\beta)/68.5\}^2], \qquad [6.8]$$

$$B = 0.314[(90/\beta)^{0.79} - 1], \qquad [6.9]$$

and $$k = 0.363(\beta-1) - 0.014\,\beta^2. \qquad [6.10]$$

The experimental data for all the combinations of Reynolds number Re_d and yaw angle β which have been examined, converted to their generalised forms, are compared with the generalised form of Roshko's relation (equation 6.4, 6.5) in Figure [6.12].

The values shown have been obtained by calculating effective cylinder diameters by equations [6.7] - [6.10] and vortex angles by equation [6.1], and applying the calculated values to the experimental frequency parameters F and Reynolds numbers Re_d. There is quite good agreement between the experimentally-based data and the generalised Roshko relations, indicating that the latter, in conjunction with the empirical relations, equations [6.1], [6.7] - [6.10], can be used for effective prediction of the vortex-shedding frequencies of yawed cylinders in near-axial flow. Direct

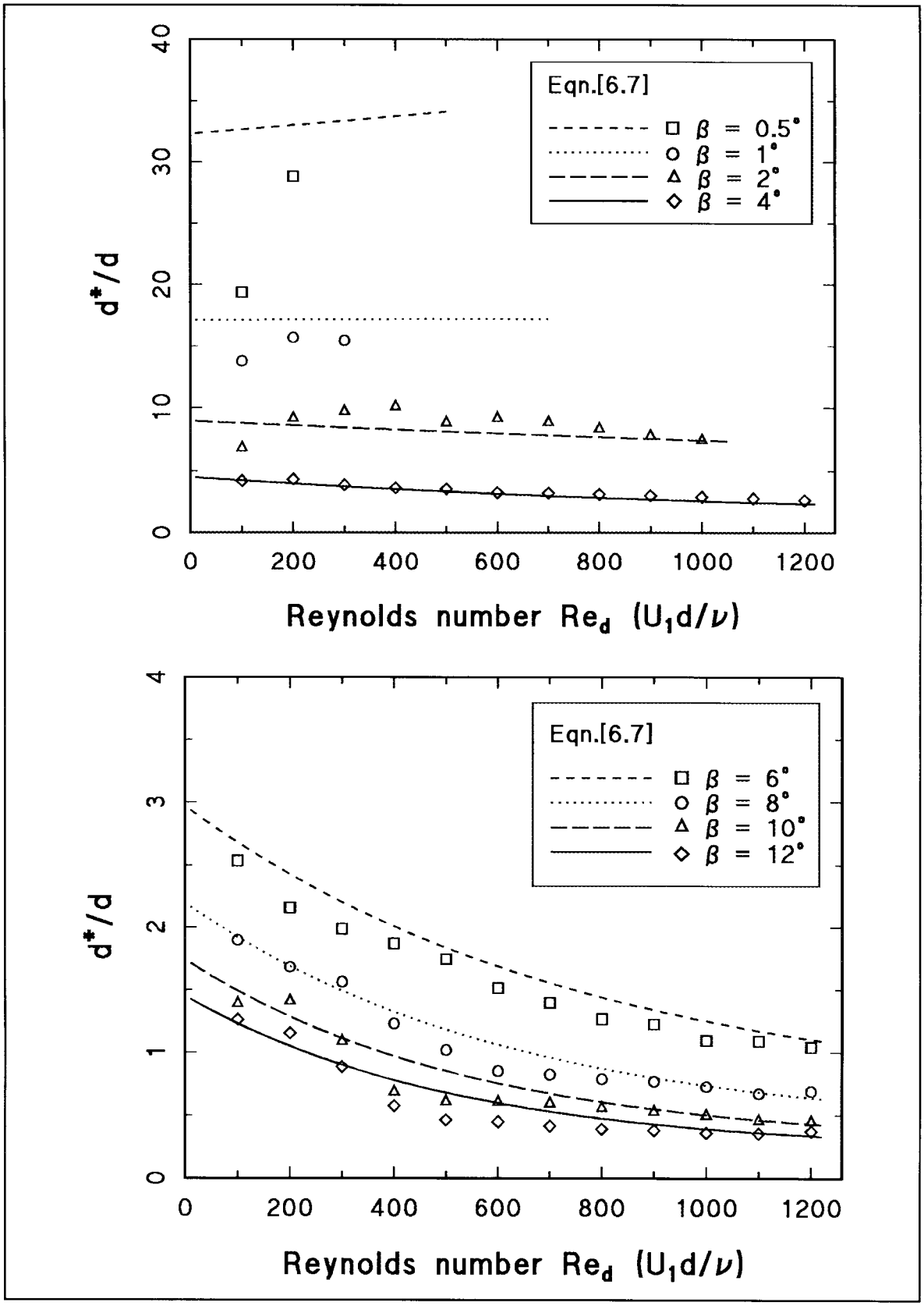

Figure 6.11 Derived values of d^*/d as a function of Re_d, for a range of yaw angles $0.5° \leq \beta \leq 5°$ (upper) and $6° \leq \beta \leq 12°$ (lower).

comparisons of measured values of frequency parameter F and their empirical representations, based on the generalised Roshko formula, are shown as a function of Reynolds number Re_d for selected values of yaw angle in Figure [6.13].

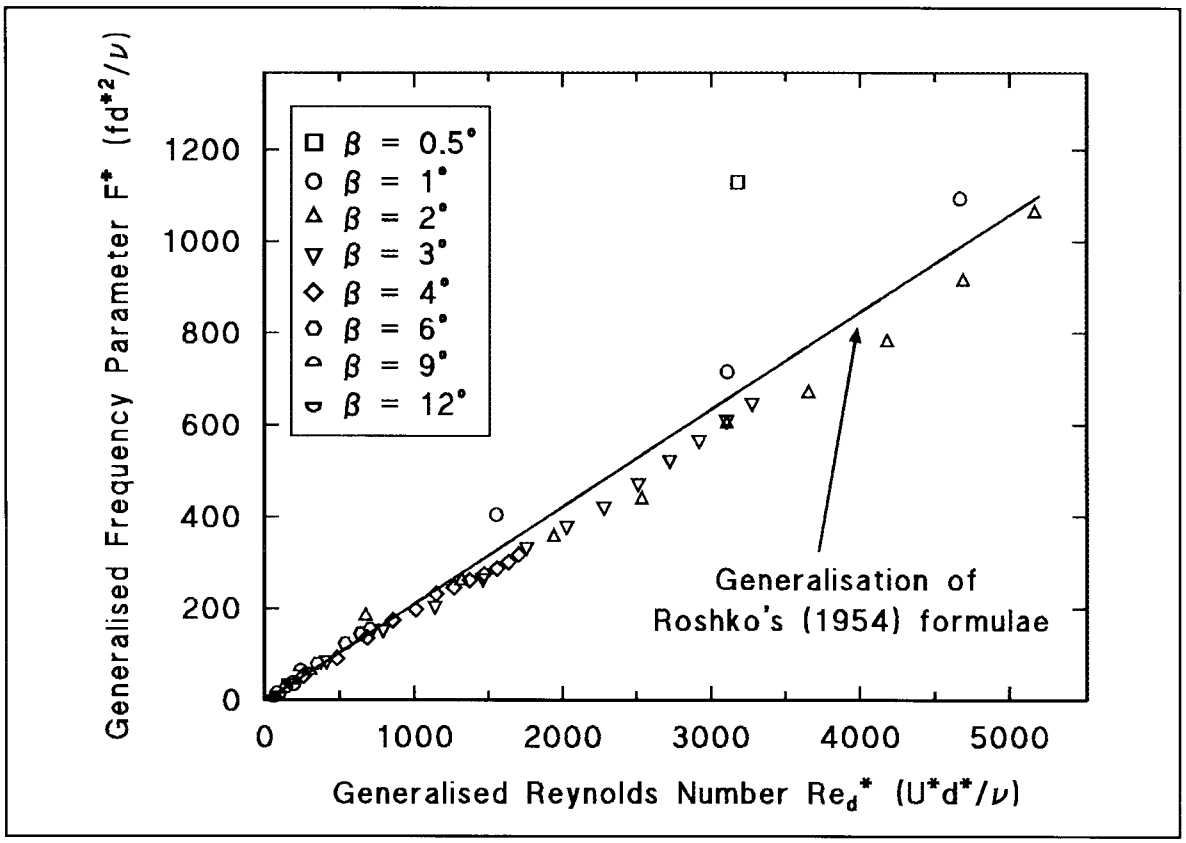

Figure 6.12 Variation of generalised Frequency parameter F^* with generalised Reynolds number Re_d^* for yaw angles in the range $0.5° \leq \beta \leq 12°$, and Reynolds numbers in the range $100 \leq Re_d \leq 1200$, and comparison with the generalised form of Roshko's equation.

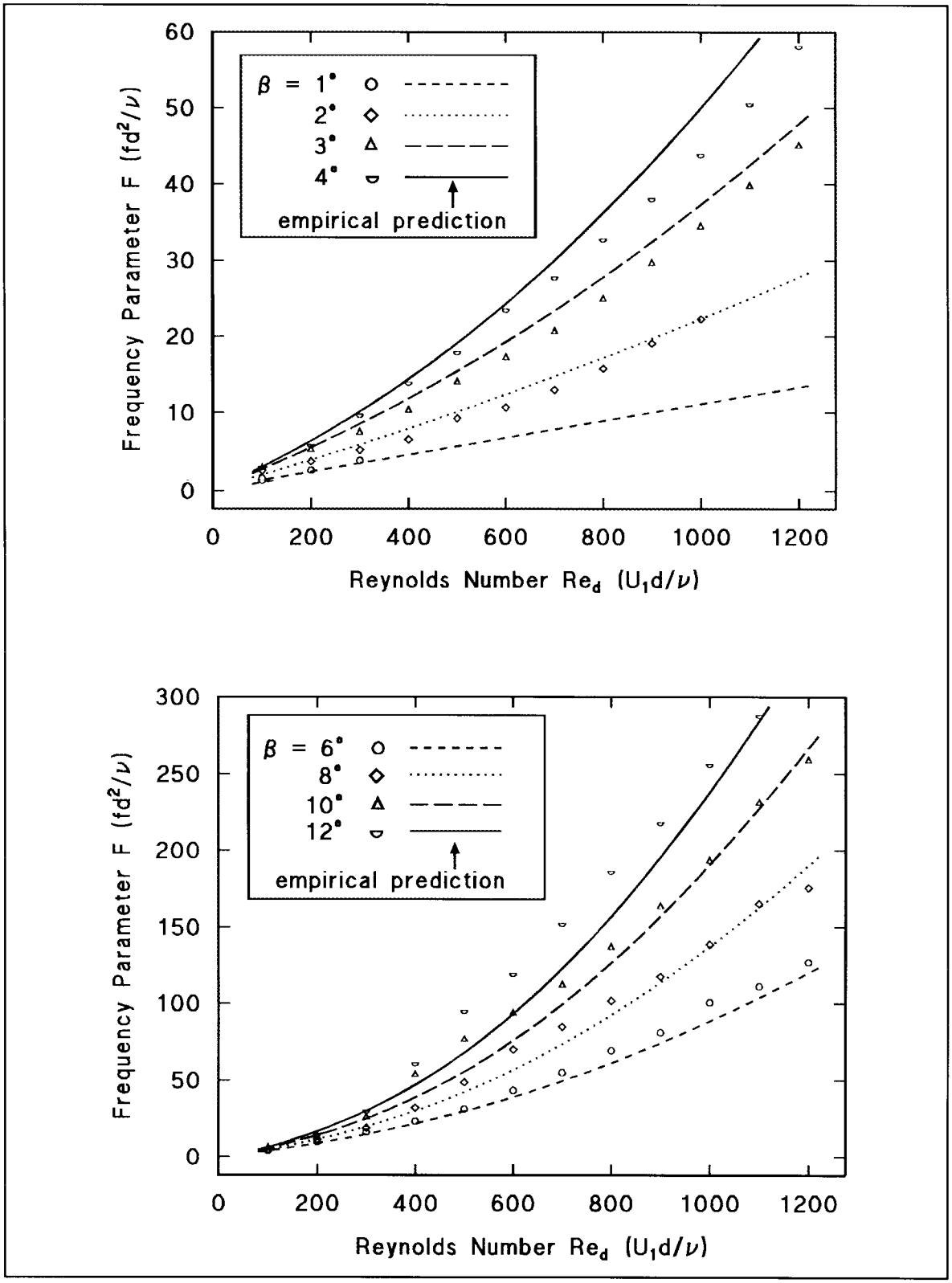

Figure 6.13 Variation of Frequency Parameter F with Reynolds number Re_d for constant yaw angles spanning the range of investigation, d = 0.9 mm, with their empirical representations based on the generalised Roshko formula.

6.5 Summary of Results

Images of the wakes of yawed cylinders obtained by hydrogen-bubble flow-visualisation in the water-tunnel confirm that the velocity oscillations considered in chapter five are associated with regular vortex shedding and the formation of a vortex street.

Visualisation of the vortex axes in the plane of cylinder yaw demonstrates that the vortex axes are inclined to the cylinder axis, in accord with the predictions of Ramberg (1983). The angle of vortex inclination approaches zero asymptotically as the cylinder yaw angle approaches 90°; almost parallel shedding persists for yaw angles down to about 45°. The latter result explains the fortuitous success of the independence principle in predicting the shedding frequency for large yaw angles. The significance of both the axial vorticity component and the axial velocity component in determining the vortex-shedding angle and the vortex-shedding frequency is found to increase greatly at small yaw angles.

Measured vortex-shedding frequencies and angles, over a range of yaw angles and Reynolds numbers, have been used to form empirical relationships which allow the existing well-established formulae of Roshko (1954) for cylinders normal to the flow to be used for the prediction of these parameters. From the experimental data, relationships between yaw angle and vortex-shedding angle (equation 6.1), and between actual cylinder diameter and an effective cylinder diameter (equation 6.6) have been derived. These allow evaluation of a generalised Reynolds number from which the

value of a generalised frequency parameter can be obtained from the Roshko formulae.

In the standard application of the Roshko formulae, for a cylinder normal to the flow, the vortex and cylinder axes coincide. The success of the yawed-cylinder correlation depends on the recognition that in the yawed-cylinder case, where the vortex and cylinder axes do not coincide, the flow conditions should be referred to the axis of the vortex rather than the axis of the cylinder.

7. EXPERIMENTAL INVESTIGATION OF FLOW MECHANISMS IN THE THICK AXISYMMETRIC BOUNDARY LAYER

The results presented in this chapter relate to the aim of identifying the effects of large transverse curvature on an axisymmetric boundary layer. As indicated in chapter four, the occurrence of frequent irregular negative velocity spikes, so-called "low-speed spots", in the very thick axisymmetric layers (Luxton et al., 1984; Bull and Dekkers, 1993b, Appendix 5) has been identified as a characteristic feature of the turbulence. Hence an attempt has been made to identify the flow processes by which these low speed spots are generated and the way in which they may be involved in turbulence generation.

Both flow visualisation and velocity measurements have been used to examine the characteristics and motion of the low speed spots within the boundary layer with a view to determining: the extent of the spots as coherent structures; the trajectories of their motion through the boundary layer; and the relation of their motion to that of the surrounding turbulence. It is then relevant to determine the magnitude and direction of the radial flow on the opposite side of the cylinder at the time of detection of a spot, and the associated variation of axial velocity with angular position around the cylinder.

The experiments have been concentrated on boundary layers for which the ratio of boundary-layer thickness to cylinder radius δ/a has values in the range 30 - 42.

7.1 Visualisation of Low-speed Spots

Images of the flow structure in the axisymmetric turbulent boundary layer in water were obtained by the hydrogen bubble method. Typical video frames of the flow along the cylinder at a Reynolds number $Re_a = 150$, with $\delta/a \approx 41$, are shown in Figure [7.1]. The most notable feature of these images is the absence of the periodic structures that were observed when the cylinder was slightly yawed to the flow, presented in chapter six. A second feature to note is the discrete structures which appear to be movements of fluid outwards from the cylinder surface. Similar images, obtained for axial flow at other Reynolds numbers, are shown as single video frames in Figure [7.2]. Within the limited range of Reynolds number investigated, there does not appear to be any significant variation of the flow structures with Reynolds number. A deterioration in image quality with increasing Reynolds number is apparent, as already seen in the near axial case. Some improvement of the image obtained at higher Reynolds numbers can be achieved by the use of a kinked bubble wire, as used for the last image of Figure [7.2]. This method produces lines of larger bubbles which are more visible at higher speeds than are the very fine bubbles formed by a straight wire.

A common feature of the images is a line of bubbles extending outwards from the cylinder surface, typically at an angle of about 45° to the downstream direction. Some of these linear structures appear to roll up to form vortices near the outer edge of the boundary layer. This suggests that vorticity associated with the higher velocity gradients near the cylinder surface is being transported into the outer boundary layer.

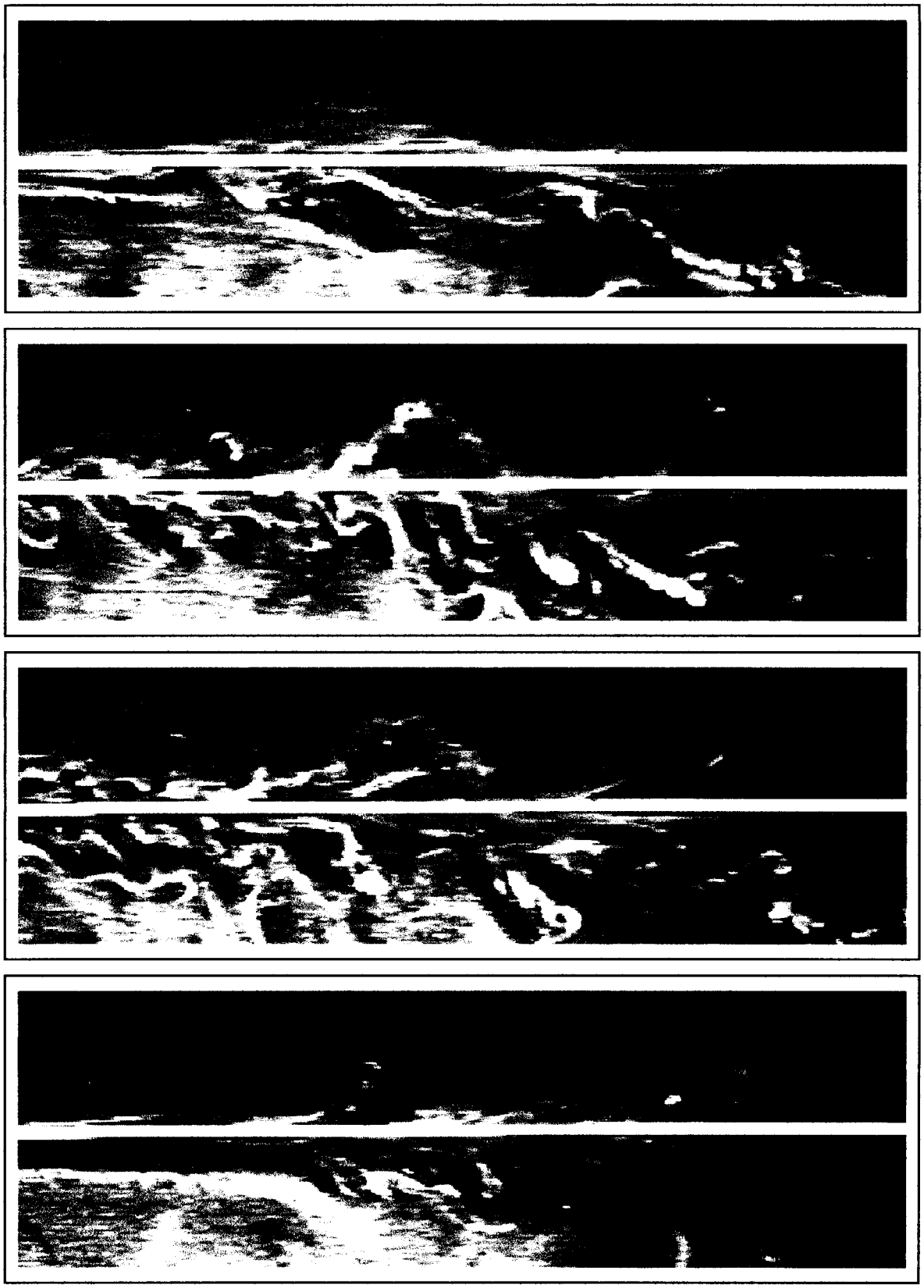

Figure 7.1 Visualisation of the axisymmetric turbulent boundary layer, hydrogen bubbles in water, $Re_a = 150$, a = 1.47 mm, $\delta/a \approx 41$, at different times, flow direction $\Rightarrow$.

$Re_a = 137$, $\delta/a \approx 42$

$Re_a = 170$, $\delta/a \approx 41$

$Re_a = 264$, $\delta/a \approx 39$

Figure 7.2 Visualisation of the axisymmetric turbulent boundary layer, hydrogen bubbles in water, various Re_a as indicated, a = 1.47 mm, flow direction ⇒.

The images of the structure of the axial flow thus provide some evidence of inner-layer low-speed fluid being carried outwards into the outer boundary layer, but give no indication as to the cause of these outward migrations.

The occasional appearance of vortices in the axial flow, coupled with the knowledge that regular vortex shedding occurs in near-axial flow at yaw angles as small as one degree, suggests that the outward flows may be the result of occasional turbulent crossflows originating on the opposite side of the cylinder (as envisaged by Luxton, Bull and Rajagopalan, 1984 and Lueptow and Haritonidis, 1987); these would not be visible because of their small deviation, possibly only one degree, from the free stream flow direction. It should be noted here that the structures shown up by flow visualisation in the axial-flow boundary layer represent the trajectories of the fluid that forms the vortices; these structures are inclined at about 45° to the downstream direction. In contrast, the visualised structures in the near-axial-flow case represent the rolled-up cores or axes of the vortices as seen in a plane at 90° to the plane of the "vortex street", and are inclined at about 45° to the upstream direction.

The results of simultaneous velocity measurement and flow visualisation by smoke generated at the cylinder surface, in an air-flow (Dekkers, Bull and Luxton, 1991, Appendix 7), are shown in Figure [7.3]. They were obtained using the experimental arrangement shown in Figure [3.7]. Both the oscilloscope trace from the velocity probe and the smoke particles in the axisymmetric boundary layer are shown in the video images. Examination of individual video frames clearly indicates that the smoke originating at the surface of the cylinder is ejected outwards at random intervals, and that when the velocity probe is within the marked fluid (the smoke) it detects a

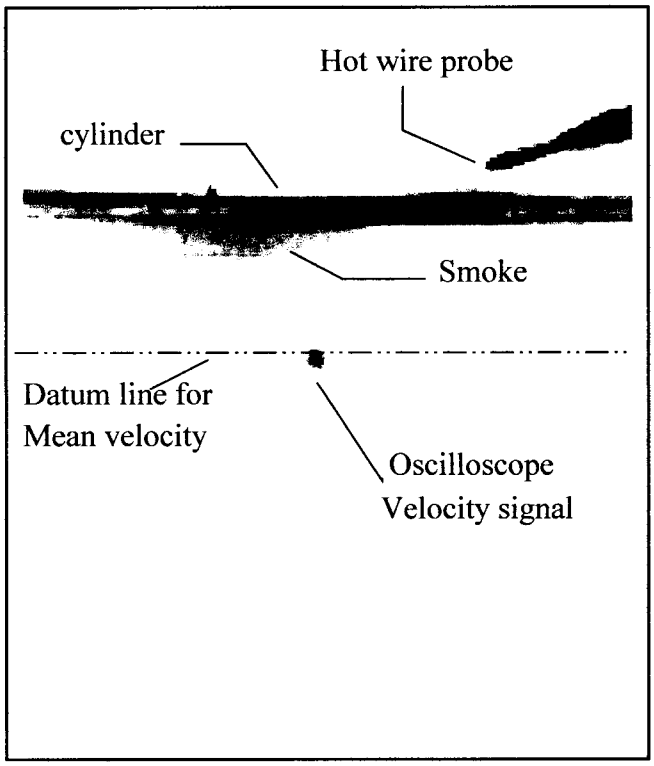

(a). Detection of mean velocity.

The hot wire probe is not immersed in the smoke generated upstream on the cylinder surface, and the velocity is indicated by the instantaneous oscilloscope trace appearing at the datum level for the mean flow velocity.

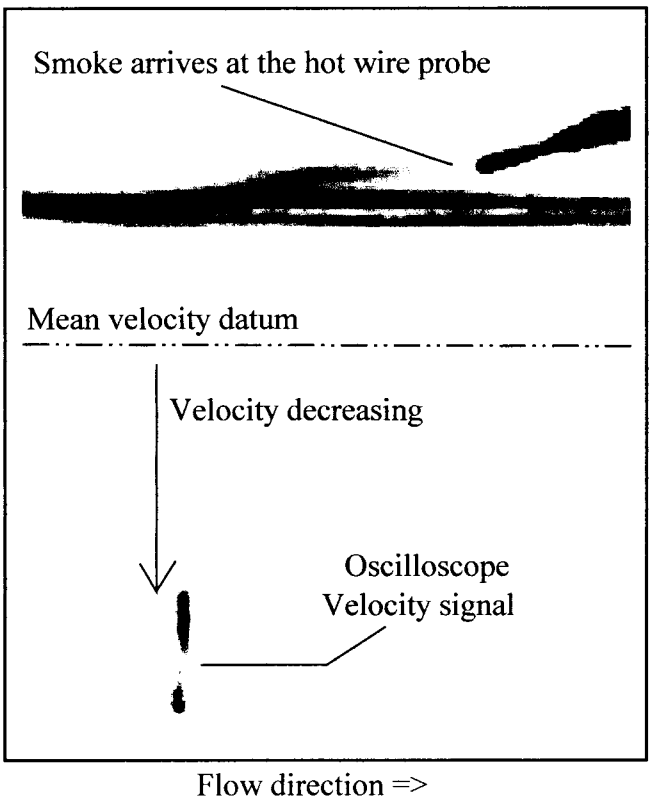

(b). Detection of a low speed spot.

The hot wire probe is immersed in the smoke generated upstream on the cylinder surface. The instantaneous oscilloscope trace appears below the datum level of the mean flow, indicating a drop in velocity below the mean value.

Figure 7.3 Simultaneous visualisation of the inner-layer fluid by smoke in air and detection of low-speed spots by hot wire anemometry, $Re_a = 375$, a = 1.47 mm, $\delta/a \approx 36$.

low-velocity spot, shown in Figure [7.3] as a drop in the oscilloscope trace. When the velocity probe is in the unmarked (no smoke) fluid it detects the mean boundary-layer velocity at that radial location.

These experiments confirm that the negative-velocity spikes in the fluctuating longitudinal-velocity signal are the result of inner-layer low-speed fluid being convected outwards into the outer boundary layer. This, in turn, provides evidence that the structures observed in the axial-flow hydrogen-bubble visualisations consist of low-speed fluid moving outwards.

There is no indication of the cause of the outward movement of the inner-layer fluid visible in the video images of the smoke shown in Figure [7.3], and, for the reasons already given for the water flow experiments, the suspected cause, turbulent cross flows, would be unlikely to be visible in these air-flow images. Further investigation of the low-speed spots in the outer boundary layer velocity is based on hot-wire anemometry.

7.2 Conditional Sampling of the Fluctuating Velocity

The low speed spots within the turbulence-velocity signal have been examined in detail by conditional sampling of the time series data for the fluctuating velocity in the axial flow over a cylinder with $\delta/a = 38$ at a Reynolds number $Re_a = 300$. Using the hot-wire anemometry equipment and procedures previously detailed in section [3.3], the fluctuating longitudinal velocity was digitally recorded as a mean voltage and a time series of the AC-coupled fluctuating voltage (amplified by a gain of 200, filtered at 10 kHz, and sampled at 20 kHz). These voltages were converted to a time series of the velocity U, using the calibration data for the particular hot wire probe used. Up to four probes could be operated simultaneously in this manner, with the total number of data points streamed to the computer hard disk in blocks of 32,000 points.

Conditional sampling relies on the comparison of each data point with a particular condition, and the extraction, for further examination, of segments of the time history where the condition is met. This technique can be applied to the investigation of low speed spots within the turbulence-velocity fluctuations by examining the velocity time-series for points where the instantaneous velocity is less than a particular chosen value, and extracting a segment of the data series around this point for analysis.

The conditioning level used to determine occurrence of a low-speed spot is expressed as a multiple of u′, the rms value of the velocity fluctuation about the mean velocity, where both the mean and rms values vary with radial position y within the

boundary layer, and with the boundary-layer Reynolds number Re_a. The first step in analysing the time-series data is thus to determine the mean value of the velocity, and the rms value of the fluctuating velocity component, and then to select a suitable conditioning level to define a low speed spot.

A typical time-history of fluctuations in streamwise velocity at a radial location 5 mm above the cylinder surface is shown in Figure [7.4] for a duration of 150 milliseconds (3000 data points). The mean velocity is shown as a dashed line, and different multiples of the rms velocity u′ are shown as dotted lines above and below the mean velocity.

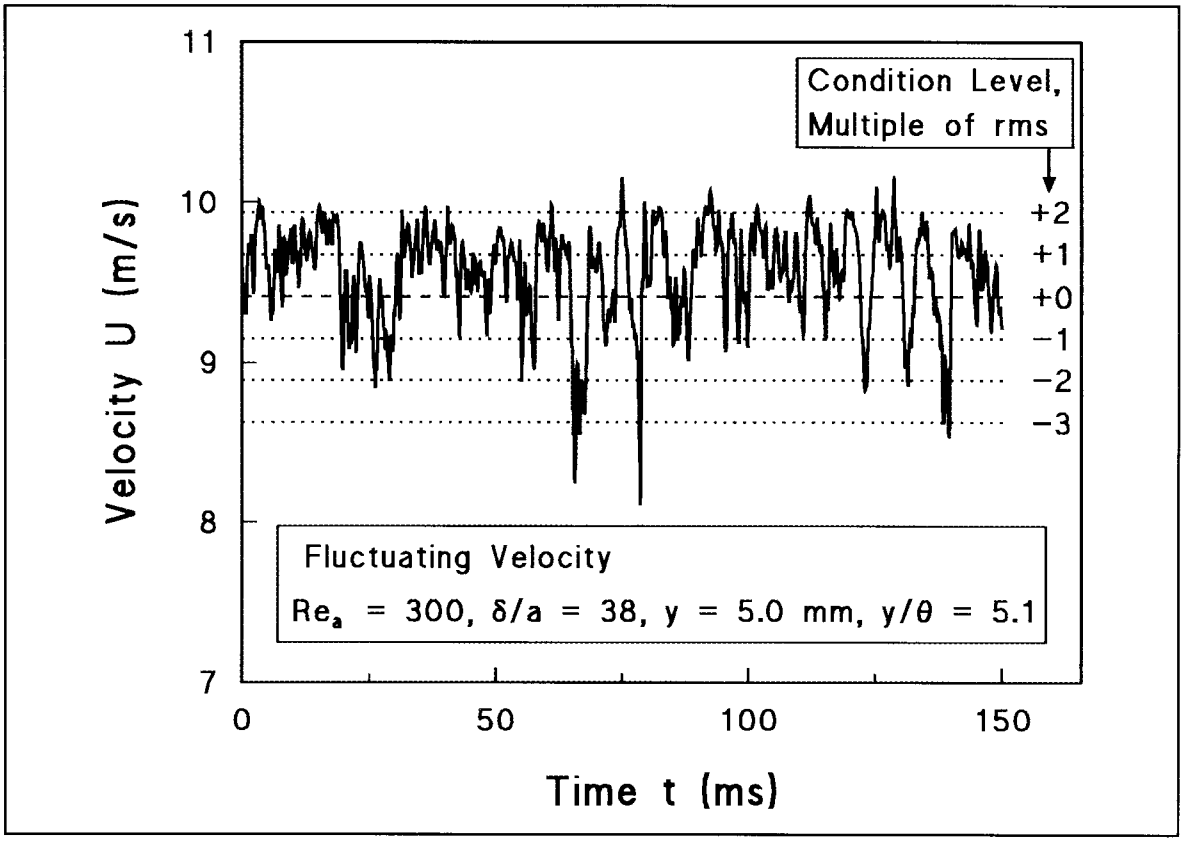

Figure 7.4 Longitudinal velocity fluctuation signal with different conditional sampling levels given as multiples of the rms value u′, for Re_a = 300, δ/a = 38, y/θ = 5.1.

From examination of records such as that shown in Figure [7.4], the (somewhat arbitrary) definition of a low speed spot has to be established - by selection of a characteristic threshold of (negative) velocity excursion from the mean velocity. The "normal" turbulent fluctuations, that is those which do not contribute significantly to the large negative skewness of the data, should not exceed the selected negative excursion, leaving only the main contributors, the larger negative spikes, as the low speed spots. It is found that, in general, the "normal" fluctuations, as in Figure [7.4], occur in the range $-1.5 < u/u' < +2.5$, with an unskewed mean of +0.5. The large negative spikes have minimum peaks of u/u' between -1.5 and -5, with very few larger that -3. It therefore appears appropriate to characterise low-speed spots by minimum peaks which are less than a value somewhat lower than -1.5. On this basis the criterion $u/u' < -2.0$ seems appropriate.

The effect of conditioning level on conditional sampling of the fluctuating velocity at different radial locations across the boundary layer has been investigated by using a digital computer algorithm that determines the mean and rms values of a given time-history record and then examines each data point relative to the conditioning level. A segment of the time history is then recorded as a "low-speed spot" whenever the velocity falls below the conditioning level. Data segments containing 2.5 milliseconds of data before and after each detection are used to ensure that the entire fluctuation is recorded.

The number of low speed spots detected, as a percentage of the velocity time history, is shown in Figure [7.5].

The figure indicates that it is reasonable to adopt u/u′ < -2.0 as a common definition of a low-speed spot across the whole of the boundary layer. The sensitivity of particular analysis procedures to the selected conditioning level will be examined in the subsequent sections where these procedures are used.

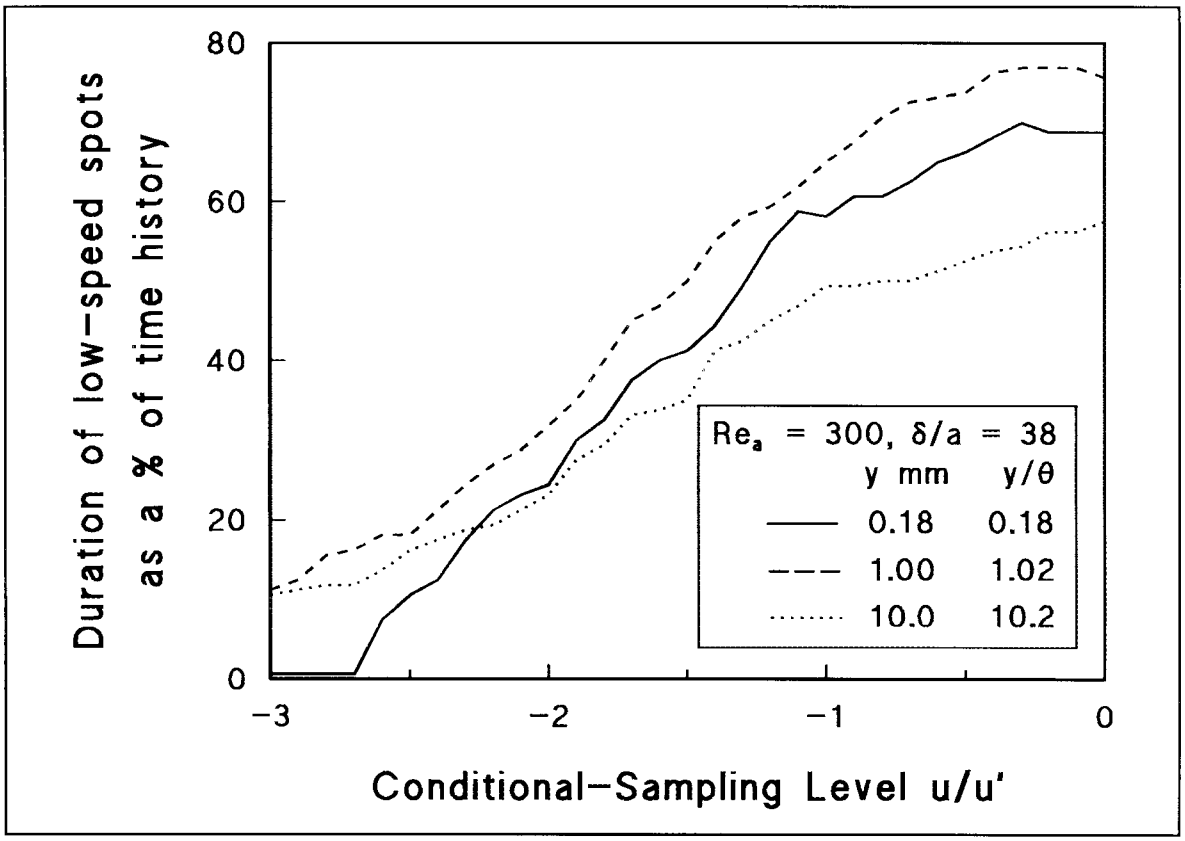

Figure 7.5 The effect of varying conditional sampling detection level, as a multiple of the rms value u′, at radial locations y/θ = 0.18, 1.02, 10.2, with Re_a = 300, δ/a = 38.

7.3 Ensemble Averages of the Low-speed Spots

The ensemble-average streamwise velocity $\langle u(t) \rangle$ at time t (measured relative to the detection time) is given by

$$\langle u(t) \rangle = \frac{1}{N} \sum_{k=1}^{N} {}^{k}u(t), \qquad [7.1]$$

where ${}^{k}u(t)$ is the velocity at time t in the time record of the k_{th} low speed spot detected. The distribution of ${}^{k}u(t)$ over t defines the k_{th} low speed spot detected, and the distribution of $\langle u(t) \rangle$ defines the ensemble-average low-speed spot. The number of detected low-speed spots N used to form the ensemble average will be referred to as the ensemble size. (The number of data points in the record from which the low-speed spots are identified will be referred to as the sample size. The ensemble size N is in general in the order of about 1/400 of the sample size.)

Ensemble averages of the low speed spots detected in the time-histories of the flustuating streamwise velocity by conditional sampling are shown in Figure [7.6], where times are measured relative to the detection time (that is the time at which the falling velocity equals the conditioning value). The figure shows the results of measurements with a single hot wire probe located at y = 1 mm and y = 10 mm and the effect of setting the conditional-sampling detection level to different values at these locations. The same ensemble averages are shown in Figure [7.7] with the velocity variation from the mean normalised by the local rms velocity fluctuation. Both figures show that the shape of the velocity trace associated with an average low speed spot does not vary greatly over this range of detection level.

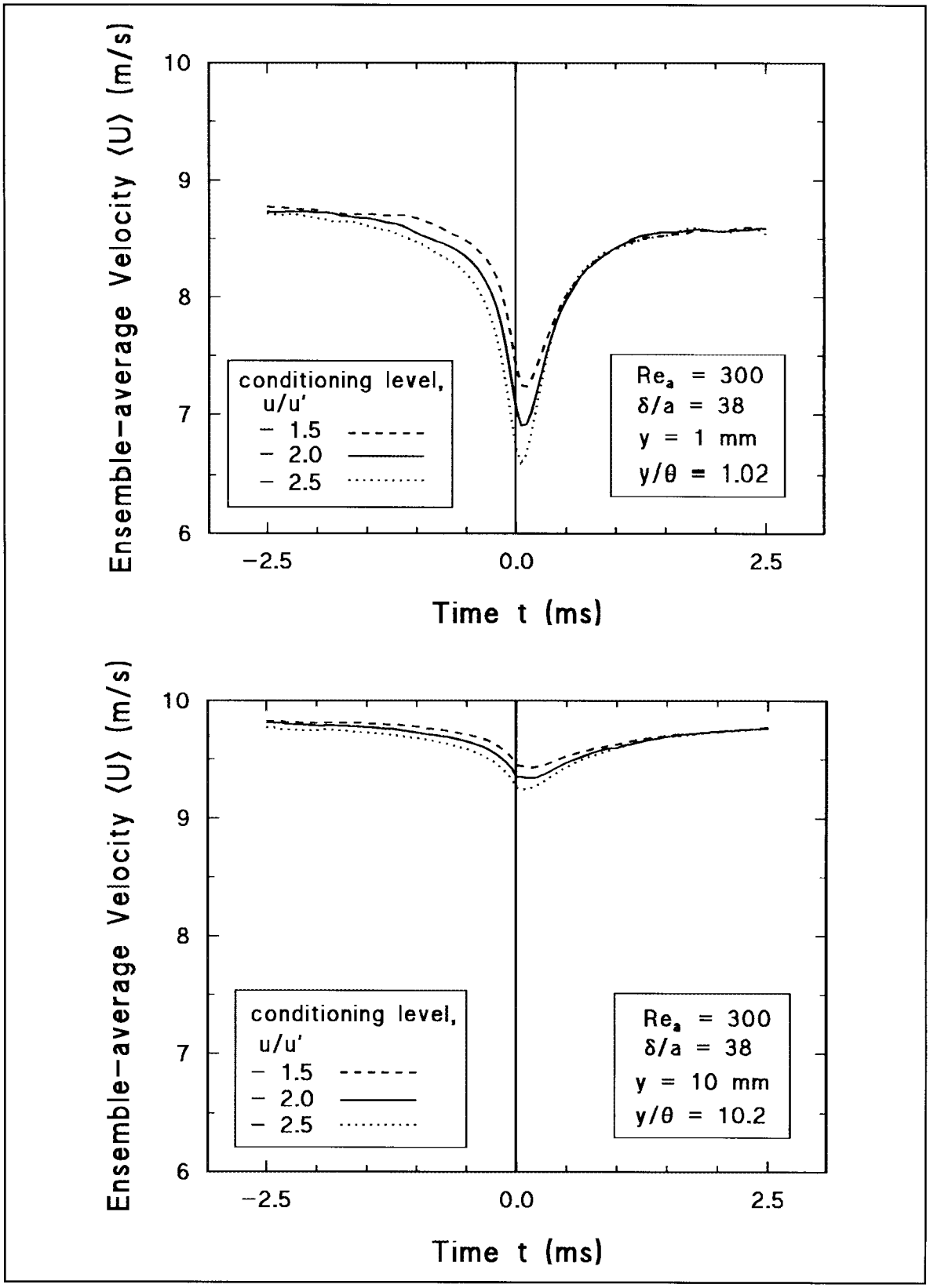

Figure 7.6 Ensemble averages of low speed spots ⟨U⟩ for different conditional-sampling detection levels. Re_a =300, δ/a =38, y/θ =1.02 (upper), y/θ =10.2 (lower).

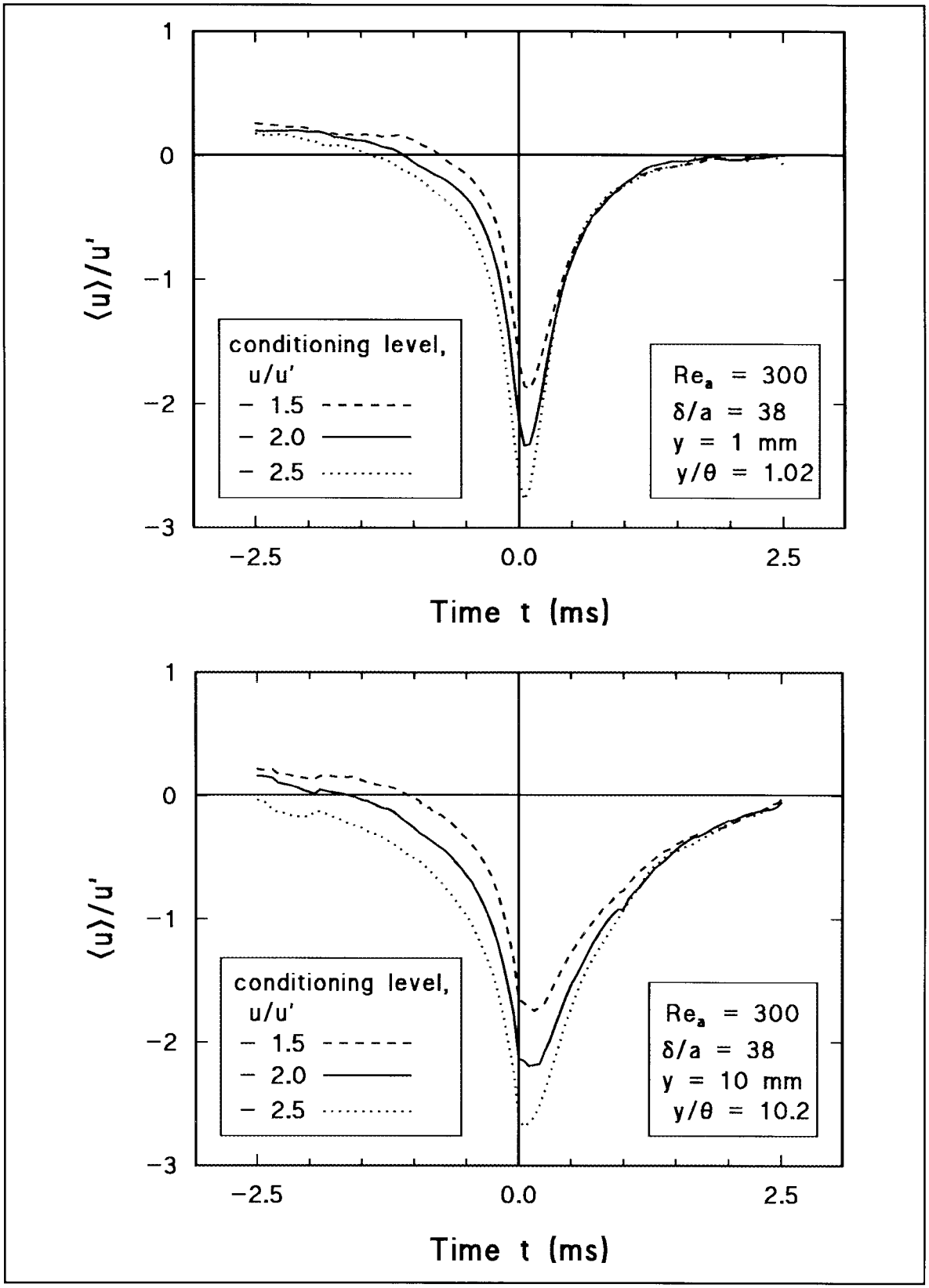

Figure 7.7 Ensemble averages of low speed spots ⟨u⟩/u′ for different conditional-sampling detection levels. Re_a =300, δ/a =38, y/θ =1.02 (upper), y/θ =10.2 (lower).

The effects of variation in radial location on the low speed spot, in the normalised form of the ensemble average ($\langle u \rangle / u'$), with a given detection level of $u/u' = -2.0$ are shown in Figure [7.8]. The algorithm used to generate the ensemble averages ensures that all the velocity traces pass through the point $\langle u \rangle / u' = -2$ at time $t = 0$, and the effect of radial location is shown by the different rates of divergence of the ensemble averages from this point.

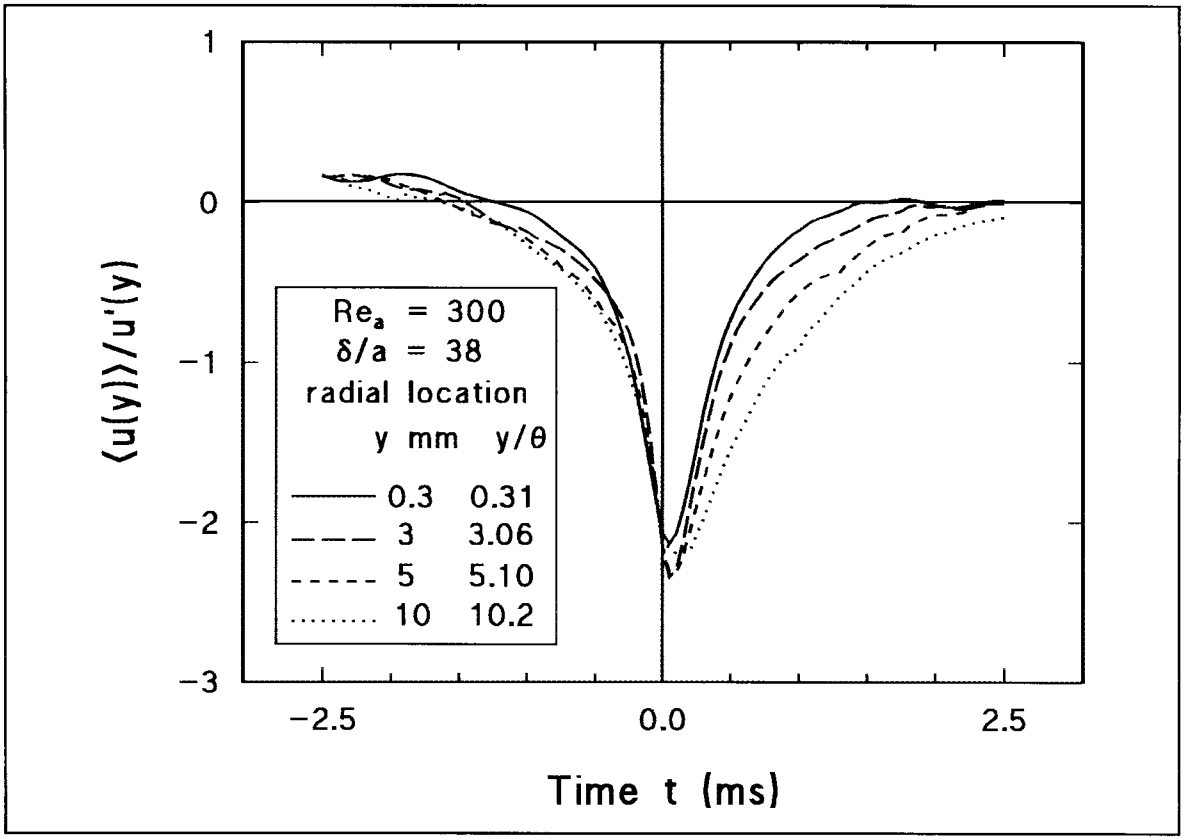

Figure 7.8 Ensemble averages of low speed spots at different radial locations y. Conditional sampling level $u/u' = -2$, sample sizes = 160,000 points, $Re_a = 300$, $\delta/a = 38$.

The main change in the characteristic shape of the ensemble-averaged low-velocity spot with radial location is a progressive increase in the duration of the lowered velocity with increasing distance from the cylinder surface. It may be expected that initially coherent features in a fluid flow, such as a region of low velocity, will become less clearly defined as time progresses. Consequently the decrease in "sharpness" of the ensemble averages with increasing radial distance may indicate an increase in age of the low-speed spots, those in the outer layer being older and more completely merged with the background turbulence. This would be consistent with the low-velocity spots being formed in the inner part of the boundary layer as very clearly defined regions of low velocity and progressively diffusing into the background turbulence as they move outwards in the boundary layer.

In order to obtain consistent results for the shape of the ensemble-averaged low-velocity spots, at a given radial location and Reynolds number, it is necessary to use an ensemble of low-speed-spot records of sufficiently large size to ensure that random variations within individual records do not affect the final average. The effect of ensemble size N on the smoothness of the resulting ensemble averages is shown in Figure [7.9] for an order of magnitude variation in N. The particular values of the sample sizes used are restricted to multiples of 16,000 by the analogue-to-digital data acquisition hardware.

Localised small-scale features of the ensemble averages shown in Figure [7.9] disappear as the ensemble size is increased, suggesting that these features are a product of small ensemble size and are not genuine characteristics of the average curve. These examples indicate that a minimum of 400 low-speed-spot records (with a sample size $\geq$

160,000 data points) should be used for each ensemble average at a particular location and Reynolds number. Because of greater statistical variation between individual segments of the velocity time-series from the secondary than from the primary probe, it may also be expected that yet larger ensemble sizes will be required for simultaneously-recorded velocity signals obtained from secondary hot wire probes.

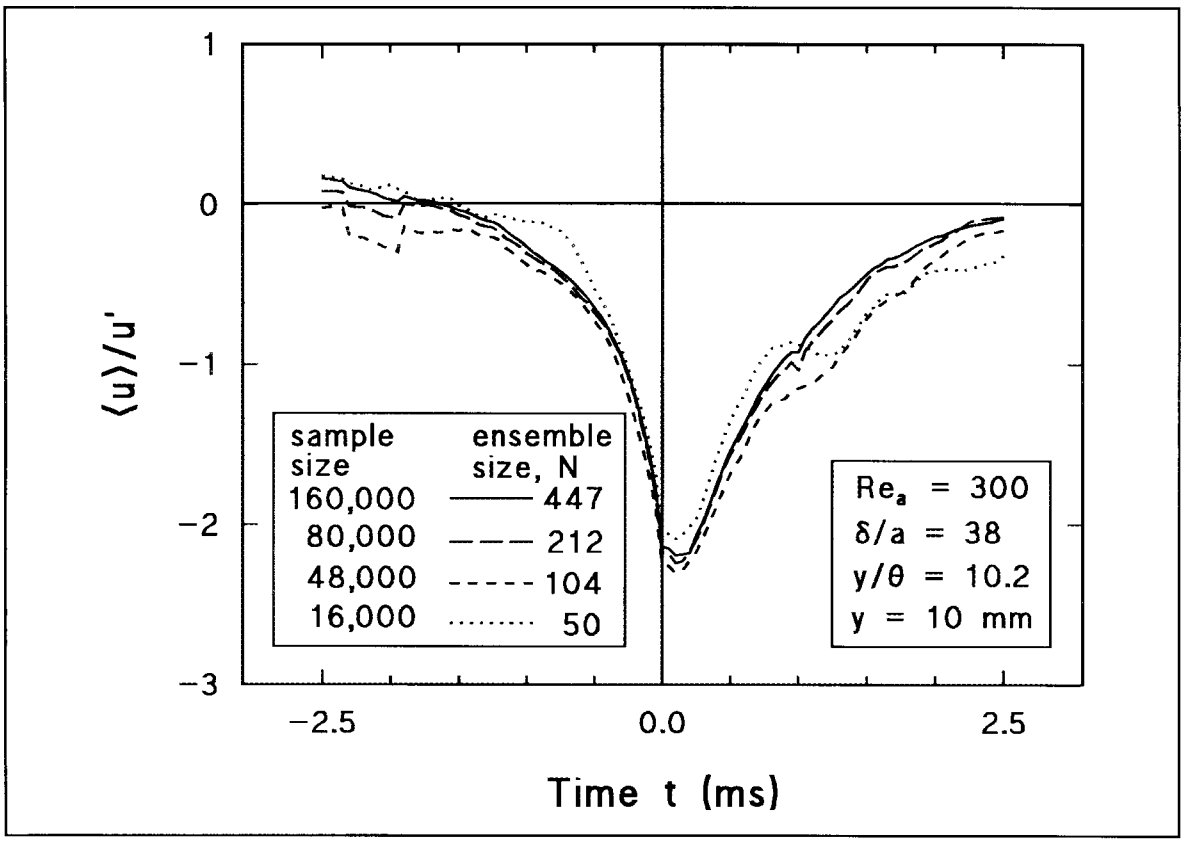

Figure 7.9 Ensemble averages of low speed spots for different ensemble sizes. Conditional sampling level u/u′ = -2, Re_a = 300, δ/a = 38, y/θ = 10.2.

7.4 Detection of Fronts of Low-speed Fluid

The extent of the region of low velocity, the streamwise signature of which has been detected by a single hot wire probe, can be explored by simultaneously recording the velocity signal at a second (and third etc.) point. An ensemble-averaged time-history of velocity at the second point, for the same set of time segments as those determining the ensemble-averaged low-speed spot from the detection-probe signal, can then be obtained. This second (and third etc.) ensemble average indicates the average behaviour of the velocity at the second location at the time of occurrence of a low-speed spot at the first probe position. Thus by using an array of hot wire probes, or by repeated measurements for different secondary-probe locations, the extent of the low-velocity region can be determined.

With the available hot wire anemometer, four hot-wires - a primary probe and three secondary probes - could be used. However, initial experiments with multiple probes (each with a body diameter of 3 mm) indicated that the ideal separation between the probes was smaller than that which could easily be obtained by a simple array of four probes. The experiments were therefore confined to two probes, each positioned independently using the mechanism shown in Figure [3.8], and the probes were always located in the same radial plane.

As the velocity signals from both hot-wire probes are recorded in full, and the conditional sampling performed on the recorded data, there is really no distinction between a primary and a secondary probe: either signal may be conditionally sampled

to obtain the primary detection of a low-speed spot.

To minimise interference to the flow in the measurement region, and to allow very small separations between the two probes, right angled probes (Figure [3.9b]) were arranged as shown in Figure [7.10]. The hot-wires were located in the same radial plane at radial distances of y_1 and y_2, giving a radial separation of $\Delta y = (y_2-y_1)$, and separated by an axial distance of Δx, as shown in Figure [7.10]. The axial distances x_1 and x_2 are measured (downstream) from a position 2700 mm downstream of the start of the test section (the upstream end of the cylinder is, as in chapters four and five, located at the start of the test section).

The effect on ensemble averages of varying the sample size (and consequently the ensemble size) is shown in Figure [7.11]. As shown previously, the ensemble average of signal records from the primary probe (to which the sampling condition is applied) appears to become independent of the sample size at 160,000 data points (typically $N > 400$). However, the ensemble average of signals from the secondary probe, also shown in Figure [7.11], still indicates some variability at that sample size, and requires a sample in the order of 320,000 data points (typically $N > 800$) to smooth out the irregularities in any individual record.

Particular attention is paid here to the variation with ensemble size of the time delay between the minimum velocity detected by the primary probe and that observed in the ensemble average obtained from the secondary probe. Subsequent ensemble averages have therefore been obtained from samples with 320,000 data points ($N > 800$) from each probe, unless noted otherwise.

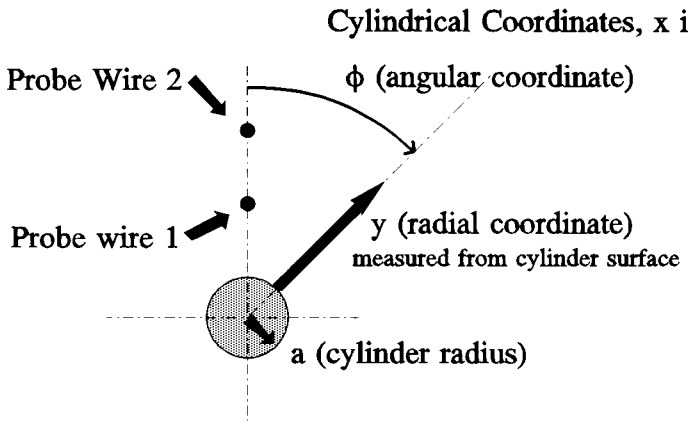

End View of Hot-wire Probe locations.

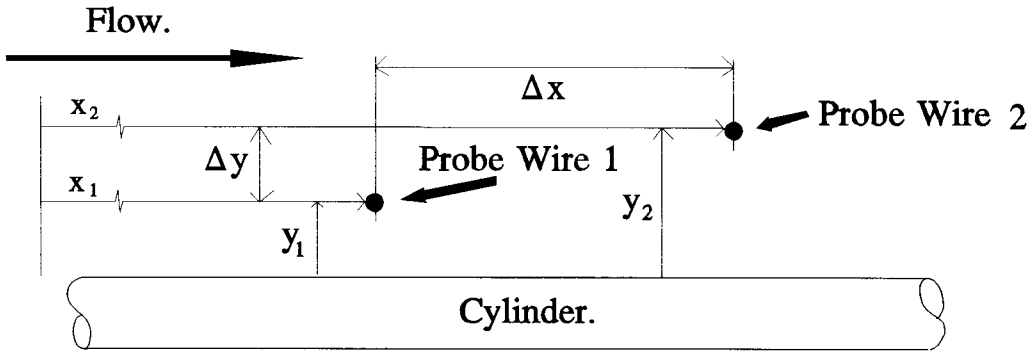

Side Elevation of Hot-wire Probe locations.

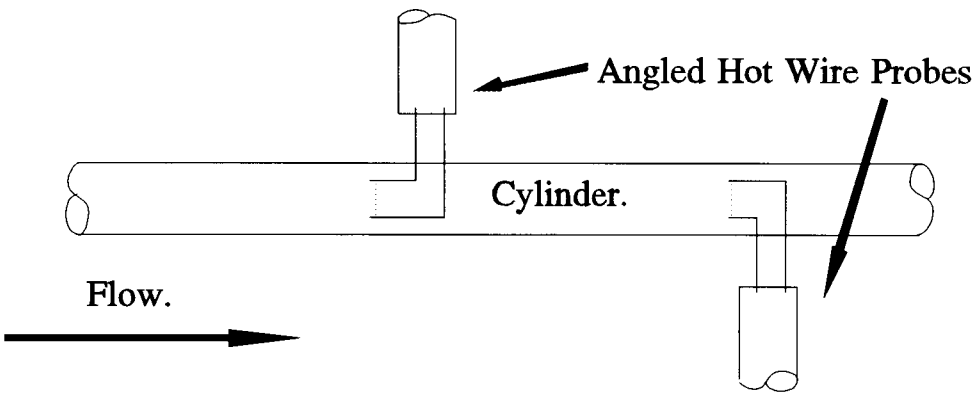

Plan View of Hot-wire Probe Arrangement.

Figure 7.10 Arrangement of hot-wire probes used to determine the region of low speed fluid, on one side of the cylinder only, (cylindrical coordinates defined in End View).

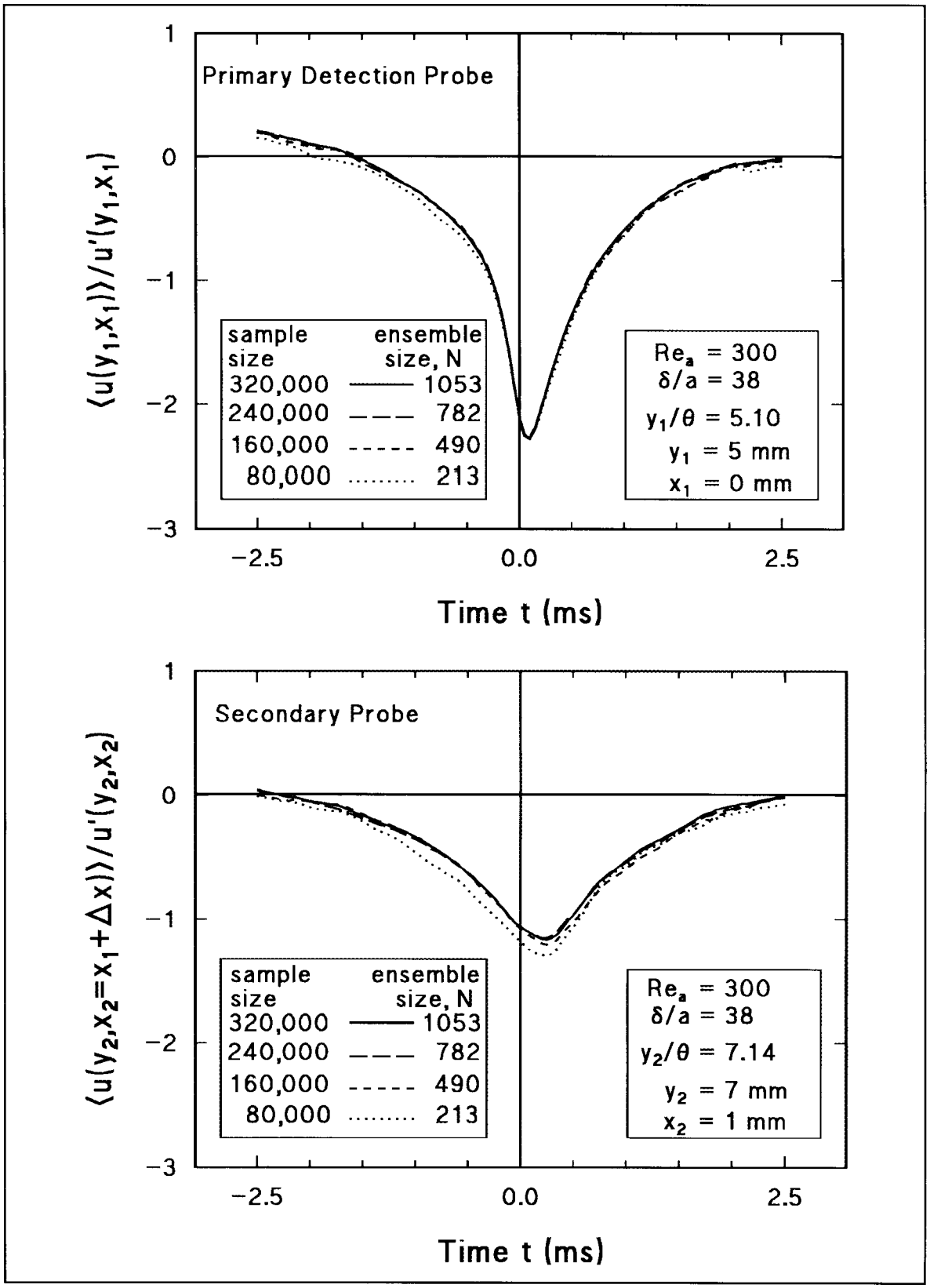

Figure 7.11 Ensemble averages of low speed spots for different ensemble sizes, for two probes with conditional sampling on the inner probe, ($\Delta x = (x_2 - x_1) = 1$ mm, $y_1/\theta = 5.10$, $y_2/\theta = 7.14$).

In generating simultaneous ensemble-averages from the two hot wire signals, conditional sampling may be applied to either one of the signals. The two possible results are shown in Figure [7.12] for hot-wires at $y_1 = 5$ mm and $y_2 = 7$ mm with $\Delta x = 1$ mm, for conditioning on the inner wire (upper graph), and on the outer wire (lower graph). As shown previously, there is little change, a very small decrease, in the magnitude of the low velocity peak with increase in radial location from y = 5 mm to y = 7 mm. In contrast, the magnitude of the low-velocity peak obtained from the secondary probe is significantly lower when the inner (y = 5 mm) probe is used for primary detection of low-speed spots than when the outer (y = 7 mm) probe is used as the primary detector. This suggests that a greater accuracy in determining the time delay between the two ensemble-average peaks may be obtained by treating the outer probe as the primary detector.

The region of low speed fluid may be mapped by detecting low-speed spots at one fixed probe and simultaneously measuring the corresponding velocity variation at a second probe for a range of radial-separation distances Δy between the probes. The results for a fixed probe at $y_1 = 5$ mm are shown in Figure [7.13] for radial separations of $\Delta y = \pm$ (1, 2 and 3) mm, and $\Delta x = 1$ mm. There is a rapid decrease in the coherence of the low-speed spot observed at the secondary probe with increasing radial separation Δy. The decrease is so rapid that the whole boundary layer thickness could not be accurately mapped with reference to a single fixed detector probe: a series of relative measurements is required between sets of points spanning the boundary layer. The difference in strengths of the velocity peaks at the secondary probe for detection on the outer and inner probes is again apparent for each pair of equal values of $|\Delta y|$ above and below the fixed detector probe at $y_1 = 5$ mm.

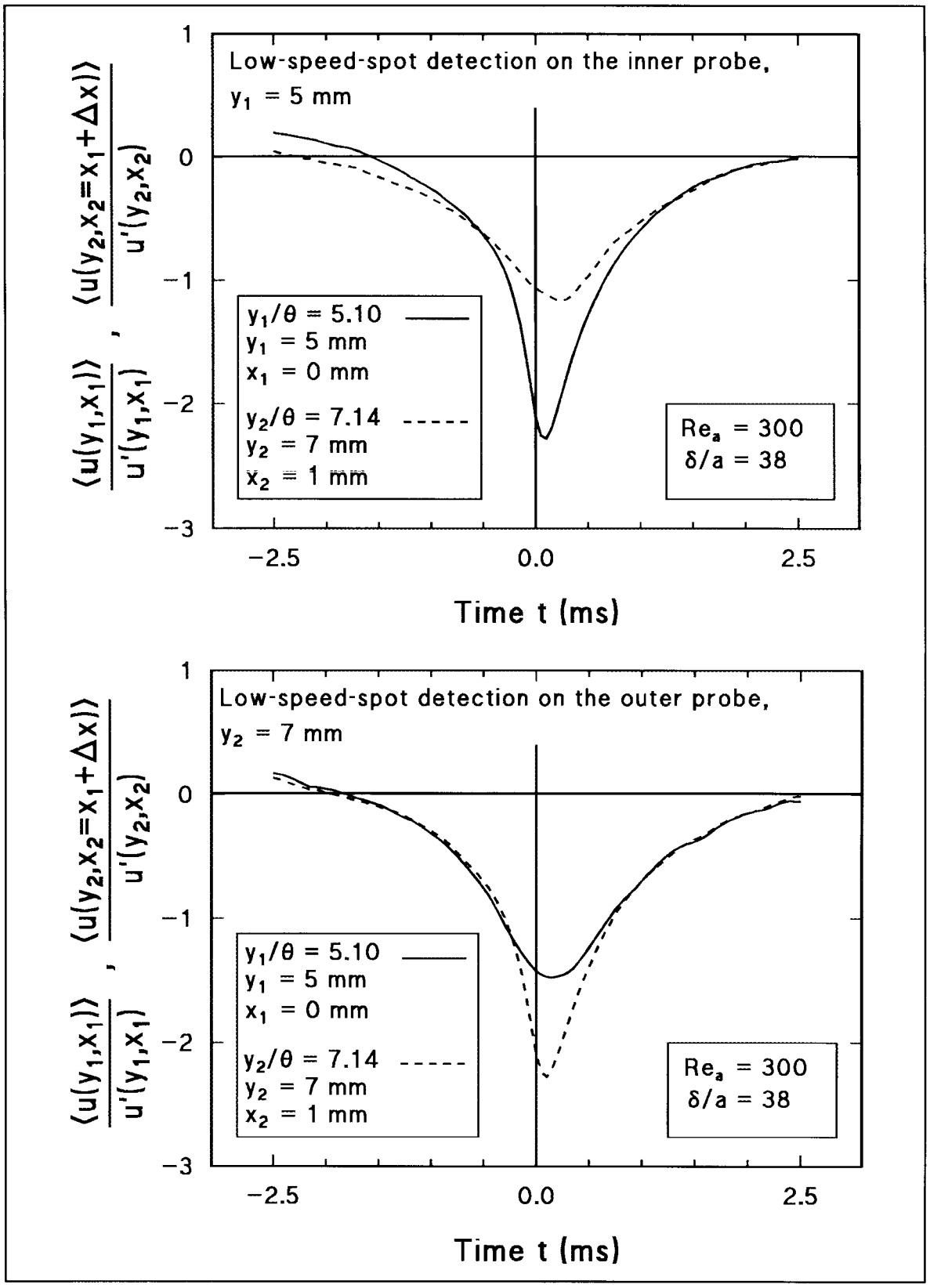

Figure 7.12 Ensemble averages of low-speed spots for two probes with conditional sampling on one or other probe. Sample size = 320,000, Ensemble size N > 800, Δx = 1 mm, y_1/θ = 5.10, y_2/θ = 7.14.

The time delay between the detection of a low-speed spot at one probe and the observation of a low-speed peak at the second probe is shown in Figure [7.13] for a single value of Δx and various Δy. Similar results have been obtained for a range of axial displacements Δx for each set of radial locations; a typical set of resulting ensemble averages, with $y_1 = 7$ and $y_2 = 5$ mm, for $\Delta x = 0$, 1, 2, 3 and 4 mm, is shown in Figure [7.14].

The time delay between low velocity peaks at the secondary probe and the primary detector probe Δt has been measured for each data set (of the type shown in Figure [7.14]). Plots of Δt against the axial displacement Δx, for a series of data sets, are shown in Figure [7.15 a,b,c], for various positions across the boundary layer.

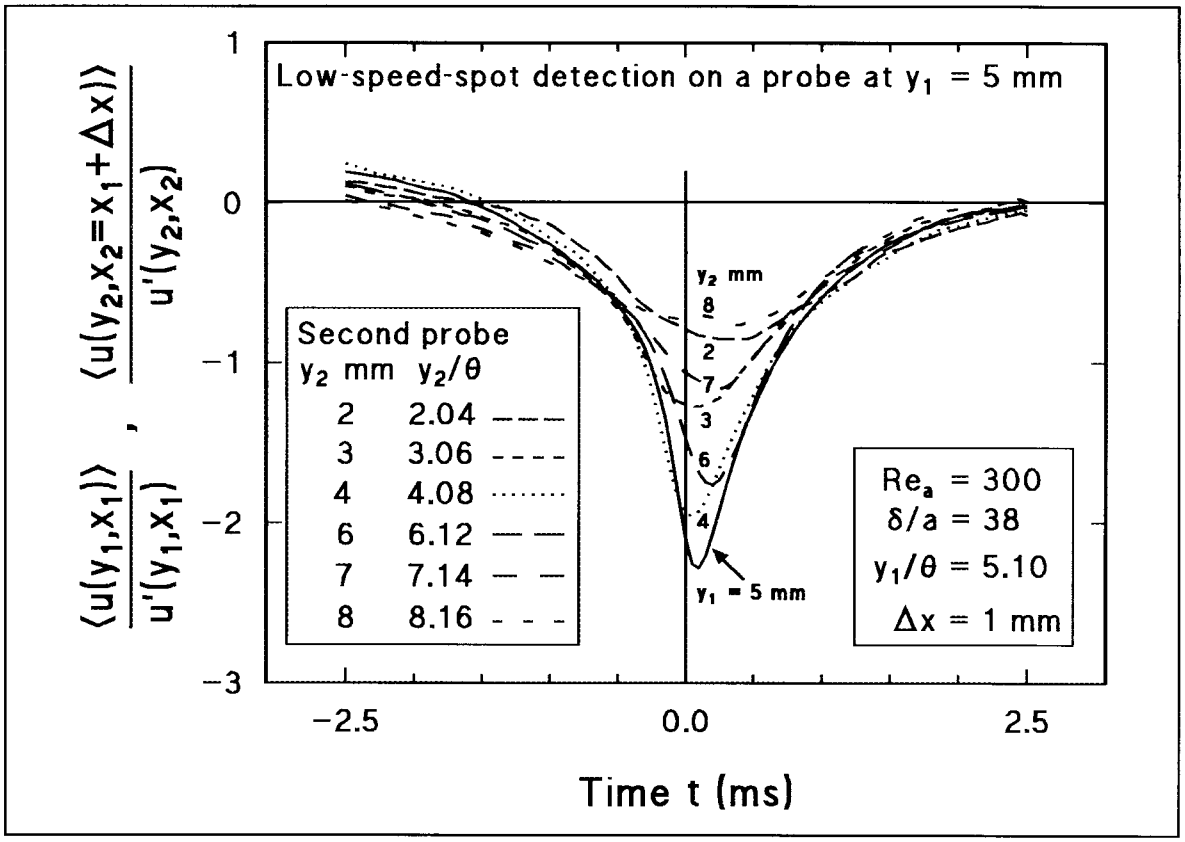

Figure 7.13 Ensemble averages of low speed spots for two probes with conditional sampling on a probe at $y_1/\theta = 5.10$, for various radial locations of the second probe y_2.

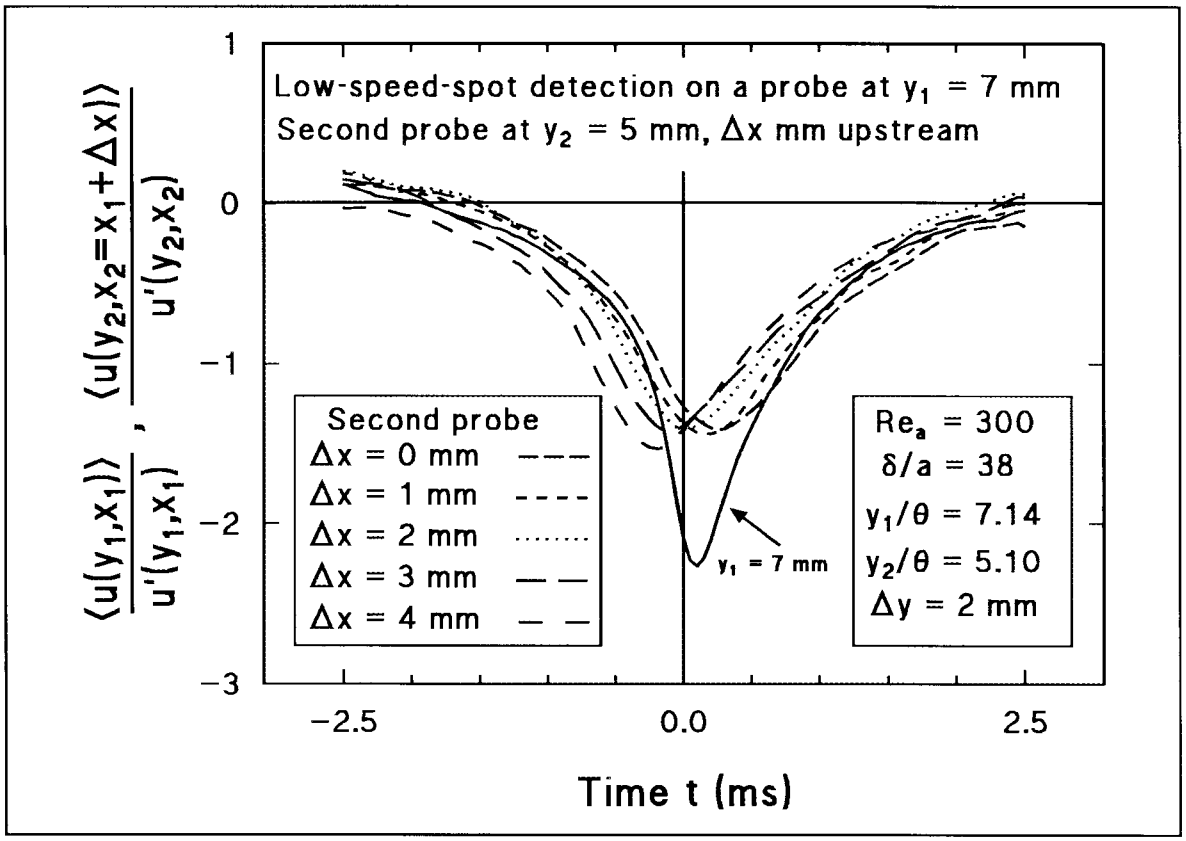

Figure 7.14 Ensemble averages of low speed spots for two probes with conditional sampling on a probe at y_1/θ = 7.14, for various axial locations Δx of the second probe.

A linear regression line, calculated for each set of time-delay data and shown in Figure [7.15 a,b,c], allows the axial displacement for zero time-delay between the two radial positions to be determined for each data set. The y_1 and y_2 combinations and the Δx values for Δt = 0 obtained from Figures [7.15 a,b,c] allow the centre line of low-velocity spots occurring simultaneously at various radial locations to be constructed. It is obtained as radial location y as a function of (relative) axial distance x, and shown in Figure [7.16]. An equation in the form $y = kx^n$ (with k = 0.175 and n = 1.75) fitted to the data is shown as a dotted line. This line can be interpreted as the centre line of a continuous front of low speed fluid (Bull and Luxton, 1991; Bull and Dekkers, 1993b, Appendix 5), extending across the boundary layer.

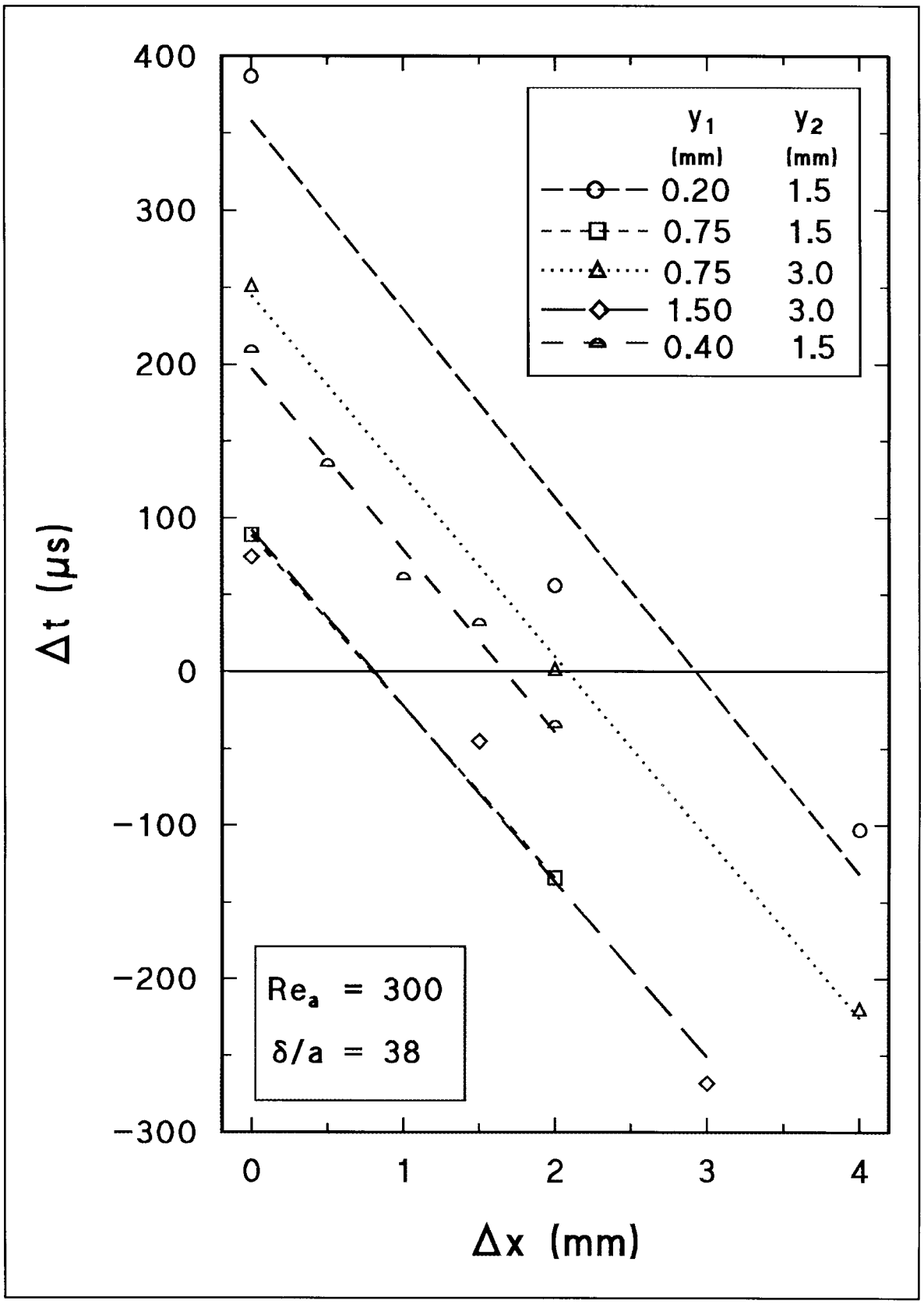

Figure 7.15(a) Determination of the axial distance Δx for simultaneous occurrence of low-speed spots at two probes Δy apart, for various radial probe-locations y_1 and y_2.

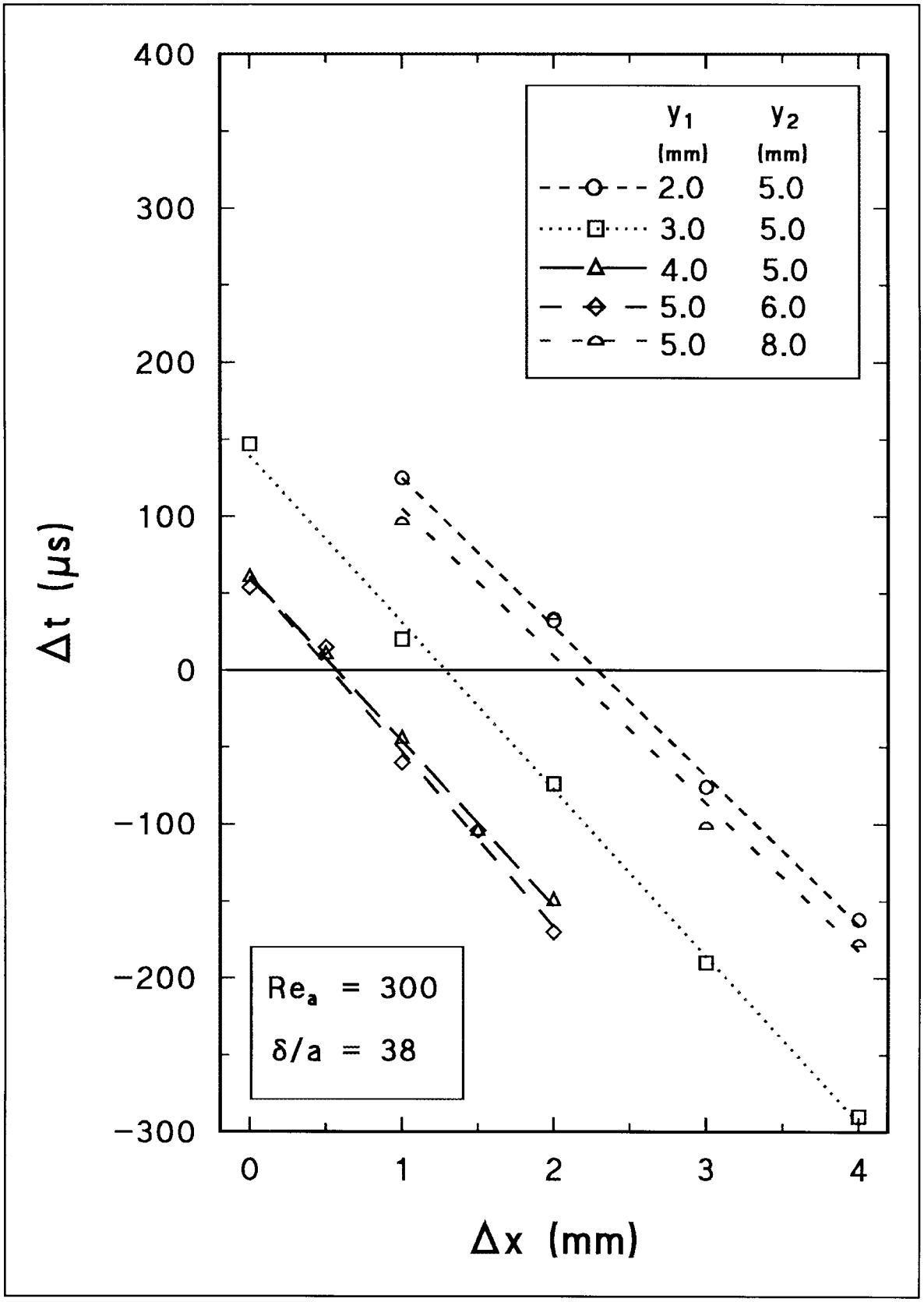

Figure 7.15(b) Determination of the axial distance Δx for simultaneous orrurrence of low-speed spots at two probes Δy apart, for various radial probe-locations y_1 and y_2.

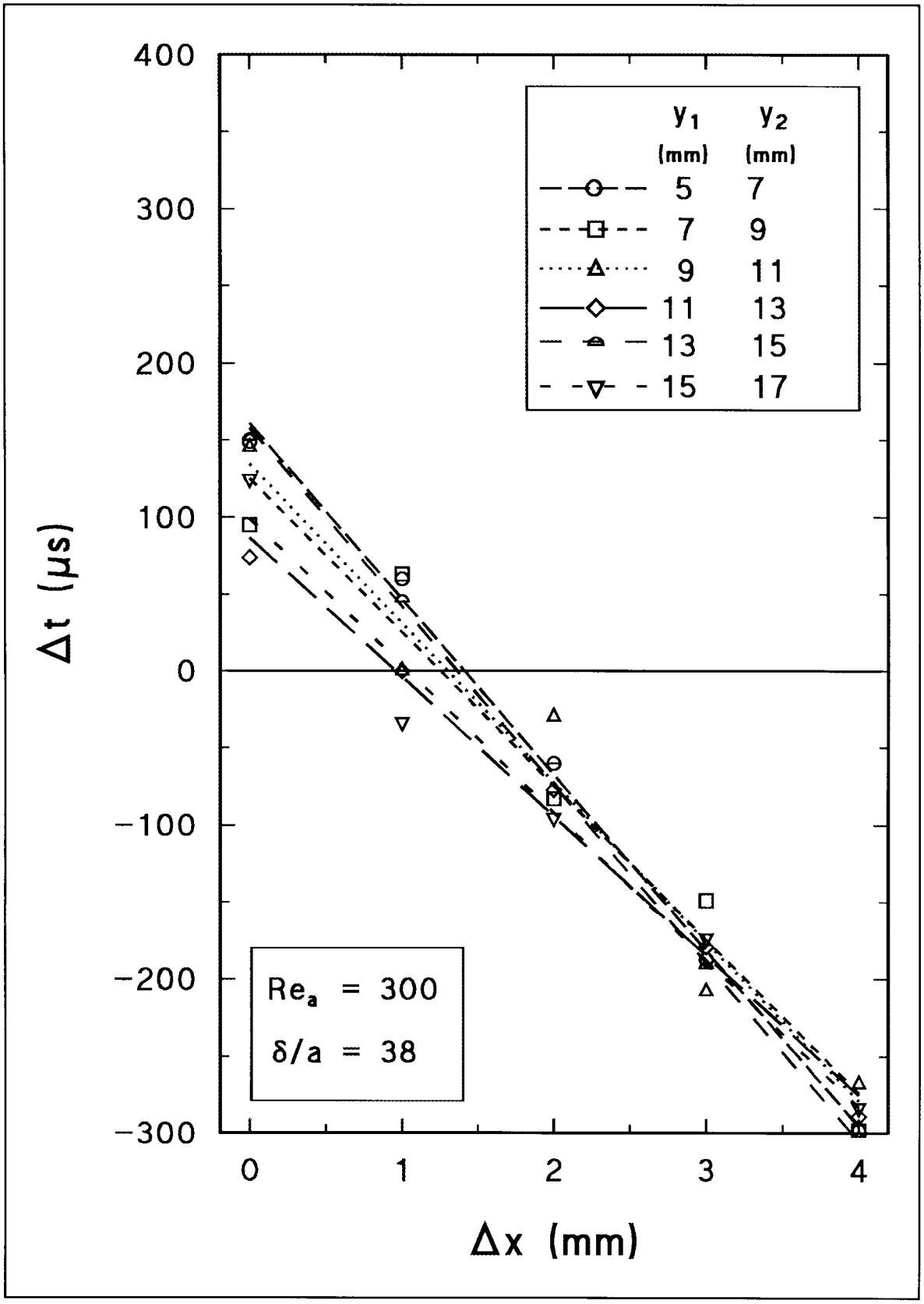

Figure 7.15(c) Determination of the axial distance Δx for simultaneous occurrence of low-speed spots at two probes Δy apart, for various radial probe locations y_1 and y_2.

A representative axial width of the low-speed region can be calculated at each y_1 measurement position from the time for which the ensemble-average velocity is below the conditional-sampling level (that is, less than 2u′ below the mean value), multiplied by the local mean velocity. This width is shown in Figure [7.16] as a bar in the x direction.

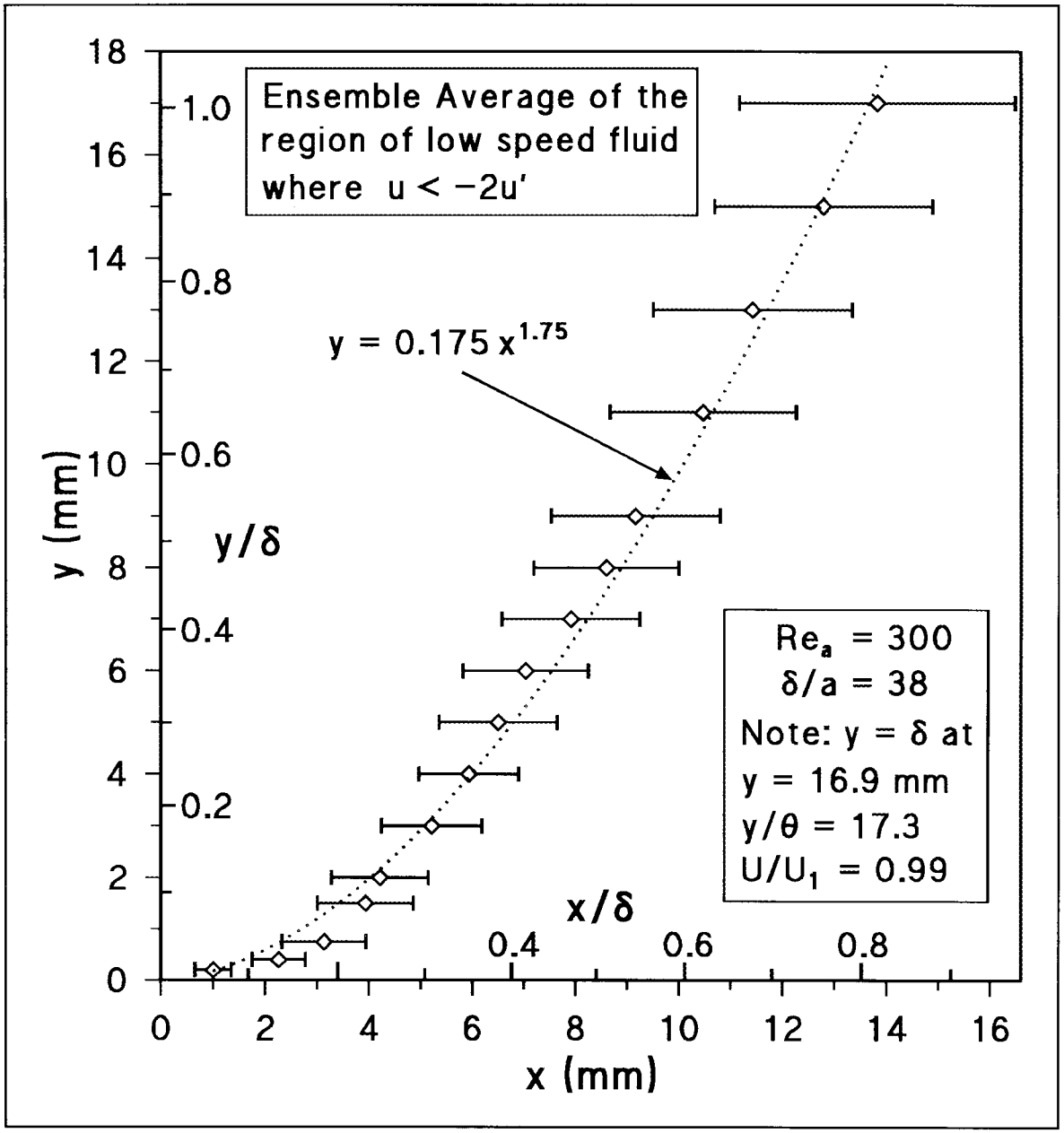

Figure 7.16 Locus of the "front" of low-speed fluid across the boundary layer, determined from ensemble averages of the fluctuating longitudinal velocity of low-speed spots.

The resulting image of a two dimensional slice in a plane through the axis of symmetry of the boundary layer, shown for one side of the cylinder only in Figure [7.16], indicates a region of low-speed fluid extending outwards from the cylinder surface and angled downstream, which is gradually diffusing into the background turbulence with increasing radial distance from the cylinder surface. This averaged image of the low speed region appears to be similar to the structures observed in individual coherent events in the flow visualisation of the boundary layer in Figures [7.1 and 7.2]. The geometry of the low-speed region determined here strongly suggests advection of low-speed inner-layer fluid from the cylinder surface into the outer boundary-layer.

Further evidence for the outward movement of low-speed fluid is provided by measurements of the longitudinal and radial velocity fluctuations, using a hot-wire probe with cross-wires, at various radial positions across the boundary layer. Ensemble averages $\langle v(y,t) \rangle$ of the radial (v) velocity component associated with the longitudinal (u) velocity, characterising low-speed spots shown in Figure [7.17], clearly indicate a positive (outward) radial flow associated with the low-speed spots.

The form of the flow structure is shown diagrammatically in Figure [7.18] as a region of low-speed fluid, formed by fluid moving outwards from the cylinder at a small angle (shown larger for clarity) extending across the boundary layer. The angle can be estimated from the relative magnitudes of the ensemble averages of the radial- and axial-velocity components within the low speed region. As an example, consider flow with $Re_a = 300$ ($U_1 = 10.35$ m/s) at $y = 10$ mm ($y/\theta = 10.2$) where $U/U_1 = 0.965$ (Figure 4.3); $u'/U_1 = 0.025$ (Figure 4.9); $\langle u \rangle/u' = -2$ and

$\langle v\rangle/v' = +0.75$ (average values within the low-u, high-v region, Figure 7.17); and $v' = 0.135$ m/s. The average axial-velocity component of the low-speed fluid is given by $U = U_1(U/U_1 + \langle u\rangle/u' \cdot u'/U_1) = 10.35(0.965 - 2\times0.025) = 9.47$ m/s, and the average radial-velocity component $v = \langle v\rangle/v' \cdot v' = 0.75\times0.135 = 0.10$ m/s. Thus the velocity of the fluid in the low-speed front is inclined outwards from the cylinder axis at an angle of 0.6° ($\tan^{-1}0.1/9.47$) at $y/\delta \simeq 0.59$. As the magnitude of this angle will vary along the front, the trajectories of the low-speed fluid leading to the formation of the front are not necessarily straight lines.

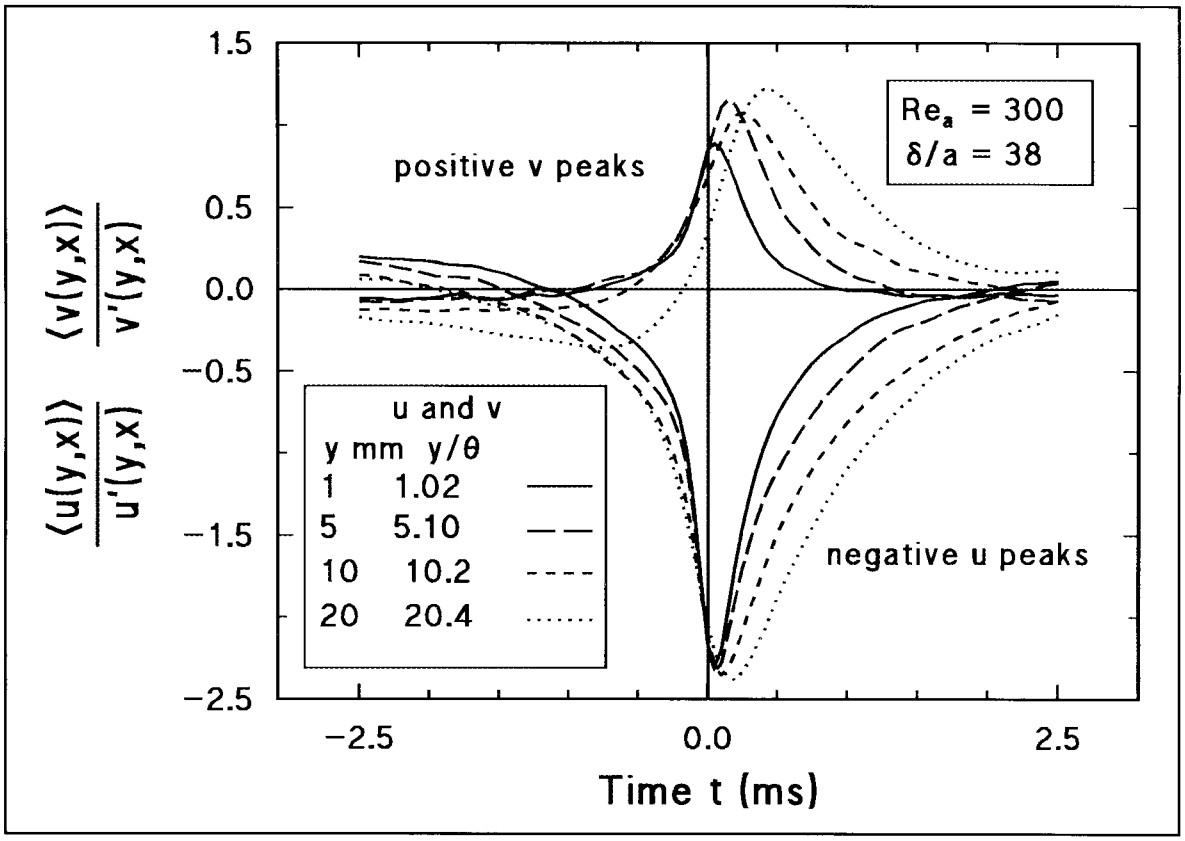

Figure 7.17 Ensemble averages of the longitudinal (u) and radial (v) velocity fluctuations at radial locations $y/\theta = 1.02, 5.10, 10.2, 20.4$, conditionally sampled on u-component $2u'$ below the mean velocity (60 second data samples, N> 3,000).

The preceding results provide strong evidence that fronts of low-speed fluid moving outwards from the cylinder surface are a distinctive feature of the structure of the turbulence generated within the thick axisymmetric boundary layer. Investigation of the inner-layer flow processes associated with the formation of the low-speed fronts is the subject of the next section.

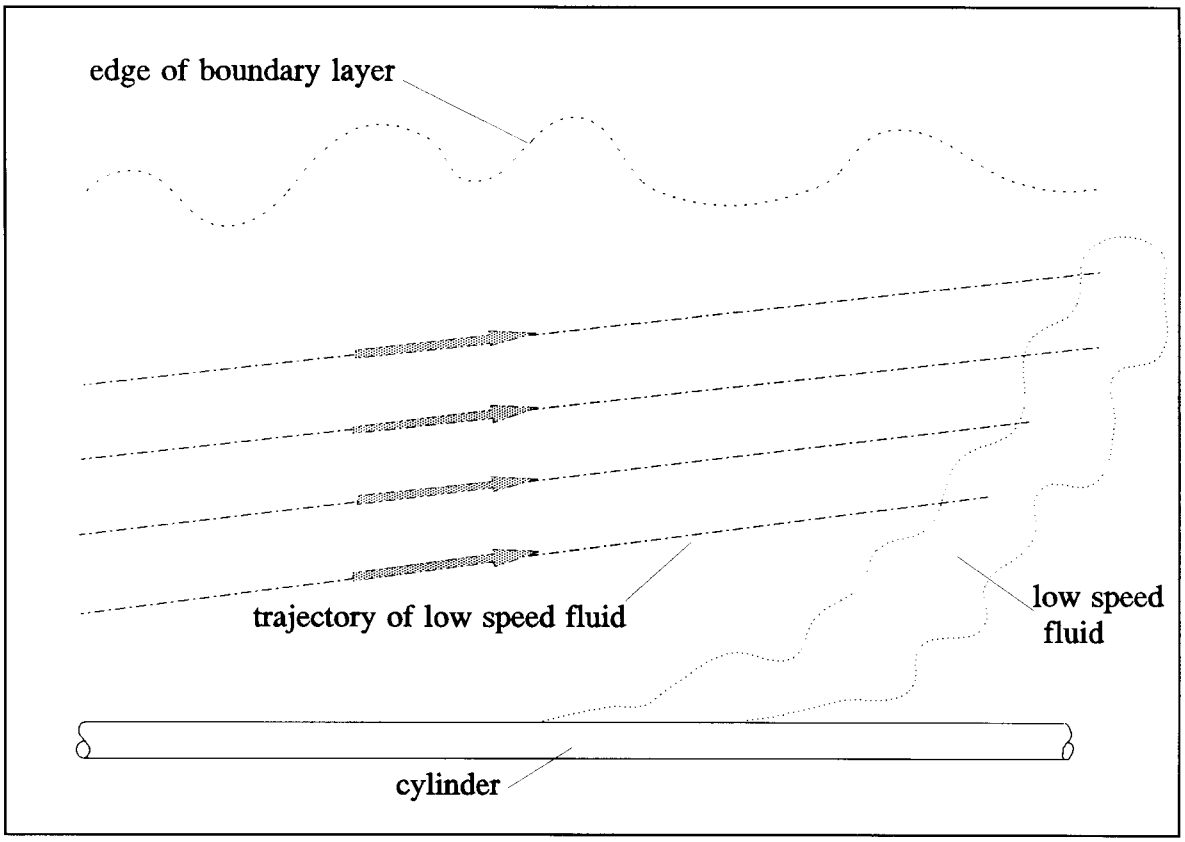

Figure 7.18 Diagram illustrating the formation of fronts of low speed fluid.

7.5 Correlation of Cross-flows with Low-speed Fronts

As the fluid within the low-speed front has a radial velocity directed outward from the cylinder surface, it is reasonable to conclude that the front consists of inner-layer low-velocity fluid that is moving away from the surface. On the view that the entire front originates near the cylinder surface, it follows that the outer regions of the front consist of inner-layer fluid originating further upstream than the fluid supplying the inner region of the front. An examination of the flow close to the cylinder surface has therefore been made to determine the general nature of the processes which result in the outward migration of inner-layer fluid.

Simultaneous measurements of the longitudinal velocity-perturbations at points on opposite sides of the cylinder, and at various axial separations, have been made with very large samples of 500 seconds duration, (ensemble sizes $N > 25{,}000$). The arrangement of the hot wire probes was similar to that shown in Figure [7.10], but with one probe above the cylinder and the other below. The resulting ensemble averages for the detection of a low-speed spot on one side of the cylinder at ($y_1 = 1$ mm, $\phi_1 = 0°$, $x_1 = 0$) and the corresponding velocity on the opposite side of the cylinder, at ($y_2 = 1$ mm, $\phi_2 = 180°$, $x_2 = x_1 + \Delta x$), are shown in Figure [7.19] for the secondary probe located $\Delta x = 0$, 2, 7.5 and 10 mm upstream and downstream of the low-velocity-detection probe. The large sample sizes used here were required to distinguish clearly the relatively weak secondary velocity peaks shown in Figure [7.19] from the general turbulence. These secondary velocity peaks are also shown expanded to a larger scale for additional clarity in the lower graph of Figure [7.19].

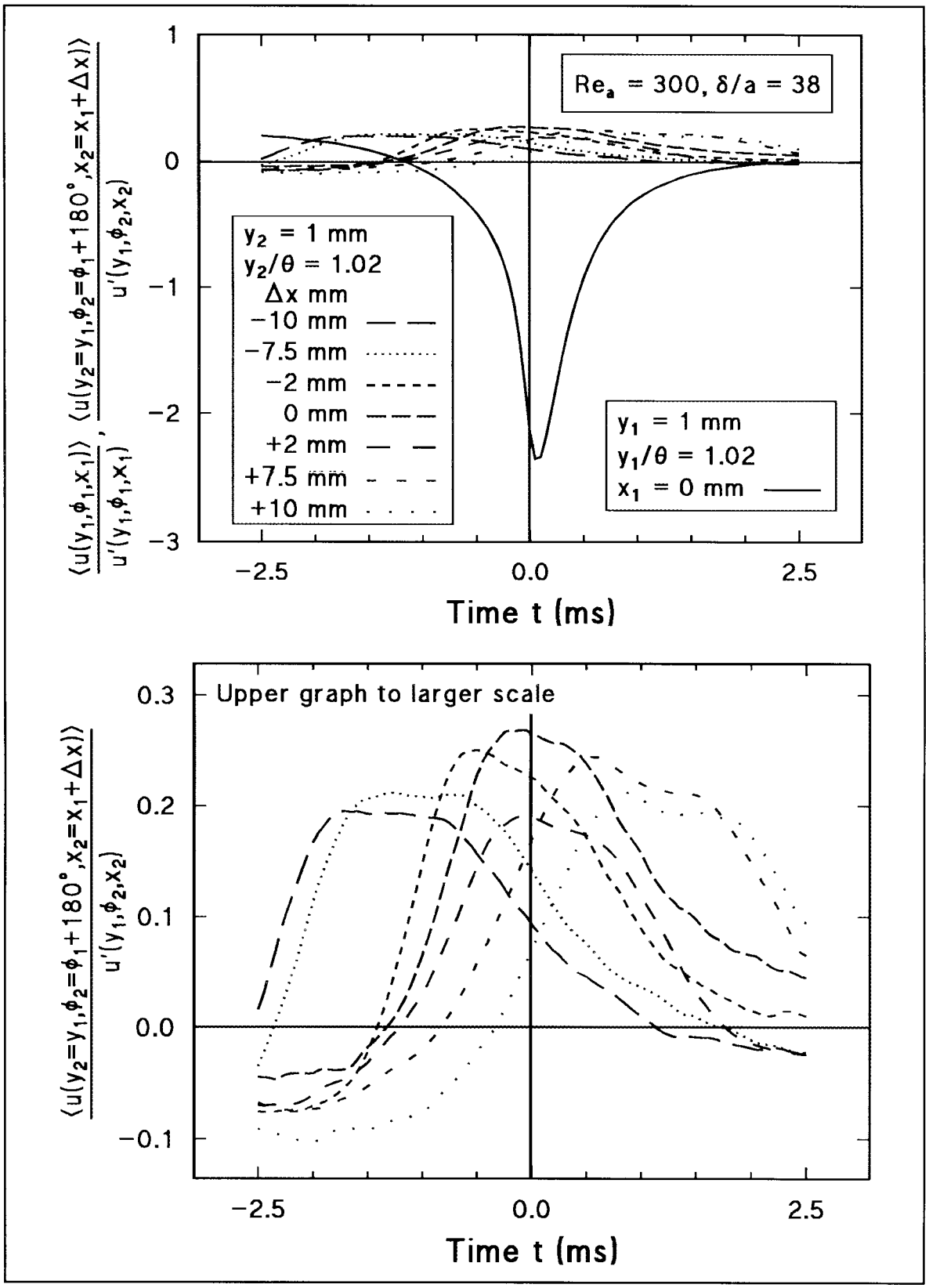

Figure 7.19 Ensemble averages of the longitudinal velocity on opposite sides of the cylinder with various axial separations Δx, Re_a = 300, y_1 = 1 mm, ϕ_1 = 0°; y_2 = 1 mm, ϕ_2 = 180°; $\Delta x = (x_2 - x_1)$.

The ensemble averages of the streamwise velocity $\langle u(y_2 = 1 \text{ mm}, \phi = 180°, x_2)\rangle$ on the opposite side of the cylinder to the low-speed-spot detector, over the duration time of a low-speed spot, shown in Figure [7.19], clearly indicate a period of higher-than-average streamwise velocity upstream prior to the detection of the low-speed spot. High-speed fluid also occurs directly opposite the detector at the time the low-speed spot is detected, and persists for some distance downstream. The duration time of increased velocity, and the time delay between detection of a low-speed-spot and the detection of the high-speed fluid at different axial locations, indicates that the region of high-speed fluid extends for approximately 30 mm ($\simeq 2\delta$ or $\simeq$ 30 cylinder diameters) in the axial direction, and that it is being convected downstream at a speed of approximately 0.8 U_1 (that is, the local mean velocity). The occurrence of this distinctive velocity feature, rather than random turbulence, is consistent with the hypothesis that the low-speed fronts are associated with movements of fluid across the cylinder: inward movement of high-speed fluid on one side of the cylinder giving rise to an outward movement of low-speed fluid on the other - in accord with the cross-flow ideas put forward by Luxton, Bull and Rajagopalan, 1984, and Lueptow and Haritonidis, 1987. (However, it should be noted that this result, in itself, would be consistent with a bodily lateral movement or oscillation of the whole boundary layer.)

If a cross-flow is responsible for transporting the fluid associated with an inner-layer low-speed spot to the outer part of the boundary layer, it is to be expected that the spot would be associated with a radial outflow ($v>0$) in its immediate vicinity (as established in section 7.4) and, at the same time, with a radial inflow ($v<0$) on the opposite side of the cylinder. Measurements were made to investigate this expectation. The observation that the time delay between the high- and low-velocity peaks on opposite sides of the cylinder (Figure [7.19]) approaches zero as the axial separation of

the probes approaches zero suggests that the region of high streamwise-velocity that would participate in the cross-flow extends radially outwards for some distance. As there is little variation with axial position of the axial extent of the region of the high-speed flow identified in Figure [7.19], these tests have been conducted with zero axial-displacement between the velocity probes.

Fluid with high streamwise-speed on the side of the cylinder opposite to a low-speed spot, has been detected in two ways: firstly by replacing one of the two single-hot-wire probes (at zero axial separation) with a cross-wire probe to determine both the axial and radial components of the velocity peaks shown in Figure [7.19]; and secondly to examine, simultaneously, the velocities at two points at the same radial distance for a range of different angular separations, using two single-wire probes.

The results of measurements with a cross-wire probe at (y_2 = 2 mm, $\phi_2 = 180°$, $x_2 = x_1$) and (y_2 = 4 mm, $\phi_2 = 180°$, $x_2 = x_1$) opposite a single-wire probe at (y_1 = 1 mm, $\phi_1 = 0°$, x_1), with axial separation $\Delta x = (x_2 - x_1) = 0$, are shown as ensemble averages (N > 3,000) of 50-second samples in Figures [7.20] and [7.21]; the detection of low-speed spots is made at the single-wire probe. The cross-wire probe records radially-outward flows as positive v-fluctuations, and increases in the U-velocity as positive u-fluctuations. The small ensemble-average values of the secondary velocities shown in Figures [7.20] and [7.21] are also shown expanded to a larger scale in the lower graph of each figure.

The period of increased velocity previously detected by a single hot-wire is again apparent in the measurements of the u-velocity component directly opposite the

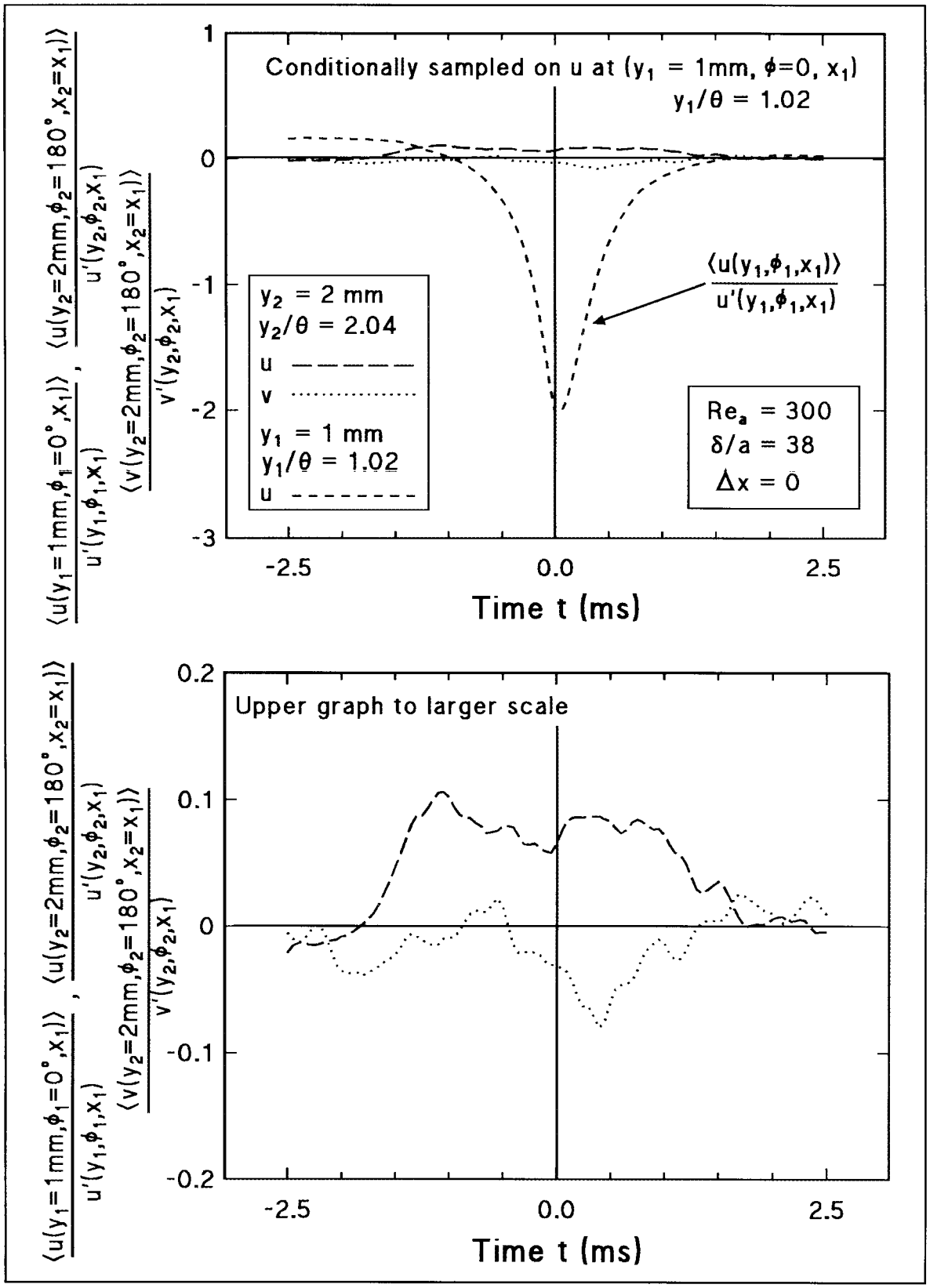

Figure 7.20 Ensemble averages of the u- and v-velocity components on the opposite side of the cylinder to a low-speed spot. u-wire at (y_1 = 1 mm, ϕ_1 = 0°, x_1); X-wire at (y_2 = 2 mm, ϕ_2 = 180°, x_2); $\Delta x = (x_2 - x_1) = 0$.

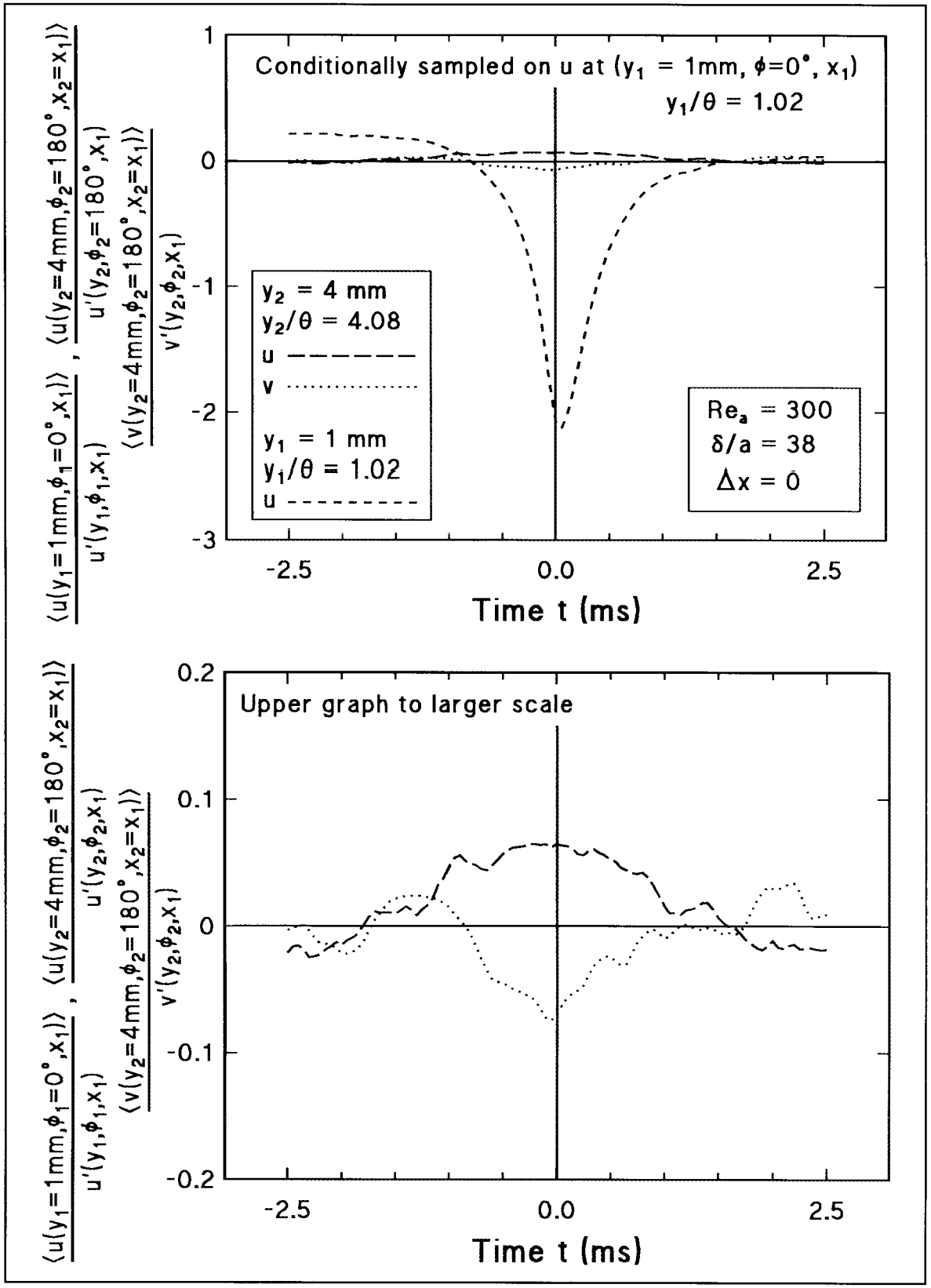

Figure 7.21 Ensemble averages of the u- and v-velocity components on the opposite side of the cylinder to a low-speed spot. u-wire at (y_1 = 1 mm, ϕ_1 = 0°, x_1); X-wire at (y_2 = 4 mm, ϕ_2 = 180°,x_2); $\Delta x = (x_2 - x_1) = 0$.

point of low-speed-spot detection at the time of detection shown in Figures [7.20] and [7.21]. The observation that this high u-velocity persists at points of increasing radial distance from the cylinder surface on the opposite side of the cylinder, (Figures 7.20 and 7.21 for y_2 = 2, 4 mm respectively), suggests that the high-speed flow is part of a structure within the turbulence that is large relative to the cylinder diameter.

The measured ensemble average v-velocities, enlarged by a factor of ten, are shown in the lower graphs of Figures [7.20] and [7.21]. The radial velocity appears as a small negative peak, indicating a small radially-inward velocity component of the high-speed flow opposite the point of detection of a low-speed spot at a time close to the detection time. In interpreting these measurements of the very small averaged velocity-components, the size of the velocity sample must be considered. As these results have been produced from a 50-second segment of data, yielding N > 3,000 low-speed-spot detections, a small velocity peak still visible in the resulting ensemble is a significant feature of the flow.

A smoothed form of the characteristic radial-velocity signature has been obtained by high-order-polynomial regression of the data, which effectively filters out the shorter-period fluctuations. Polynomial regressions of up to thirteenth order were applied to both the longitudinal and radial velocity fluctuations measured opposite the low-speed spot. The results of ninth-order polynomial regressions are shown in Figure [7.22] for the u- and v-data shown in Figures [7.20] and [7.21]. Polynomial regressions of order higher than nine did not produce any appreciable further changes in the appearance of the velocity variation. The characteristic feature of the radial-velocity fluctuation opposite a low-speed spot, shown by Figure [7.22], appears to be an inward

flow with a peak magnitude of about 6% of the radial rms value, occurring at a time very close to the low-speed-spot detection time.

Further examination of the role of inward radial-velocity fluctuations has been made by conditional sampling of the radial velocity for the detection of large inward radial-velocity fluctuations defined as twice the rms value below the (zero) mean value, and simultaneous sampling of streamwise velocity fluctuations on the opposite side of the cylinder. The resulting ensemble averages of the u-velocity (measured by a single-wire probe) on the opposite side of the cylinder to a large inward radial velocity fluctuation are shown in Figure [7.23]. On the scale of the large inward radial-velocity fluctuation there is no obviously-discernible feature in the corresponding u-velocity on the opposite side of the cylinder. The data of Figure [7.23] are also shown enlarged by a factor of ten in Figure [7.24], which indicates that large inward radial fluctuations, which might be expected to result in the formation of low-speed spots on the opposite side of the cylinder apparently do not do so. These results suggest that the high speed flow (with a small radially inward component) is much more widely dispersed around the cylinder than the resulting low speed spot.

The trajectory of the 'cross-flow' fluid associated with the formation of a low-speed spot on the opposite side of the cylinder can be obtained from the axial- and radial-velocity components of the 'cross-flow' fluid ($U_x = U + \langle u \rangle$ and $U_y = \langle v \rangle$ respectively) approaching the cylinder, as determined by the mean-flow velocities and the ensemble averages shown in Figure [7.22]. Values of the relevant parameters are given in Table [7.1]. The values used for $\langle u \rangle / u'$ and $\langle v \rangle / v'$ are the largest excursions from the mean flow in the smoothed ensemble averages shown in Figure [7.22]. The

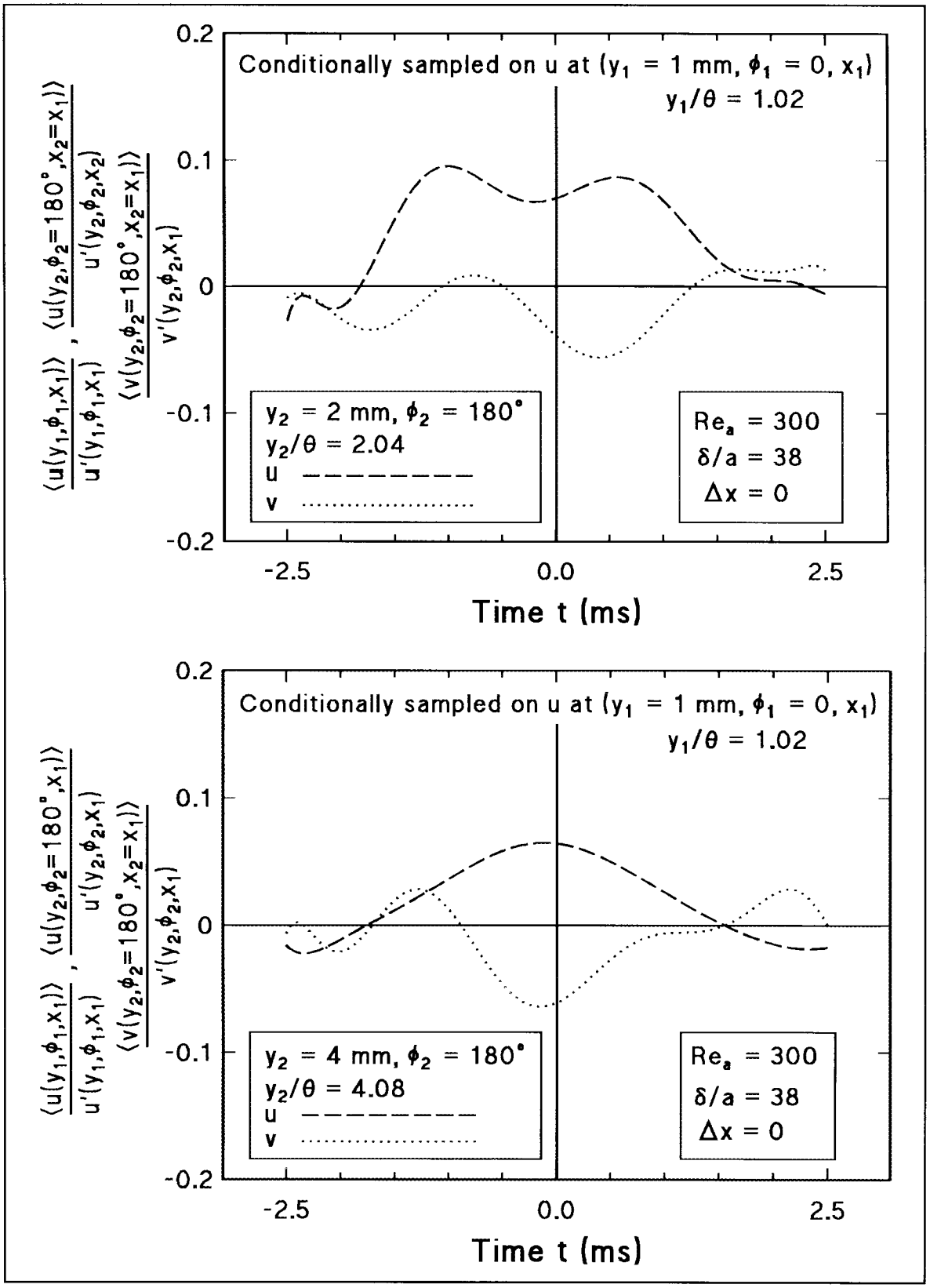

Figure 7.22 9th order polynomial regression of the u- and v-velocity components on the opposite side of the cylinder to a low-speed spot at y_1 = 1mm, X-wire y_2 = 2, 4 mm.

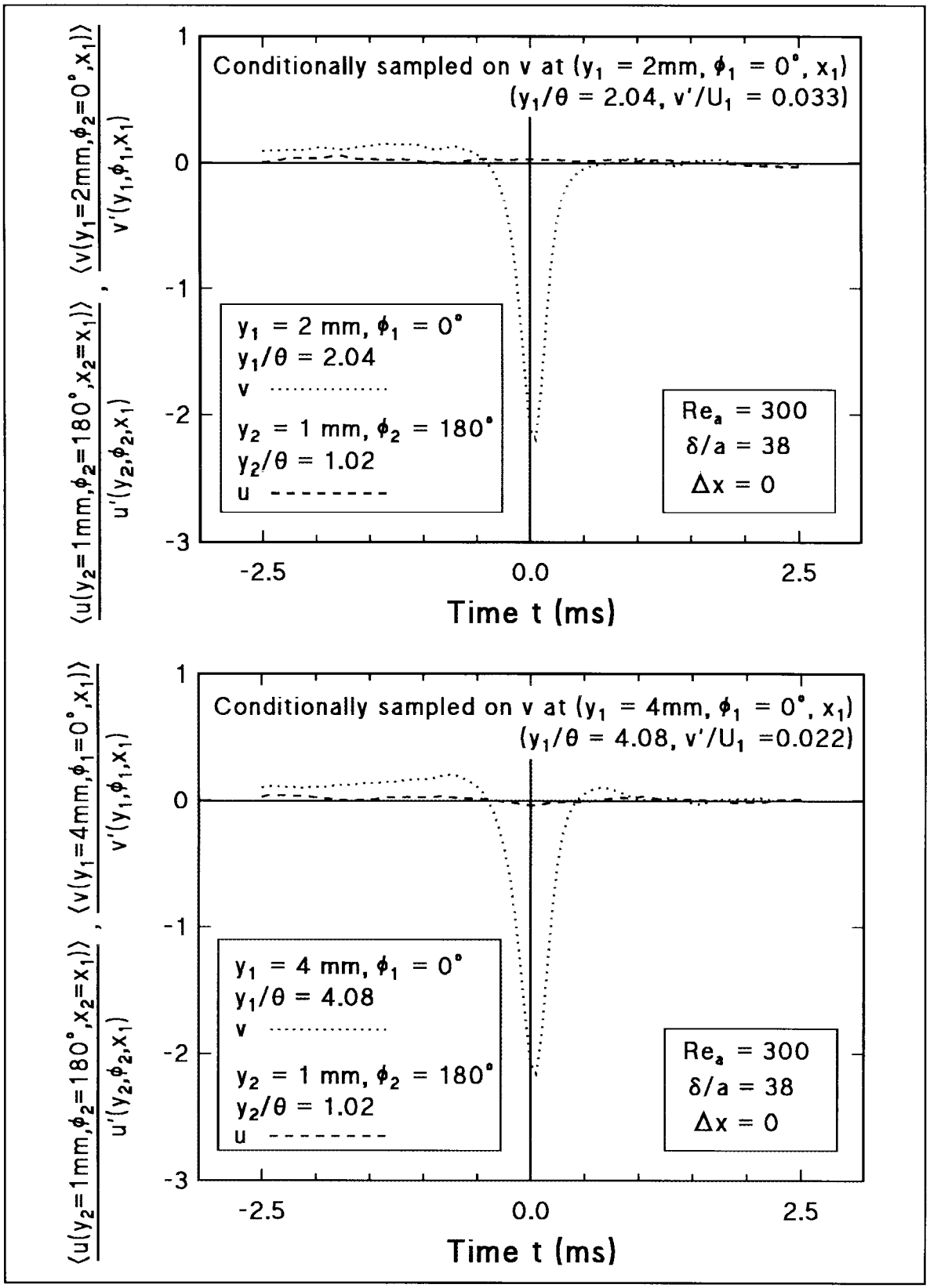

Figure 7.23 Ensemble average of the velocity at (y_2 = 1 mm, ϕ_2 = 180°, x_2) on the opposite side of the cylinder to an inward v-fluctuation at (y_1 = 2 mm, ϕ_1 = 0°, x_1) (upper figure); (y_1 = 4 mm, ϕ_1 = 0°, x_1) (lower figure); $\Delta x = (x_2 - x_1) = 0$.

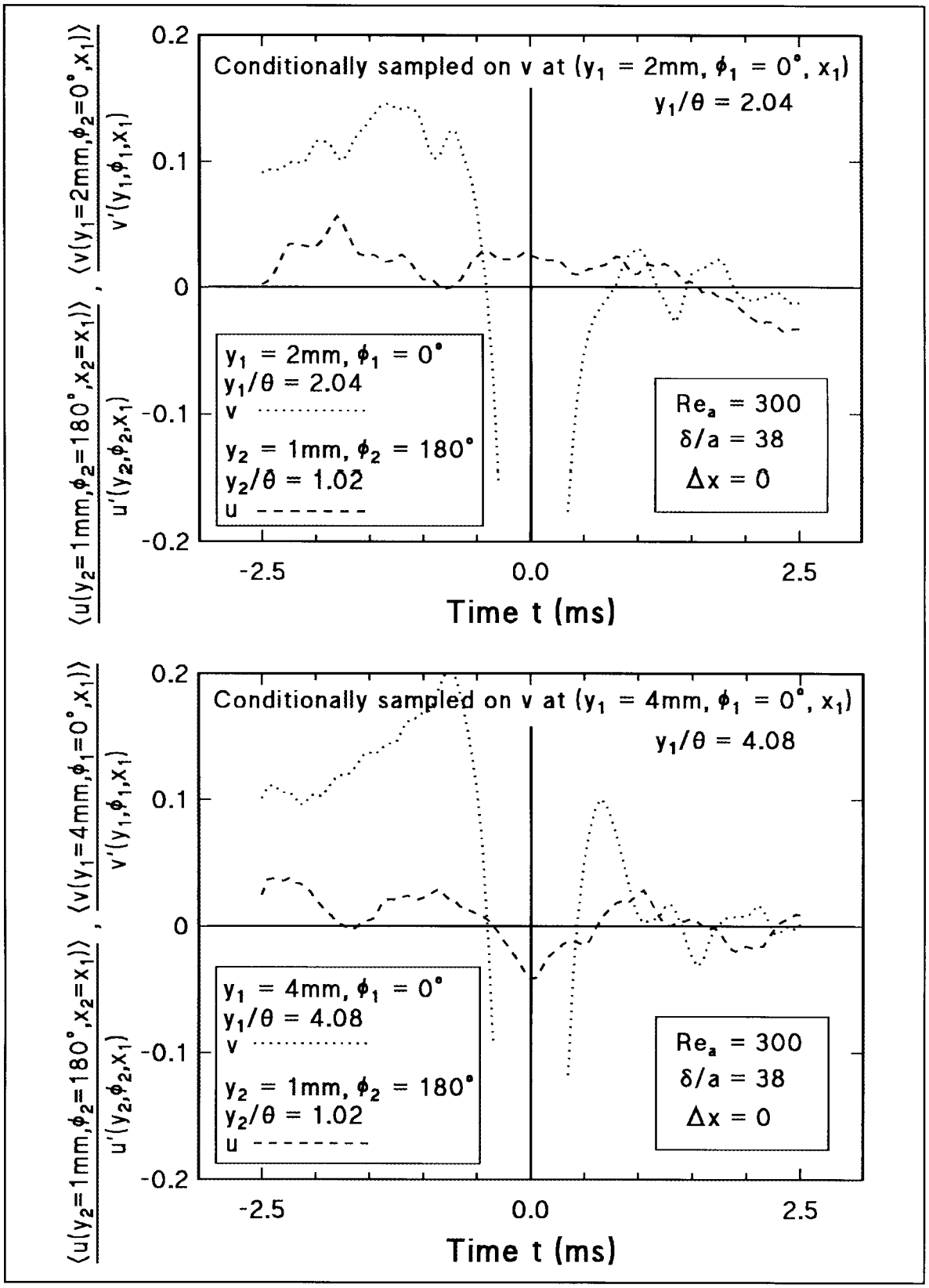

Figure 7.24 Expanded scale view of the ensemble-average velocity at (y_2 = 1 mm, ϕ_2 = 180°, x_2) on the opposite side of the cylinder to an inward v-fluctuation at (y_1 = 2 mm, ϕ_1 = 0°, x_1) (upper figure); (y_1 = 4 mm, ϕ_1 = 0°, x_1) (lower figure).

values used for v'/U_1 are determined from the complete v-velocity signatures which are conditionally sampled to form the ensemble averages shown in Figure [7.23].

The cross-flow approaches the cylinder at a very small angle to the main flow direction β_{avg} in the order of 0.1°. Table [7.1] also includes flow inclinations typical of the general turbulence determined from the magnitude of the rms radial-velocity fluctuations relative to the local mean axial velocity (without conditional sampling). These angles β_{rms} are significantly larger, in the order of 2°. These fluid trajectory angles are within the regimes of cylinder yaw angle which are associated with boundary layer asymmetry in chapter 4, and with vortex shedding in chapter 5.

In the second method of investigating the formation of low-speed spots, simultaneous u-component measurements have been made with two hot-wire probes with zero axial-separation, located at $y_1 = y_2 = 1$ mm, over a range of angular separations.

y/θ	U/U_1 (fig 4.3)	u'/U_1 (fig 4.9)	$\langle u \rangle/u'$ (fig 7.22)	v'/U_1 (fig 7.23)	$\langle v \rangle/v'$ (fig 7.22)	U_y/U_x	β_{avg}	v'/U	β_{rms}
2.04	0.890	0.065	0.09	0.033	-0.06	0.0022	0.13°	0.037	2.1°
4.08	0.926	0.055	0.06	0.022	-0.06	0.0014	0.08°	0.024	1.4°

Table 7.1 'Cross-flow' fluid velocity components U_x and U_y determined from ensemble averages of the velocity on the opposite side of the cylinder when a low speed spot is detected and the resulting average fluid trajectory angle β_{avg} (= $\tan^{-1} U_y/U_x$), and the rms average trajectory angle β_{rms} (= $\tan^{-1} v'/U$) of the general turbulence.

One hot-wire was used for the detection of low-speed spots, leading to the ensemble average $\langle u(y_1 = 1 \text{ mm}, \phi_1 = 0°, x_1)\rangle$. Ensemble averages $\langle u(y_2 = 1 \text{ mm}, \phi_2, x_2 = x_1)\rangle$ from the second hot-wire of the velocities at points $\phi_2 = 45°$, 90° and 180° around the cylinder, corresponding to detection of a low-speed spot (at $\phi_1 = 0°$) (Figure [7.25]) show that high-speed fluid occurs at all ϕ in the range $45° < \phi < 180°$. Thus, at y = 1 mm, the region of high-speed flow associated with the formation of a low-speed spot on the opposite side of the cylinder (at $\phi = 180°$) to the detected low-speed spot (at $\phi = 0°$), assuming symmetry, extends around the cylinder for at least 270° to within at least 45° of the spot itself.

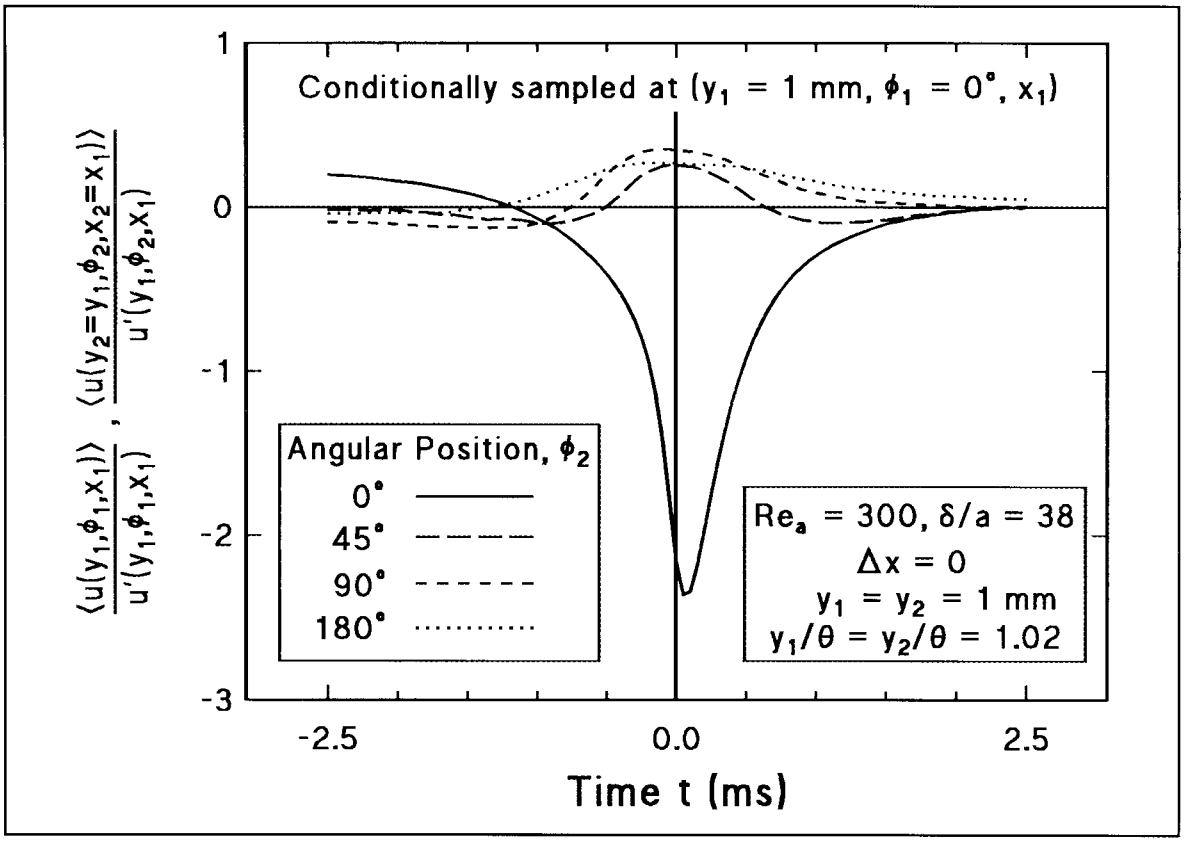

Figure 7.25 Ensemble averages of the velocity at different angular locations around the cylinder at $y_2 = 1$ mm, $y_2/\theta = 1.02$, $\Delta x = (x_2 - x_1) = 0$, corresponding to a low velocity spot at $(y_1 = 1 \text{ mm}, \phi_1 = 0°, x_1)$.

The results in Figure [7.25] indicate, as found previously (p.205), that the high-speed flow associated with low-speed spot formation occupies a region with an axial extent of some tens of cylinder diameters, is widely dispersed angularly around the cylinder, and has a small transverse velocity directed towards the cylinder. Thus, the high-speed flow completely envelops the cylinder, and the cylinder would do little to impede the transverse movement of this fluid.

Further insight into the relationship between the characteristic u-velocity signature of a low-speed spot and the simultaneous characteristic velocity distribution at other points around the cylinder can be gained from a conditional correlation coefficient R, calculated from the conditionally-detected time-history of a low-speed spot and each of the corresponding secondary velocity-time-histories. The conditional correlation coefficient is defined as

$$R = \frac{\frac{1}{N}\sum_{k=1}^{N}\left(\frac{1}{T_n}\sum_{1}^{T_n} {}^{k}u_1(n)\ {}^{k}u_2(n+n_\tau)\right)}{\left[\frac{1}{N}\sum_{k=1}^{N}\left(\frac{1}{T_n}\sum_{1}^{T_n} {}^{k}u_1(n)^2\right)\right]^{\frac{1}{2}}\left[\frac{1}{N}\sum_{k=1}^{N}\left(\frac{1}{T_n}\sum_{1}^{T_n} {}^{k}u_2(n)^2\right)\right]^{\frac{1}{2}}} \qquad [7.2]$$

where ${}^{k}u_1(n) = {}^{k}u(y_1, \phi_1, x_1, t)$ is the conditionally-detected u-component of the velocity of the k-th low-speed spot at time t (n data points after detection),

${}^{k}u_2(n) = {}^{k}u(y_2, \phi_2, x_2, t)$ is the u-component of the corresponding k-th secondary velocity at time t, and

$T_n = 5$, the number of data points in the time-length of the record, and

n_τ is the number of data points in the time delay τ.

The variation of R with time-delay τ can in some cases provide information more clearly than the ensemble averages of the velocity signatures.

Conditional correlations of this form, based on the same data segments as those used to produce the ensemble averages in Figure [7.25], are shown for each of the angular separations ϕ_2 in Figure [7.26]. The most prominent feature is the strong negative correlation at zero time-delay at all ϕ_2 values, corresponding to the spatial correlation between the low velocity at the spot-detection point and the high velocity at the secondary points around the cylinder. (It should be emphasised that the correlation values are calculated for the conditionally-sampled data segments only, and that a spatial correlation between two complete velocity time series would have a much lower magnitude as a result of the inclusion of large periods of uncorrelated random turbulence.)

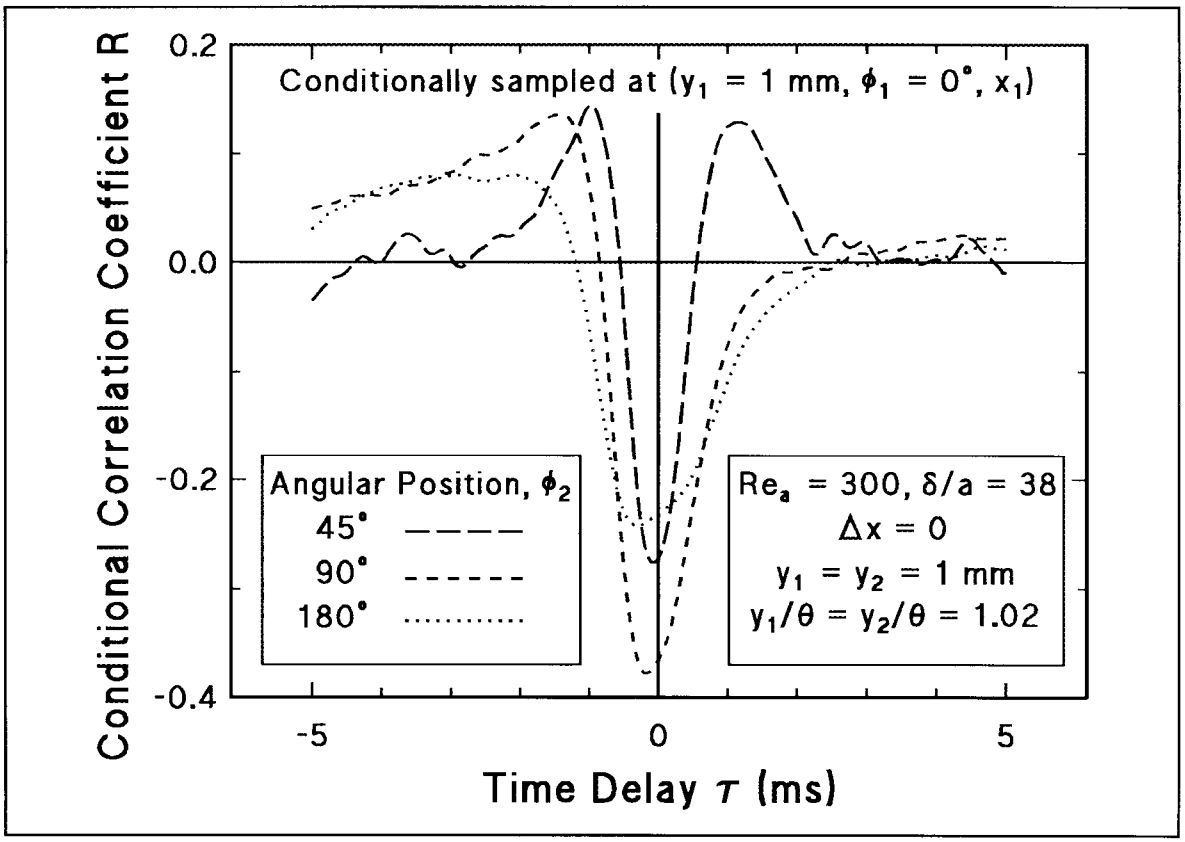

Figure 7.26 Variation of the conditional correlation coefficient R with time delay, at various angular locations around the cylinder, at y = 1 mm, y/θ = 1.02. Δx = 0, for a low velocity spot detected at ϕ = 0° at t = 0.

The positive correlations at negative time-delays in Figure [7.26] correspond to the low secondary velocities shown by Figure [7.25] prior to the appearance of the high velocity associated with the formation of the low speed spot (at $\phi = 0°$). The positive correlation peak between the velocities at $\phi = 0°$ and $\phi = 45°$ at a positive time-delay corresponds to the period of low velocity detected at $\phi = 45°$ after the occurrence of the negative peak of the spot.

The additional information that can be derived from the conditional correlations, which is not as apparent in the ensemble averages, is the time delay between the two velocity signals that results in the maximum correlation. These values can be estimated from the time difference between the peaks of the ensemble averages of secondary velocity and the spot-detection velocity, for both the positive and negative secondary-velocity 'peaks' shown in Figure [7.25], but are more easily measured from the conditional correlations of Figure [7.26]. From the latter, maximum negative correlation with the low-speed spot occurs at negative time-delays of 0.1, 0.2 and 0.4 milliseconds and maximum positive correlation at negative time delays of 1, 1.4 and 2 milliseconds, at angular locations of $\phi = 45°$, 90° and 180°, respectively, in each case.

The decrease in magnitude of the time delay with decreasing angular displacement as the low-speed-spot position is approached is consistent with a cross-flow moving over the cylinder, progressing past each of the secondary probes in turn, and progressively moving low-speed fluid ahead of it to the 'lee' side of the cylinder to form the low-speed spot. The positive correlation between the low-speed-spot velocity and that at $\phi = 45°$, at a positive time delay, indicates that, at this time in the process

of low-speed-spot formation, low-speed fluid that will eventually form part of the spot still extends around the cylinder from $\phi = 0°$ to at least $\phi = 45°$, and still contains the secondary probe at y = 1 mm.

The difference in behaviour between the different angular locations can be qualitatively explained by considering the relative motion of each probe through the boundary-layer fluid, shown diagrammatically in Figure [7.27] for a cross-flow that directs low-speed inner-boundary-layer fluid outwards towards the conditional-sampling probe at $\phi = 0°$. If such a cross-flow occurs (with minimal distortion of the velocity distribution, for the purposes of illustration) and is followed by re-establishment of an equilibrium boundary-layer mean-velocity profile, the relative paths of each probe shown in Figure [7.27] will have the following results:

At $\phi = 0°$ the velocity will decrease to a very small minimum as the probe moves through the steep near-wall mean-velocity gradient in the boundary layer, and return to the mean value as the equilibrium boundary layer is re-established.

At $\phi = 90°$ and $180°$ the velocity will increase only slightly to a maximum as the probe moves outwards through the slowly-increasing velocity in the outer part of the boundary layer, and decrease to the mean value as the boundary layer regains its undisturbed form. Clearly, this will produce a strong negative correlation with the velocity variation at the $\phi = 0°$ probe.

At $\phi = 45°$, the velocity will initially decrease to a minimum at $\phi = 90°$ as the probe moves inwards and then increase to reach a maximum at $\phi > 90°$: as the boundary layer flow returns to normal, this variation will be reversed.

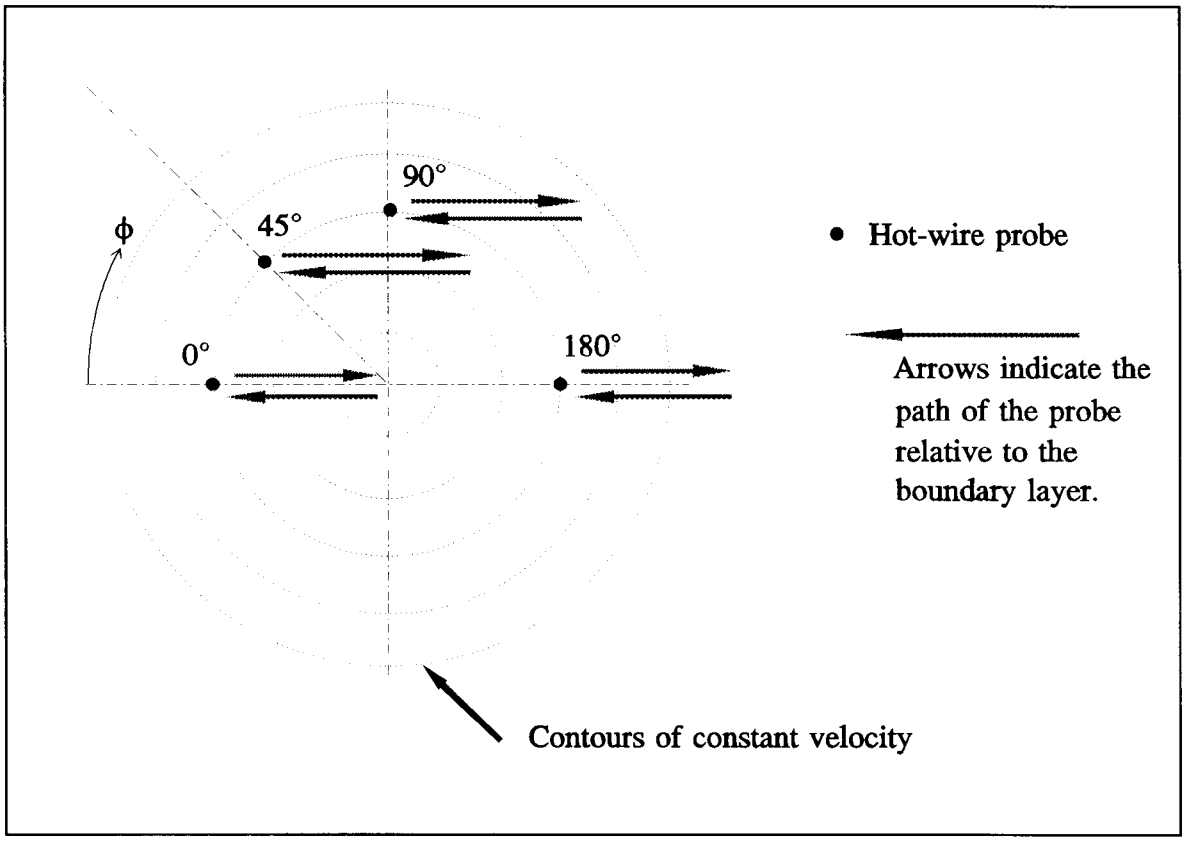

Figure 7.27 Diagramatic representation of motion of hot wire probes relative to an axisymmetric boundary layer as a result of cross-flow.

The simple cross-flow process of the type shown in Figure [7.27] faithfully reproduces the variation of velocity with time at each angular position in the ensemble averages in Figure [7.25], although the model is too simple to account for the variation in time-delay between correlated events at different points around the cylinder shown by the conditional correlations of Figure [7.26]. Nevertheless, the model does add plausibility to the hypothesis that cross-flows in the turbulent boundary layer can strip low-speed inner-layer fluid from the cylinder and transport it to the outer part of the boundary layer.

The presence of the cylinder can be expected to modify the simple model presented above, and particularly details of the flow. For example, as the cross-flow approaches the cylinder, the 90° probe detects a lowered velocity before following the pattern shown in Figure [7.27]. This can be attributed to the progressive displacement of low-speed boundary-layer fluid by the high-speed fluid as it passes around the cylinder, under the effect of the cross-flow.

The distributions of mean and rms velocity across the boundary layer previously determined for axial flow with Reynolds number $Re_a = 300$ (Figures [4.3] and [4.9]) indicate that the fluid with a streamwise velocity fluctuation more than twice the rms fluctuation below the mean, detected in the outer boundary layer, originates from the inner region of the boundary layer, and is not simply neighbouring fluid of slightly lower velocity shifted radially outwards: for $y/\theta \gtrsim 2$, $2u' \sim 0.1\ U_1$, and Figure [4.3] show that shifts of more than 40 θ could scarcely produce such a large velocity excursion. It is therefore concluded that cross-flows of boundary-layer fluid eject a local section of the inner-layer core of low-speed fluid into the outer layer. Removal of low-speed fluid in this way necessitates generation of a new inner layer. The high velocity-gradient between the cylinder surface and both the high-velocity fluid in the cross-flow and the newly-arriving fluid with unperturbed mean-velocity constitutes an enhanced source of vorticity and of turbulence generation, which does not occur for flat plate boundary layers.

The presence of the low speed fronts spanning the entire boundary layer, and their interaction with the surrounding higher speed flow, might also be expected to increase Reynolds stresses (although no direct evidence for this is presented here) and

consequently to result in increased generation of turbulence energy. This interaction appears to provide a mechanism of turbulence generation unique to flow over long slender bodies immersed in very thick turbulent boundary layers, which can occur in addition to the turbulence-generating mechanisms identified in flat-plate turbulent boundary layers.

7.6 Summary of Results

A detailed study of an axisymmetric turbulent boundary layer with $\delta/a = 38$, at one typical Reynolds number ($Re_a = 300$), using both flow visualisation and velocity measurement, has revealed the presence of characteristic organised structures in the thick axisymmetric turbulent boundary layer. The structures take the form of "fronts" of low-speed inner-boundary-layer fluid that has left the cylinder surface and is moving outwards across the boundary layer.

Investigation of the origin of these structures has identified local turbulent cross-flows within the boundary layer as the probable cause. The slender cylinder offers little impedance to random transverse motion of the boundary-layer fluid caused by the larger cross-flows within the layer; and it appears that these cross-flows continually remove inner-layer fluid from the cylinder surface to form unattached regions or "spots" of low-velocity fluid. The removal of inner-layer fluid is also a continuous process (over a short time) in each particular cross-flow event. In the course of such an event, inner layer fluid from a finite axial length of the cylinder is progressively removed and transported by the cross-flow to form a low-speed front. The necessary continual regeneration of the inner layer, and the interaction between the low-speed fronts and the outer layer, constitutes a new process of vorticity and turbulence generation, specific to axisymmetric boundary layers with large δ/a.

The process of continual, irregular, inner-boundary-layer separation bears some similarity to the regular, periodic, separation process that characterises formation of a

vortex street in the wake of a slightly yawed cylinder. The average instantaneous yaw angles between radially-inward turbulence velocity fluctuations and the (unyawed) cylinder axis are of similar magnitude to the yaw angles associated with vortex shedding from cylinders at small geometric yaw angles.

Structures in the axisymmetric boundary layer identified by flow visualisation (Figure [7.2]) are believed to consist of separated inner-layer fluid and appear to roll up into vortices within the boundary layer. The orientation of successive separations is random, and their frequency irregular, in accord with the random nature of the turbulent cross-flows which produce them.

The identification of this process in axial flow with similarities to periodic vortex shedding is in conformity with the wake-like nature of boundary layers with large δ/a. Such a process would also be expected to be significant in relation to the practical problem of identifying and reducing low-frequency noise generated by axial flow over towed sonar-array cables.

8. RESEARCH FINDINGS

The results of an investigation of long slender cylinders in axial and near-axial flow are presented in the preceding chapters. The investigation has involved aspects of three broad areas of fluid mechanics: boundary layer properties, vortex shedding and turbulence mechanisms. Each of these areas is the subject of extensive previous and ongoing research which is summarised in a literature review to set the current experimental investigation in context.

The experiments have been focused on two simple, well defined geometric arrangements, a long slender cylinder in axial flow, and a cylinder in near-axial flow. The study of the boundary layer properties and associated turbulent-flow mechanisms has been concentrated on the axisymmetric boundary layer established on a cylinder in axial flow. The obvious standard of reference for such a study is the classic case of flow over a flat plate in zero pressure gradient, although even in this case turbulence mechanisms in the boundary layer are still far from completely understood (see, for example, Chong et.al. 1998).

In the present work, an examination has been made of the effect of large transverse curvature on the turbulence mechanisms which have been identified in flat plate boundary layers and extended to cylinders of modest transverse curvature by previous researchers (see, for example, Lueptow and Jackson, 1991). It is concluded that there is an additional possible mechanism of turbulence generation in boundary layers of large thickness relative to the cylinder diameter (large δ/a) which becomes increasingly significant as the transverse curvature of the surface increases. The postulated mechanism results from the negligible impedance presented by a slender cylinder to the turbulent cross-flows within a thick boundary layer.

Detailed investigation of the boundary-layer turbulence in such a flow indicates that cross-flows can strip inner-layer fluid from the cylinder and transport it into the outer layer. Repeated stripping of inner-layer fluid necessitates continual regeneration of the inner boundary layer, and this constitutes an additional turbulence-generation mechanism.

The effects of small angles of yaw have been investigated, firstly as asymmetry in the boundary layer at very small yaw angles, and secondly as the occurrence of regular vortex shedding at larger yaw angles. The boundaries of the flow regime where regular vortex shedding occurs have been identified, and the vortex-shedding frequencies quantified. The present results extend the range of yaw angles for which regular vortex shedding is known to occur (Hanson 1966, Ramberg 1983) into the regime of near-axial flow. At these small yaw angles the contribution of the axial velocity component to the vortex-shedding process is shown to be significant, in contrast to flow at large yaw angles where vortex shedding is dominated by the velocity component normal to the cylinder axis.

The primary aim of this investigation has been to obtain a clearer understanding of the flow processes that occur in thick axisymmetric turbulent boundary layers. To that end, the experiments have been conducted over a quite narrow range (variation by a factor of two only) of relatively low Reynolds numbers. To identify the broader dependence on Reynolds number and to represent specifically the higher Reynolds numbers corresponding to many practical applications, a Reynolds number variation of one or even two orders of magnitude would be desirable. Nevertheless, the mechanisms and general characteristics of flow at higher Reynolds numbers can reasonably be expected to be similar to those identified by the present investigation.

8.1 Mean-velocity Distribution in Axisymmetric Boundary Layers

Transition from laminar to turbulent flow in the axisymmetric boundary layer has been found to be determined primarily by two non-dimensional parameters, the cylinder Reynolds number Re_a and ratio x/a of axial distance along the cylinder to cylinder radius. When transition has taken place, these two parameters also determine the thickness of the turbulent axisymmetric boundary layer that is established on a cylinder in axial flow: to obtain a layer with large δ/a, both large x/a and small Re_a are required. The combinations of Re_a = 300, 450, 600 and x/a = 6000 were selected for the investigation; these give values of δ/a = 38, 33 and 31. Such large values of δ/a can be expected to ensure significant effects of transverse curvature on the flow in the outer region of the boundary layer. Significant effects on the inner region are to be expected only if, also, the ratio of cylinder radius to the wall scale, a^+, is small. Values of a^+ corresponding to the preceding values of δ/a are 22.4, 33.0 and 40.8 respectively, and these appear to be sufficiently small to produce considerable effects on the inner layer.

Mean-velocity profiles have been examined in terms of inner-layer and outer-layer length scales. Of the two definitions of momentum thickness commonly used for the integral (outer) length-scale of axisymmetric boundary layers, θ_1 and θ_2 (equations 4.8 and 4.11), both of which are derived from an annular momentum-defect area, only the latter, θ_2 (which takes full account of the annular cross-sectional area of the boundary layer), is appropriate for axisymmetric boundary layers in general, and for thick (large δ/a) axisymmetric boundary layers in particular. Scaling of the radial coordinate y by θ_2 leads to similarity of outer-layer velocity-profiles over the range of Reynolds number investigated. (It is also found that the length scale θ defined by the

standard flat-plate-boundary-layer integral (equation 4.3) is equally effective in producing velocity-profile similarity over the Reynolds-number range of the investigation; and it has the advantage of being somewhat less sensitive to experimental errors at the outer extremity of the boundary layer.) Willmarth et.al.(1976) have shown that, when the mean-velocity distribution in the inner layer is considered in terms of wall scales U_τ and ν/U_τ, the effect of increasing transverse curvature is to produce a progressive divergence from the flat-plate "law of the wall" as δ/a increases and a^+ decreases. The present results (Figure 4.7) show the same effect of increasing transverse curvature, although in the present case the magnitudes of divergence are rather greater, apparently as a result of different Re_a values for the two sets of data. Both sets of experimental results indicate that for $\delta/a \gtrsim 30$ or $a^+ \lesssim 40\text{-}70$ the profile no longer has a logarithmic region.

Small angles of yaw, typically less than 1°, have, as found in previous investigations (Willmarth et.al. 1976), a major effect on the symmetry of an attached boundary layer. Contours of constant mean longitudinal velocity in planes normal to the cylinder axis demonstrate this extreme sensitivity to yaw angle: for example, at Re_a = 300, a yaw angle of only 0.5° results in a boundary layer thickness on the leeward side of the cylinder some 4.5 times greater than that on the windward side.

At yaw angles greater than about 1°, the boundary layer no longer remains attached; flow separation occurs and a regime of regular vortex shedding into the cylinder wake is established. The investigation of the larger cylinder yaw angles has been focused on the vortex-shedding processes which are then the dominant feature of the flow.

8.2 Vortex Shedding Behaviour

Vortex shedding from long cylinders in near-axial flow has been investigated by measurement of vortex shedding frequencies and by visualisation of the vortex-wake flow, in a series of experiments in which great care has been taken to eliminate extraneous effects. Particular attention has been paid to the avoidance of cylinder vibration and the maintenance of consistent cylinder end-conditions of a type least likely to affect the vortex shedding mechanisms; inconsistencies in previous experimental results have often been attributed to their neglect.

The flow regime, in terms of yaw angle and Reynolds number, within which regular vortex shedding occurs has been determined by observation of both the velocity signal measured in the cylinder wake and the associated frequency spectrum. An upper Reynolds-number boundary, increasing with yaw angle (to a maximum of $Re_a = 2200$ at $\beta = 8°$), has been determined for the range $0° \leq \beta \leq 10°$ of near-axial-flow yaw angles. At Reynolds numbers up to about 10% above this boundary, there is a transition range in which vortex shedding continues to occur, but not in the simple periodic manner observed below the boundary. Beyond the transition range, shedding ceases. A lower Reynolds-number boundary, similar to that found for cylinders normal to the flow, might be expected, but cessation of shedding was not observed at the lowest Reynolds number of the experiments ($Re_a \sim 60$). The determination of these boundaries extends the range of yaw angles for which regular vortex shedding is known to occur in near-axial flow.

8.2.1 Vortex-shedding frequencies

Frequencies of vortex shedding from cylinders normal to the flow are usually expressed as the Strouhal number $S = fd/U$ as a function of Reynolds number [$S = S(Re_d)$], or less commonly in terms of a frequency parameter $F = fd^2/\nu$ as $F = F(Re_d)$. For yawed cylinders, the most appropriate non-dimensional parameters with which to represent the relationship between the flow properties, the cylinder geometry and the vortex-shedding frequency are the frequency parameter F, Reynolds number (Re_a or Re_d) and yaw angle β. The use of F is preferred to S because frequency and velocity are then separated in the descriptive function.

The introduction of a yaw angle to the cylinder geometry adds this non-dimensional parameter to the functional relationship. The unknown effects of yaw on the variation of frequency along the cylinder axis require that an axial location term, x/a or x/d, also be included in the functional relationship, which then becomes $F = F(Re_d, \beta, x/a)$. Significant effects of axial location, if any, are expected to occur in near-axial flow, and to decrease to zero as β increases and normal flow ($\beta=90°$) is approached. At the small angles of near-axial flow examined here, no consistent variation of F with x/a is observed in the experimental results. However, it should be noted that at small β there is a tendency for the vortices to be formed in cells of constant frequency, and this might mask any weak dependence on x/a.

The present measurements of vortex-shedding frequency are consistent with previous results obtained by Van Atta (1968) at larger yaw angles: data from both

sources when cast in the form of Strouhal number as a function of yaw angle for constant Re_n, as used by Van Atta, form a continuous set, although the relationship between Strouhal number and yaw angle becomes more complex in the near-axial flow regime. The present results have been examined relative to those obtained both for cylinders normal to the flow and for cylinders at yaw angles above 45°. For the latter, the vortex frequency appears to follow the normal-cylinder results when the Reynolds number considered is based only on the normal component of the flow velocity. As β is decreased below 45° (that is, towards axisymmetric flow), the vortex-shedding frequency, at a given Re_n, diverges from the normal-cylinder results: at small β the frequency is always greater than that from a cylinder normal to the flow (at the same Re_n). These results make it clear that the contribution of the axial velocity-component to the vortex shedding process is by no means insignificant.

Thus, the present results conclusively refute the so-called "independence principle", which is based on the notion that only the normal velocity-component controls the vortex-shedding process. However, at the same time, they provide the experimental data on which alternative relationships might be based. The invalidity of the "independence principle" at small yaw angles indicates that the "principle" is invalid in general and that the axial velocity-component always has an effect on the vortex shedding behaviour, but that the effect becomes insignificant at yaw angles greater than about 45°.

An empirical relationship for the dependence of the frequency parameter on Reynolds number and yaw angle has been determined. It is based on the premise that effective values of free-stream velocity and cylinder diameter can be derived to extend

the classic frequency-parameter/Reynolds-number relationship of Roshko (1954), for cylinders normal to the flow, to yawed cylinders.

The effective velocity U^* which controls the vortex shedding is identified as the component $U_1 \sin(\alpha+\beta)$ of the free stream velocity normal to the vortex axes. The effective diameter d^* is then determined to match the measured frequencies to the Roshko relations which then become

$$F\left(\frac{d^*}{d}\right)^2 = B_R Re_d \left(\frac{d^*}{d}\right) \sin(\alpha+\beta) - C_R ,$$

where B_R (= 0.212) and C_R (= 4.5 or 2.7) are the Roshko constants.

Both U^* and d^* are defined as functions of the Reynolds number of the flow Re_d and the yaw angle β by the following empirical formulae. The relation between the yaw angle and the angle α between the cylinder and the vortex axes, valid over the whole range of yaw angle $0° \leq \beta \leq 90°$, takes the form

$$\cos\alpha = \frac{170 \sin^{4/3}\beta}{1 + 169 \sin^{4/3}\beta} .$$

The expression derived for the effective diameter is

$$\frac{d^*}{d} = A + Be^{-kR} ,$$

where $R = (Re_d/1000)$ and, for the range of yaw angles $0° < \beta < 12°$, the parameters A, B and k are given by

$$A = [1 + 0.08(90-\beta)/\beta - \{(90-\beta)/68.5\}^2],$$

$$B = 0.314[(90/\beta)^{0.79} - 1],$$

and $k = 0.363(\beta-1) - 0.014\,\beta^2$ (with β in degrees).

8.2.2 Vortex-shedding angles

Hydrogen-bubble flow-visualisation images of the vortex street formed in the wake of a yawed cylinder are similar to those of the vortex street formed in the wake of a cylinder normal to the flow. The similarity results from the use of a plane sheet of light to illuminate the vortex wake, which produces images of the underlying "two-dimensional" vortex shedding within the more complex three-dimensional wake flow. With illumination in the plane of the cylinder yaw angle, both the orientation of the vortex axes and the influence of the experimental arrangements on the flow can be determined.

The shedding angle, taken as the inclination of the vortex core to the cylinder axis in the initial region of vortex formation (before distortion by mean-flow gradients) varies continuously with yaw angle: it shows an asymptotic approach to zero as the yaw angle approaches 90°, corresponding to parallel shedding for cylinders normal to the flow and near-parallel shedding for yaw angles in the range $45° \leq \beta \leq 90°$; and in near-axial flow the vortex-shedding angle rapidly increases to values greater than 45° as $\beta \rightarrow 0°$. The observed inclination of the vortex lines to the cylinder axis reflects the influence of the axial velocity-component on the vortex shedding, in accord with the prediction of inclined vortex-shedding from yawed cylinders made by Ramberg (1983). For the small range of Reynolds numbers considered here, the vortex-shedding angle appears to be independent of the Reynolds number.

8.3 Turbulence Mechanisms

Flow mechanisms have been investigated in detail in very thick axisymmetric turbulent boundary layers with δ/a typically about 38, in which the effects of transverse curvature are expected to be conspicuous. The turbulence in such layers exhibits properties that are characteristically and distinctively different from those associated with flat-plate turbulent boundary layers and axisymmetric boundary layers of small δ/a.

Compared with the properties of flat-plate boundary-layer turbulence, the fluctuating longitudinal velocity-component has increased turbulence intensity close to the wall, strongly asymmetric probability-density functions, and much greater negative skewness throughout the layer. These results support the hypothesis advanced by Luxton et.al.(1984) that, in cases of sufficiently large δ/a, transverse-curvature effects result in an additional turbulence-generating mechanism that involves low-speed inner-layer fluid being stripped from the cylinder surface by transient turbulent cross flows, and convected outwards through the boundary layer. The large negative skewness is associated with the occurrence of large negative spikes in the velocity time-histories at all radial positions, and the regions of fluid in which they occur have been termed "low-speed spots". The negative velocity excursion from the mean that characterises a low-speed spot has been established as $u < -2u'$.

Hydrogen-bubble flow-visualisation images show outward random ejections of inner-boundary-layer fluid as coherent ribbons (shear layers), which often roll up to

form vortices in the outer layer. Simultaneous recordings of streamwise-velocity fluctuations and flow visualisation by smoke marking inner-layer fluid show that the low-speed spots detected in the velocity records can be identified with inner-layer fluid that is being advected outwards through the boundary layer.

By conditional sampling and ensemble averaging, the velocity distribution characterising the low-speed spots has been determined at a number of locations across the boundary layer. The spots have similar signatures at all radial positions, and appear to be a characteristic feature of the turbulence in a boundary-layer subject to extreme transverse curvature, such as that presented by long slender cylinders in axial flow. A synthesis of the time delays between the occurrence of low-speed spots at different radial locations, measured from a series of simultaneous ensemble averages of two conditionally-sampled velocity signals, leads to identification of a continuous ribbon of low-speed inner-layer fluid extending from the cylinder surface to the outer edge of the boundary layer. The ribbon forms a "front" of low speed fluid that is carried downstream by the mean flow and eventually diffuses into the local flow. On formation, the front has a well-defined (almost parabolic) shape given by $y \approx 0.175(\Delta x)^{1.75}$, an axial extent (estimated from the time-duration of the ensemble-averaged signatures of the low-speed spots) in the order of about 2δ. The azimuthal extent of the front has not, however, been determined.

The fluid particles which form the front have streamwise velocities that are far greater than their outward radial velocities; their trajectories are therefore inclined to the cylinder axis at quite small angles (for example $0.6°$ at $y/\delta = 0.59$ in flow with $Re_a = 300$).

The mechanism of formation of low-speed spots and consequently of low-speed fronts has been identified by detection of low-speed spots on one side of the cylinder, and the simultaneous measurement of streamwise and radial velocity-components on the opposite side of the cylinder and also at a range of angular positions around the cylinder perimeter. Low-speed-spot formation is associated with a body of high-speed fluid significantly larger in streamwise extent than the cylinder diameter (30 cylinder diameters in the case investigated in detail) which has acquired a radially-inward turbulence velocity. The progressive movement of this fluid across the cylinder, while it is simultaneously moving downstream, displaces inner-boundary-layer fluid to the opposite side of the cylinder to form a low-speed spot and initiates the outward movement of the spot. Progressive displacement leads to the coalescence of low-speed fluid into a low-speed front.

The local transient regions of near-axial flow, with cross-flow velocities, that are associated with the formation of low-speed spots approach the cylinder at small yaw angles, typically less than 1°. The combination of Reynolds number and yaw angle of these transient turbulent cross-flows within the axisymmetric boundary layer corresponds to the boundary region of the regular-vortex-shedding regime for yawed cylinders in near-axial flow. As this boundary region is associated with irregular vortex shedding from cylinders in near-axial flow, transient cross-flows within this region, in the axial-flow case, can be expected to result in boundary-layer separation on the "lee" side of the cylinder, but not to generate a distinct vortex-shedding frequency.

The very small impedance to transverse flow presented by a small-diameter cylinder within a large-diameter boundary layer is considered to be the feature

distinguishing the thick axisymmetric turbulent boundary layer from axisymmetric layers of smaller δ/a. When the cylinder is large relative to the radially-inward turbulent fluctuations, the wall blocks the inward velocity in a manner similar to a flat plate, and turbulence is generated by the "burst-sweep" cycle identified for flat-plate boundary layers. When the cylinder is small relative to the region of inward flow, the flow passes around the cylinder causing the boundary layer to separate temporarily, forming a local wake of low-speed inner-layer fluid. As the inward-flow region moves downstream the ejected low-speed fluid is left behind, but continues to migrate outwards with a radial velocity acquired from the passing cross-flow.

The repeated stripping of inner-layer fluid, and its coalescence into low-speed fronts represents a new mechanism of vorticity and turbulence generation - in addition to those established for flat-plate boundary layers. The principal additional turbulence mechanisms proposed are: the creation of vorticity by the repeated regeneration of the boundary layer in an extremely high-velocity-gradient environment, and its dispersion into the outer layer by subsequent inner-layer ejections; and, the interaction of the outer layer with the slower fluid in the low-speed front, primarily as a result of the blockage caused by the slow fluid to the surrounding faster-moving boundary layer fluid.

The flow mechanisms that are proposed for turbulent axisymmetric boundary layers with very large δ/a extend the range of mechanisms considered to be significant in the generation of turbulence within boundary layers in general (see, for example, Chong et.al. 1998). The details of these mechanisms revealed by the present investigation materially increase our understanding of the process (discussed previously by Bull et.al. 1988) by which the small surface area of the cylinder maintains such a large volume of turbulent flow in the thick axisymmetric boundary layer.

8.4 Subjects for Further Investigation

The broader investigation of this subject area, by both current and previous researchers, has produced a great number of topics requiring further investigation, of which the following three are most directly related to continuation of the present investigation.

1. Accurate measurement of the wall shear stress τ_w by direct means for cylinders of small diameter, from which the friction velocity can be determined as $U_\tau = (\tau_w/\rho)^{1/2}$.

This would allow a more accurate reduction of position measurements within the boundary layer in terms of non-dimensional wall units $y^+ = yU_\tau/\nu$ for the flow regime of large δ/a examined here. The inner-layer flow-stripping mechanism could then be more accurately examined for flow similarity close to the wall over a range of Reynolds numbers, and its dependence on Re_a and x/a determined. The effects of transverse curvature on the wall shear stress, and thus on the fluid-dynamic drag may then also be better understood for both cylinders and other surface shapes.

2. Investigation of the boundaries of the flow regime within which the low-speed fronts observed in this investigation occur.

At small transverse curvatures the turbulent-flow mechanisms are expected to approach flat-plate behaviour; however, for transverse curvature the limits are unknown. The flow mechanism examined in this investigation is expected to become

increasingly significant with increasing transverse curvature. This may, however, be limited by the perimeter of the cylinder approaching the average sub-layer streak spacing, that is $2\pi a$ becoming of the order of 100 ν/U_τ or $a^+ \rightarrow \sim 16$: for a^+ smaller than this value, the boundary layer on the cylinder is unlikely to be turbulent.

3. Further investigation of the results of varying the cylinder end conditions and the boundary conditions of the flow for yawed cylinders.

The present investigation has been focused on the quasi-two-dimensional case corresponding to a cylinder of infinite aspect ratio l/d. This infinite-aspect-ratio case is particularly relevant to problems associated with towed sonar arrays where the cylinders are extremely long. There are many other applications involving short cylinders yawed to the flow, particularly in vehicle aerodynamics, where specific cylinder end conditions exist. The prediction of the vortex wake behaviour for problems of this type requires a greater understanding of the way in which specific finite end conditions modify the results obtained here for the essentially infinite cylinder. Further understanding of cylinder end effects is also significant in the study of cylinders normal to the flow; the vortex-shedding process is often assumed to be quasi-two-dimensional, but various three-dimensional characteristics are known to occur for different end conditions.

Further investigation of these particular topics can be expected to add to the new insights provided by the present investigation in understanding the fundamental fluid mechanics of cylinders in axial and near-axial flow.